2015-06-16

Cloud and Aerosol Optics by Polarized Micro Pulse Lidar and Ground Based Measurements of Zenith Radiance

Rodrigo Delgadillo
University of Miami, lobos799@yahoo.com

UNIVERSITY OF MIAMI

CLOUD AND AEROSOL OPTICS BY POLARIZED MICRO PULSE LIDAR AND GROUND BASED MEASUREMENTS OF ZENITH RADIANCE

By

Rodrigo Delgadillo

A DISSERTATION

Submitted to the Faculty
of the University of Miami
in partial fulfillment of the requirements for
the degree of Doctor of Philosophy

Coral Gables, Florida

August 2015

UNIVERSITY OF MIAMI

A dissertation submitted in partial fulfillment of
the requirements for the degree of
Doctor of Philosophy

CLOUD AND AEROSOL OPTICS BY POLARIZED MICRO PULSE LIDAR AND GROUND BASED MEASUREMENTS OF ZENITH RADIANCE

Rodrigo Delgadillo

Approved:

Kenneth J. Voss, Ph.D. Professor of Physics	Olga Korotkova, Ph.D. Associate Professor of Physics
Howard R. Gordon, Ph.D. Distinguished Professor of Physics	Dean of the Graduate School
Paquita Zuidema, Ph.D. Professor of Meteorology and Physical Oceanography	

DELGADILLO, RODRIGO (Ph.D., Physics)

Cloud and Aerosol Optics by Polarized Micro Pulse Lidar and Ground Based Measurements of Zenith Radiance (August 2015)

Abstract of a dissertation at the University of Miami.

Dissertation supervised by Professor Kenneth J. Voss.
No. of page in text. (112)

Clouds impact Earth's climate through cloud transmission and reflection properties. Clouds reflect approximately 15 percent of the incoming solar radiation at the top of the atmosphere. A key cloud radiative variable is cloud optical depth, which gives information about how much light is transmitted through a cloud. Historically, remote measurements of cloud optical depth have been limited to uniform overcast conditions and had low temporal and spatial resolution. We present a novel method to measure cloud optical depth for coastal regions from spectral zenith radiance measurements for optically thin clouds, which removes some of these limitations. Our measurement site is part of South Florida's Cloud-Aerosol-Rain Observatory (CARObb), located on Virginia Key, FL (6 km from Miami). This work is based on Marshak et al.'s [1] method for finding cloud optical depth from vegetative sites that provide a strong spectral contrast between red and near infrared surface albedo. However, given the unique nature of our site, which contains water, vegetation, beach, and urban surface types, we found no such spectral contrast at those wavelength pairs. We measured albedo, with hyperspectral resolution, for different surface types around our measurement site

to estimate the effective spectral albedo for the area centered on the site with a 5km radius. From this analysis, we found the best possible albedo contrast (573.9 and 673.1 nm) for our site. We tested the derived cloud optical depth from zenith radiance at these two wavelengths against a concurrently running polarized micro pulse LIDAR (MPL) and found good agreement.

For my father.

ACKNOWLEDGMENTS

Graduate school has been a tremendous experience in my life, and there are many people to thank for the many memories I'll certainly carry with me for the remainder. My advisor, Dr. Kenneth Voss is a very patient and kind person. He gave me a lot of freedom during my time here. Sometimes it was challenging, but that made the victories so much sweeter. I believe this is his method, because as physicists we should be leaders in our research, have original thoughts, and be self-reliant. I'm really thankful for this. He has also been a great guide through the writing of my thesis. I would also like to thank Dr. Paquita Zuidema. She has been like my second advisor, supporting me and guiding me through the years. Voss and Zuidema are both primary investigators of the CARObb program, which is NSF funded, and is the primary grant that pays for my instrumentation. To the rest of my committee Dr. Howard Gordon and Dr. Olga Korotkova, I would like to thank for reviewing my work and being a resource on topics related to optics. Korotkova led our optics seminar in which she would bring in papers on optics. Sometimes the topics ranged far outside our current research, which opened our eyes to the possibilities. In meetings, I'll always remember Dr. Gordon for explaining things in a clear and concise ways.

I'm very thankful to the University of Miami for having many great activities and resources for graduate students. I served as a Senator for the physics department in the Graduate Student Association (GSA) for two years and it was a learning experience in leadership. During this, I became aware of how much the university really cares about our education and experience.

I would also like Dr. Michael Gaines and the NSF for funding me for two years under the Science Made Sensible Fellowship (SMS), an NSF GK-12 STEM fellowship. As part of the fellowship, we learned about inquiry learning. We designed inquiry based labs and lesson plans and tested them on inner city middle school students in Miami. The idea was to create thought provoking labs that engage the students and build critical thinking skills. During my time in SMS, Dr. Gaines also selected me to spend a summer teaching inner city students in Pretoria, South Africa. It was a life changing experience.

I want to thank the staff at the physics department. Annie Sebro, our secretary, is always kind and helpful. Marco Monti could always save the day when something computer related went awry. Juan Lopez, our electronics expert, taught me many things about electronics and proper soldering technique.

To my friends and colleagues, I'm thankful for all the good times and companionship. As graduate students we organized ourselves to start a graduate student seminar series. The idea is to have a series of talks where graduate students could share their ideas with fellow graduate students. We believe that this would help create a community aspect, provide alternative perspectives to our research, and improve our communication skills. I led the creation of this series, but it wouldn't have been possible without the support of other graduate students who banded together, especially Pedro Manrique, Saeed Moshfeghyeganeh, Youaraj Uprety, Andrey Lazopulo, and Stanislav Lazopulo. Also, thanks to Joshua Cohn, the department chair, for supporting this activity especially in the form of money for pizza and drinks.

Most of all, I would like to thank my family for inspiring me to seek a career in science. My father brought me to the United States when I was only three years old with a dream. He raised me by himself and imparted the value of education

and self-reliance. My whole life, I've been working to repay his sacrifice through hard work and by obtaining a Ph.D. in physics. I always looked up to my uncle. He would speak of the importance of education and to not let anybody tell me that I cannot achieve my goals. Although we were very poor, we had big dreams. My dream was to become a scientist, and by finishing this Ph.D. that is finally a reality.

TABLE OF CONTENTS

List of Figures

List of Tables

Chapter 1

Introduction

Clouds determine a large part of the balance of Earth's incoming and outgoing radiation, the Earth's energy budget, which then directly influences the climate. We can consider clouds as having both a cooling and heating effect on the Earth's temperature. On the one hand, radiation coming from space is reflected back out, which causes cooler temperatures. On the other hand, long wave radiation emitted from the Earth's surface can become absorbed and re-emitted from the bottom of clouds, which causes hotter surface temperatures when compared to clear-sky conditions. Clouds vary greatly both in time and space, which leads to the complexity in measuring their optical properties. Although clouds have traditionally been poorly understood, there has been much interest in the recent years to improve our knowledge of them. Among the most important variables in cloud optics is cloud optical depth. When cloud optical depth is large, clouds backscatter more light, and transmit less. This directly influences how much energy is either backscattered or transmitted, which plays a big role in the Earth's energy budget given that about half of the Earth is covered by clouds at any given moment [4].

We are interested in focussing on cloud optical depth for this work. Our work is part of South Florida's Cloud-Aerosol-Rain Observatory (CAROb), an observatory located on Virginia Key (6 km from Miami, FL) on the University of Miami's RSMAS Campus, with the goal to study clouds, aerosols, and Saharan dust. Accurate measurements are difficult because past techniques either require extra knowledge

about the cloud layer that is not readily available, or because the techniques used do not provide local measurements since they rely on irradiance based techniques that are thus averages over a larger area. In the sections that follow, we will discuss clouds, their important features and how cloud optical depth fits into the picture. As part of this discussion, we will also review what has been done previously with cloud optical depth and the challenges encountered with these techniques.

1.1 Size Distributions

Clouds are highly variable, ranging in optical thickness, altitudes, and shapes. This variability adds to the difficulty in modeling them. Primarily, water makes up the contents of clouds, either in liquid or solid phase states. Non-precipitating cloud particle radii range from 6 to 20 μm [4]. The lower limits of particles size are determined by coagulation and condensation processes. Water vapor condenses on different nuclei particles in the air, salt for example, to form clouds. This condensation process is the initial process that begins to grow the cloud particles, and determines the lower limit of particle size. Gravitational effects determine the upper limit of particle size. As particles begin to grow, through collisions and condensation, they become heavier and fall faster, with the fall speed roughly proportional to the square of the particle radius. A cloud droplet of radius 20 μm falls at approximately 4 cm/s and begins to collide and coalesce with smaller particles. Unless caught in a strong up draft, such a particle is likely to fall through the cloud base and either evaporate or reach the surface as precipitation. When particle size increases beyond 20 um, they spend only a little time in the atmosphere compared to smaller particles.

However, clouds are not uniform. We have to consider cloud particle size distributions, where the two important variables become the effective radius and the width of the distribution. Two commonly used size distributions are the gamma

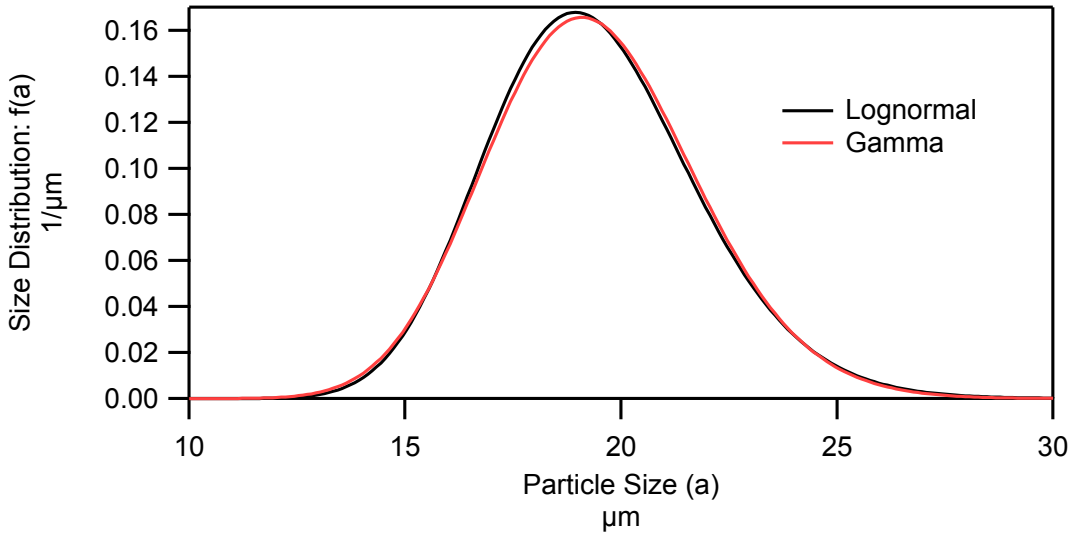

Figure 1.1: Particle Size Distribution functions with effective particle size of 20 μm and coefficient of variation of $2.5/20 = 0.125$.

distribution and lognormal distributions, which are based on the natural distributions of cloud particles. Size distributions are characterized by size distribution functions $f(a)$ that must be normalized such that [4]:

$$\int_0^\infty f(a)\,\mathrm{d}a = 1 \tag{1.1}$$

where a is the particle radius. The average of a variable x weighted by the PDF is found by:

$$\langle x \rangle = \int_0^\infty x f(a)\,\mathrm{d}a \tag{1.2}$$

The gamma distribution has been shown to be a good model for the PDF of clouds [5]

$$f(a) = \frac{\mu^{\mu+1} a^\mu}{\Gamma(\mu+1)\, a_0^{\mu+1}} e^{-\mu\left(\frac{a}{a_0}\right)} \tag{1.3}$$

where μ describes the size distribution width (typically between 2 and 8), a_0 is the peak in the distribution, and Γ is the gamma function:

$$\Gamma(\mu) = \int_0^\infty s^{\mu-1} e^{-s}\,\mathrm{d}s \tag{1.4}$$

Another commonly seen size distribution is the log-normal distribution [6, 4]:

$$f(a) = \frac{1}{\sqrt{2\pi}\sigma a} e^{-\frac{\ln^2(a/a_m)}{2\sigma^2}} \tag{1.5}$$

where a_m is the mean of $\ln(a)$, and σ is the standard deviation of $\ln(a)$. The effective radius is found by the ratio of the average volume to surface area of cloud particles [7]:

$$a_{ef} = \frac{\langle a^3 \rangle}{\langle a^2 \rangle} \tag{1.6}$$

The gamma and log-normal distributions use different variables to define the distribution shape and peak. To compare them, we relate them to the effective radius a_{ef} and coefficient of variation:

$$C_{var} = \frac{\sqrt{\langle (a - \langle a \rangle)^2 \rangle}}{\langle a \rangle} \tag{1.7}$$

which is the ratio of standard deviation and mean of the particle size. For the gamma distribution:

$$a_{ef} = a_0 \left(1 + \frac{3}{\mu}\right) \ , \ C_{var} = \sqrt{\frac{1}{\mu + 1}} \tag{1.8}$$

For log-normal distribution:

$$a_{ef} = a_m e^{2.5\sigma^2} \ , \ C_{var} = \sqrt{e^{\sigma^2} - 1} \tag{1.9}$$

Then, the variables a_0, μ, a_0, and σ can be solved in terms of a_{ef} and C_{var}. For the gamma distribution:

$$a_0 = \frac{a_{ef} C_{var}^2}{3 - 2C_{var}^2} \ , \ \mu = \frac{1}{C_{var}^2} - 1 \tag{1.10}$$

For the log-normal distribution:

$$a_m = a_{ef} e^{-2.5 \ln\left(1 + C_{var}^2\right)} \ , \ \sigma = \sqrt{\ln\left(1 + C_{var}^2\right)} \tag{1.11}$$

For an effective radius equal to 20 μm and coefficient of variation equal to 0.125:

$$a_0 = 19.09, \ \mu = 63, \ a_m = 19.24, \ \sigma = 0.1245 \tag{1.12}$$

The resulting distributions are shown in Fig. 1.1.

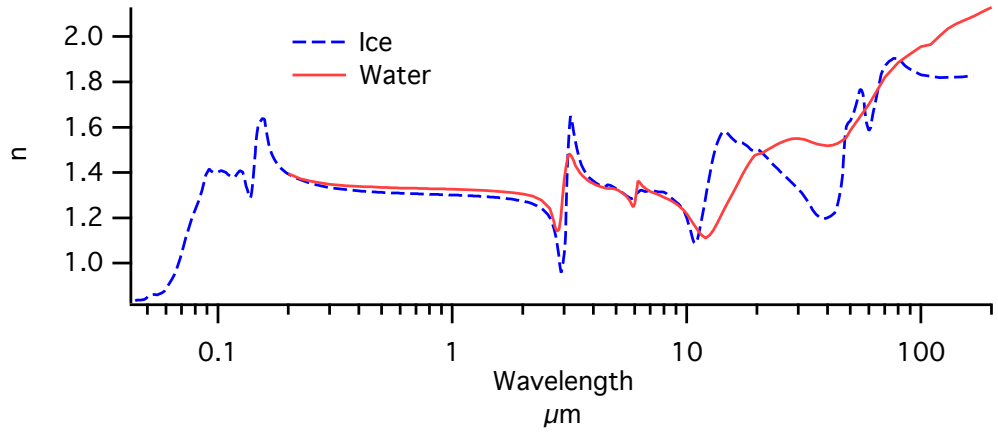

(a) Real part

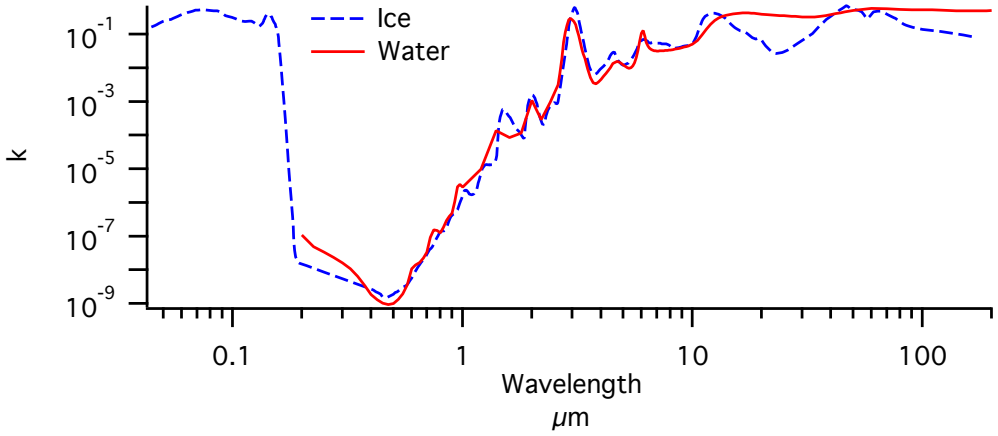

(b) Imaginary Part

Figure 1.2: Refractive index for water and ice.

1.2 Liquid vs. Ice Particles

When cloud particles are made up of ice crystals, several optical features are altered in comparison to clouds that are mainly liquid water droplets. One such feature is the index of refraction. Figure 1.2 shows the refractive index for water [8] and ice [9]. From 0.400 to 1.8 μm, the real part of refractive index (n) decreases for both water (1.339 to 1.312) and ice (1.319 to 1.283), with ice generally being lower than water. However, the imaginary part of the refractive index (k) increases for both water (1.86×10^{-9} to 1.15×10^{-4}) and ice (2.71×10^{-9} to 1.03×10^{-4}) for the same

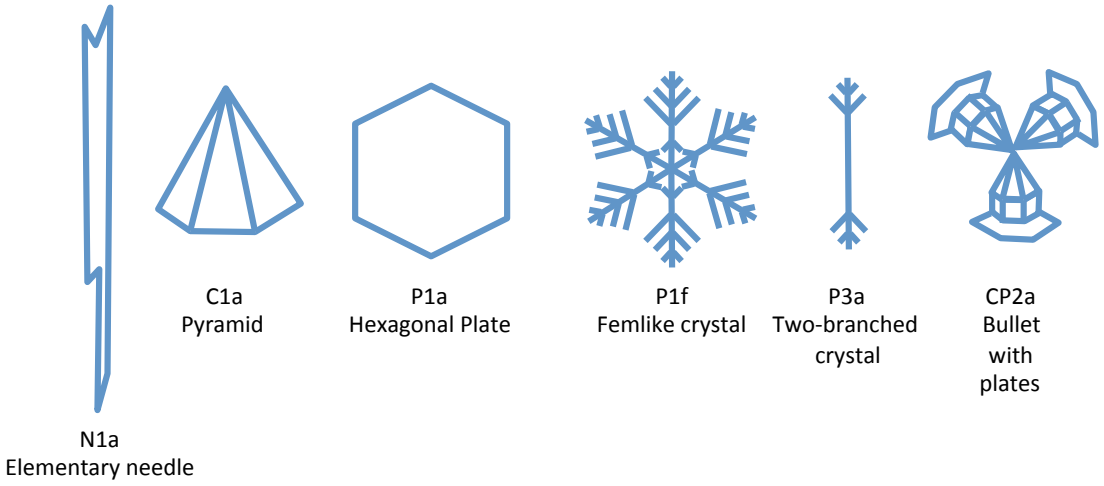

Figure 1.3: Examples of snow crystals for meteorological classification by Mogano and Lee (1966)

wavelength range. This variability in the imaginary part (k) of the refractive index explains the different absorption values within particles at different wavelengths.

With colder temperatures, there tend to be more and more ice particles in clouds and the particles tend to be bigger. Much like the expression "as unique as a snowflake" implies, the shapes that they can take are highly variable. Mogano and Lee (1966) [10] identified 80 different classification types of snow crystals. Some selected examples of crystal types are shown in Fig. 1.3. This greatly complicates calculations given that each crystal type would have its own proper size distribution. Given the geometry of ice crystals, one can understand that light scattering off of ice crystals has a depolarizing effect. Polarized lidars apply this concept to differentiate between ice and water clouds[11] by measuring the depolarization ratio. Clouds can also exist in mixed states (ice and water).

1.3 Cloud Optical Depth

If the concern is how much radiation is transmitted through a medium, then transmittance is key. For a simple medium, optical depth is related to the direct transmittance by:

$$T = \frac{E}{E_0} = e^{-\tau} \tag{1.13}$$

where T is the transmittance, E is direct irradiance (radiative power incident on an area), E_0 is initial direct irradiance, and τ is optical depth of the medium and a dimensionless quantity. In the atmosphere, we have to account for the airmass, the path length through the atmosphere, which modifies the transmittance to be [12]:

$$T_{atm} = e^{-m\tau} \tag{1.14}$$

where m is the airmass. When accounting for the atmospheric refraction and the earth's curvature, the airmass is [13]:

$$m(\theta) = \frac{1}{\cos(\theta) + 0.15\,(93.885 - \theta)^{-1.253}} \tag{1.15}$$

where θ is the zenith angle, which works for large and small angles. For small angles ($\theta < 82°$), the airmass can be approximated as:

$$m(\theta) = \frac{1}{\cos(\theta)} \tag{1.16}$$

As seen in Fig. 1.4, at around 82° the small angle approximation diverges by 5% from Eq. 1.15.

1.3.1 Cloud Optical Depth Methods

In the past, cloud optical depth research has been dominated by satellite and ground based techniques. The International Satellite Cloud Climatology Project (ISCCP) was created as part of the World Climate Research Programme (WCRP)

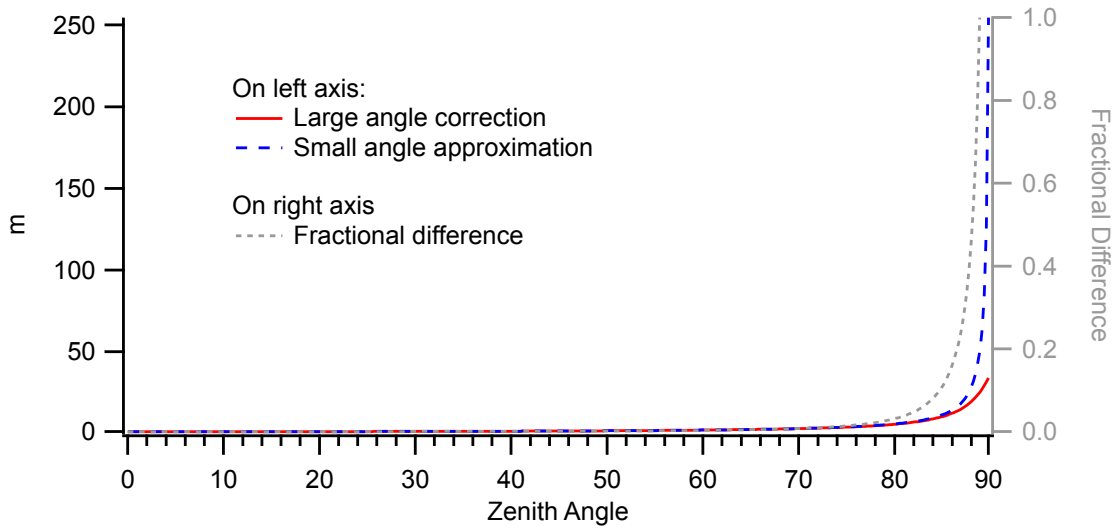

Figure 1.4: Airmass versus zenith angle comparison between the large angle correction (Eq.1.15) and the small angle approximation (Eq.1.16).

to use satellite based radiance measurements to determine cloud radiative properties on a global scale in order to improve cloud and climate models [14]. Data from this project is available spanning the dates of July 1983 to December 2009. Han et al (1994) determined the effective particle radius and cloud optical depth from lookup tables, which modeled reflected radiance from the top of Earth's atmosphere using radiative transfer theory[15]. One of the drawbacks is that these derived products are on a global scale and often represent 30 day, and in some cases yearly, averages. The project was intended to use a spatial averaging of 250 km by 250 km boxes, consequently, the data are not local. These become concerns when one is interested in studying clouds overhead at higher spatial resolution. Another challenge with satellite based measurements of cloud optical depth [16, 17] is finding independent measurements with which to compare, which has led to increased interest in ground based measurements [18].

Irradiance and radiance are two commonly measured light quantities in cloud optics. Irradiance (E), which has units of $\frac{W}{m^2}$, is a measure of how much radiative

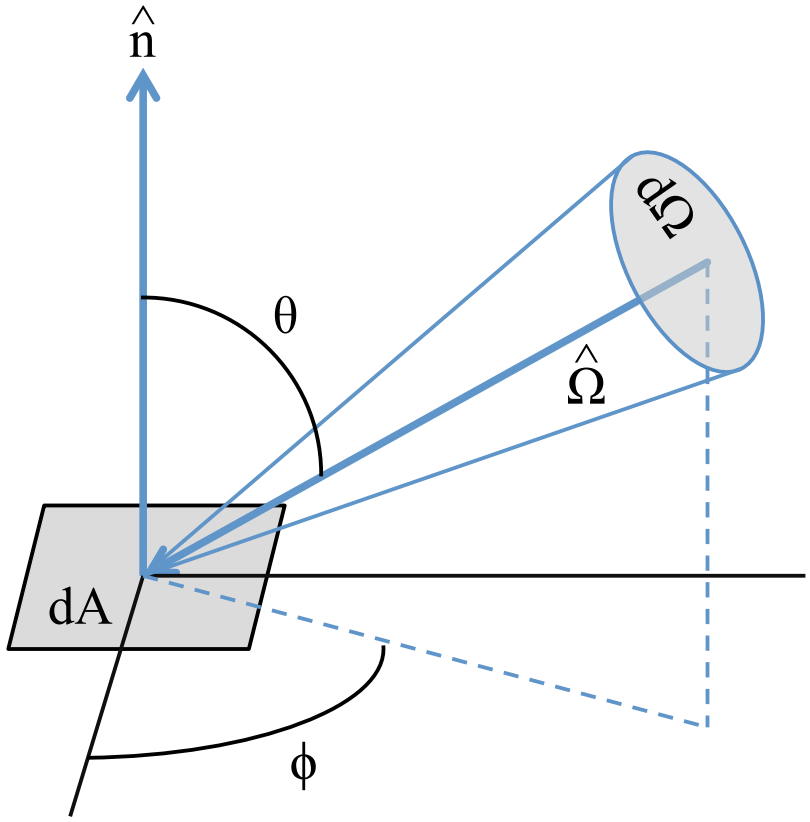

Figure 1.5: Radiance beam geometry

power is incident on an area. However, we often refer to spectral irradiance $E(\lambda)$ which is related to total irradiance E by:

$$E = \int_0^\infty E(\lambda)\,\mathrm{d}\lambda \tag{1.17}$$

where $E(\lambda)$ has units of $\frac{W}{m^2 nm}$. Radiance is the amount of radiative power incident on an area per solid angle with units $\frac{W}{m^2 sr}$, and similarly spectral radiance has $\frac{W}{m^2 sr\ nm}$. Conversely, irradiance is integral of radiance over solid angle:

$$E = \int_\Omega L(\widehat{\Omega}')\ \widehat{n}\cdot\widehat{\Omega}'\,\mathrm{d}\Omega' \tag{1.18}$$

where $\widehat{n}$ is the surface normal and $\widehat{\Omega}'$ is direction of the beam. The geometry is shown in Fig. 1.5. If we consider the upwelling irradiance, light emerging from the

surface and heading skyward, we have:

$$E^{\uparrow} = \int_0^{2\pi} \int_0^{\pi/2} L^{\uparrow}(\theta, \phi) \cos(\theta) \sin(\theta) \, \mathrm{d}\theta \, \mathrm{d}\phi \tag{1.19}$$

where θ is the zenith angle and ϕ is the azimuth angle.

Ground based techniques have focused on irradiance based methods, which come in broadband [19, 20, 21, 22] and spectral [23] varieties. There are also radiance [1] based measurements. It also possible to use lidar for cloud optical depth, but this is limited to thin clouds, since typical lidars are low power and cannot penetrate optically thick clouds.

Irradiance methods focus on modeling the total downwelling irradiance on the surface. Important inputs are surface albedo and the atmospheric layers in the scene, which include aerosol (large particles), Rayleigh (molecular), and cloud layers. In some studies, the authors used broadband irradiance. Leontyeva and Stamnes (1992) [24], for example, used a pyranometer to measure irradiance between 0.3 to 4 μm and from this derive cloud optical thickness. Some authors use spectral irradiance. For example, Min and Harrison (1996)[23] measured spectral irradiance at 6 wavelengths (415, 500, 610, 665, 862, and 940 nm) with 10 nm full width half maximum response on each channel to derive cloud properties. An inherent limitation of irradiance methods for cloud optical depth is that the detectors have a large field of view since they view incoming light for the entire hemisphere. This results in a requirement that it be completely overcast since you want the cloud properties to be consistent over the field of view of the measurement. A large field of view (FOV) can make it difficult to discriminate between cloud scenes for small clouds. For example, you can imagine a scenario where a small and optically thin cloud produces the same irradiance as a large and optically thick cloud. In the first situation you have little reflection off the cloud, but a large clear sky contribution. In the second situation, you have more reflection off the cloud and little clear

sky contribution. For this reason, you are limited to uniform overcast conditions for irradiance methods. Radiance methods are limited in a similar way, but since they have a smaller FOV they can look at smaller clouds. Particularly, this an issue with the small cumulus clouds which dominate the sky in South Florida.

One of the main objectives of ground based irradiance studies is to provide an independent source to compare with satellite studies such as ISCCP [19]. However, studies show that surface τ_{srf} and satellite τ_{sat} based retrievals of cloud optical depth disagree greatly, with on average $\tau_{srf} \approx 1.6\tau_{sat}$ [19, 23]. This large disagreement drives interest to generate alternative methods that provide a source of independent comparisons.

For our work, we have decided to build upon the work by Marshak et al. [1], which is a radiance based method. It will be discussed in detail in the following chapters. For now, let's consider some of pros and cons of this method. One of the notable improvements over irradiance based techniques is that it allows cloud optical depth for non-overcast conditions. The radiance measurements typically have an FOV less than 2°. Effective cloud fraction can also be estimated through this technique. Another feature is that it allows studying cloud optical depth on the time scale of clouds. That is, it may be possible to measure clouds as they are changing, which is an improvement over the satellite techniques we discussed earlier. As with irradiance based techniques, one of the requirements of this method is that the surface albedo must be known, which can be difficult to estimate for heterogeneous coastal regions containing vast amount of water as in Miami. Another requirement is that there be strong contrast in albedo for two wavelengths, which may not always be possible for some locations.

This method also shares some of the limitations of irradiance methods, which is that they only give an effective cloud optical depth since they assume a plane

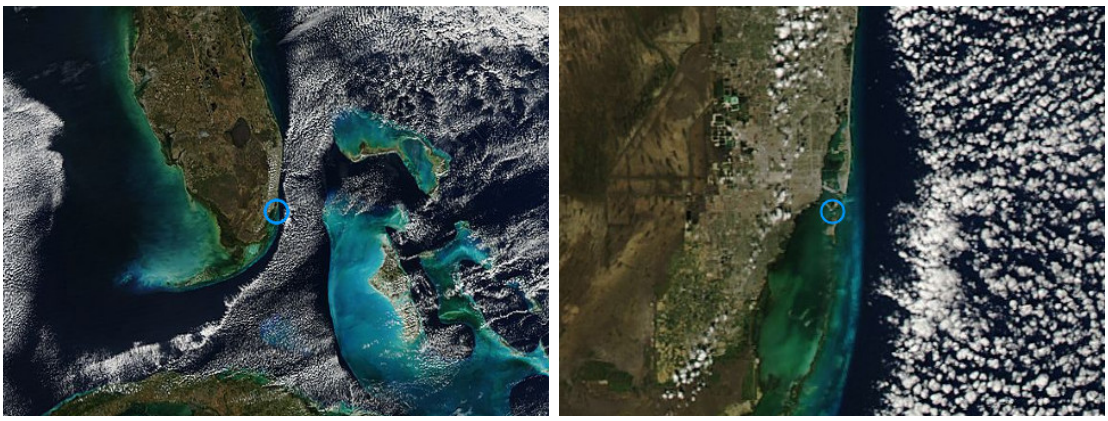

(a) 2000 m resolution (b) 250 m resolution zoomed in.

Figure 1.6: Composite Aqua-MODIS Image from 1/23/2014 centered on CARObb with overpass time: 18:45 GMT.

parallel homogeneous cloud layer which has a cloud optical depth that produces the same radiation field at the surface as the actual cloud [20], essentially assuming a one dimensional atmosphere. Clouds, however, are three-dimensional and not homogeneous in nature, thus one should be mindful of three-dimensional problems when analyzing the data. With this in mind, the cloud optical depth that we measure is the radiatively effective cloud optical depth of fitting 3D phenomena into a 1D model. Marshak et al. [1] compares a 3D Monte Carlo simulation to a 1D model of Zenith Radiance as a function of cloud optical depth [1]. In Marshak et al. [1], for the bright albedo (ρ=0.5), the 1D model is centered around the 3D model, whereas with dark albedo ($\rho = 0$) the 1D model is systematically below the 3D model. This means that if we combine lookup tables for both wavelengths that the uncertainty due to 3D effects is reduced.

Small clouds account for 15% of the global cloud cover and the smallest clouds are found over the trade wind regions of the tropics/subtropics and over arid land areas [25]. MODIS rapid response images [26], demonstrate cloud fields seen over our measurement site. The small clouds seen in Fig. 1.6 are brought in from the Atlantic by the trade winds. Present in the cloud field are many small cumulus

clouds. Optically thin clouds in marine environments represent close to 50% of low clouds [27]. Consequently, small clouds play a major role at our measurement site. Small cumulus clouds are often missed by satellites given their optically thin nature [28]. These small cumulus clouds cannot be characterized well from space, but cover a large part of globe. With the MPL and zenith radiance measurements, we have two methods to measure optically thin clouds.

Chapter 2

Instrumentation

During this thesis research, several systems were assembled that had to work simultaneously in order to get a useful data set. The main radiometer system, which I call the cloud radiometer and time-lapse video system contains three main components: the radiometer, the video camera, and the computer which records the data and controls the rest of the system. In addition, I also used a polarized micropulse lidar (MPL) and Aeronet Cimel sun photometer system. The measurement site and layout of the instrumentation can be seen in Fig. 2.1. In this aspect, this project required a lot of different responsibilities to make sure that all the systems operated correctly. Over the course of my work we obtained a four year long data set of MPL data, and two years of radiance data. This chapter is a description of these different systems.

2.1 Cloud Radiometer and Time-lapse Video System

We used two different radiometers to measure downwelling zenith radiance. They were a 6 wavelength (410, 440, 510, 550, 670, 860 nm) radiometer and a hyperspectral spectrometer with 1.2 nm spectral resolution from 400 to 900 nm. The 6 wavelength channel radiometer (1° field of view) was originally used for white cap research[29, 30]. In this work, instead of looking down at the light reflecting off white caps, it looks up at light reflecting from clouds. It was located outside on the roof of the MSC Building on the RSMAS campus. We decided to upgrade to the spectrometer to increase spectral resolution and avoid temperature variation prob-

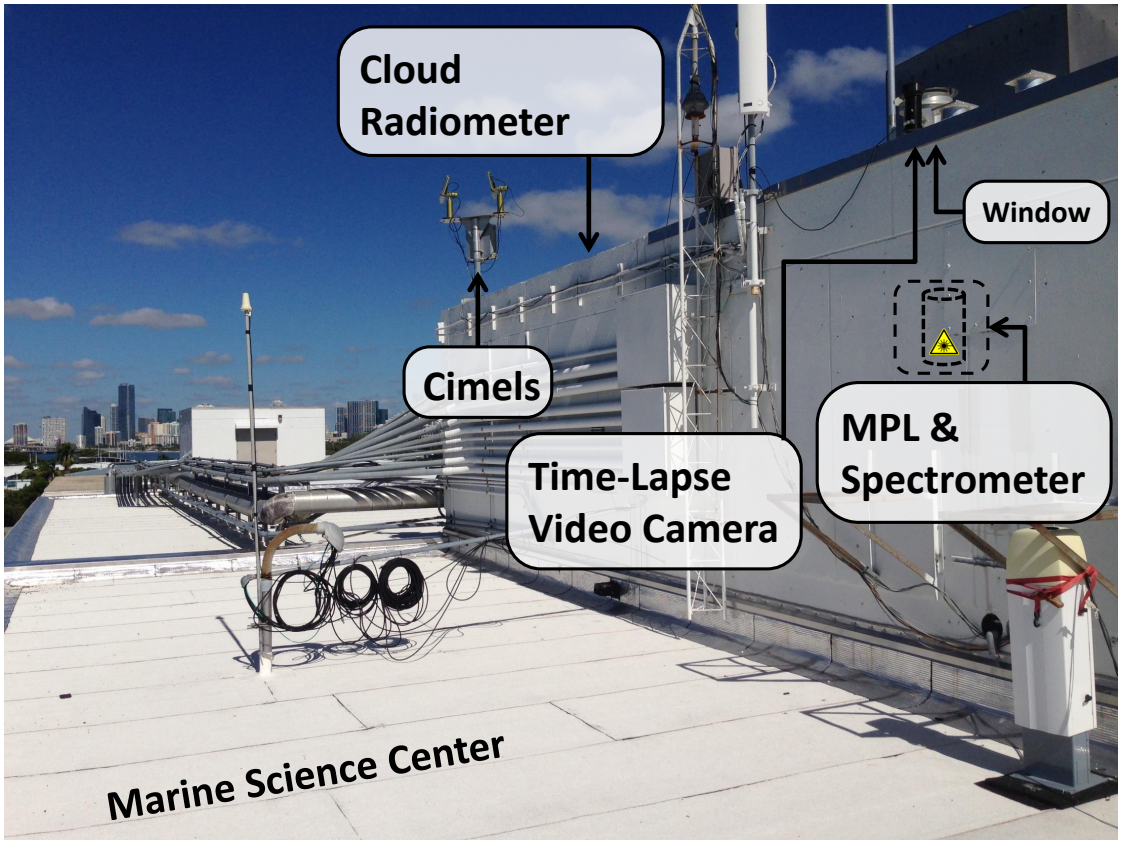

Figure 2.1: Instruments located at Key Biscayne. The Cloud Radiometer is on the other side of the wall. The MPL and Spectrometer are beside each other and inside the building. The laser light is emitted out of a window on top of the building.

lems since it has a small footprint and could be placed inside. The spectrometer is an Ocean Optics USB4000 fiber optic spectrometer. We attached a collimating lens (2° field of view) on the fiber optic cable head, which was aligned at zenith and placed next to the MPL indoors. In this section, I'll discuss the cloud radiometer and time-lapse video system in detail. I'll refer to the 6 wavelength radiometer for simplicity, but the procedure for the spectrometer is very similar.

The cloud radiometer and time-lapse video system were controlled through the use of a LabView program and shell scripts. A flowchart overview of the system is shown in Fig. 2.2. The video camera and radiometer are connected to the computer through two separate data acquisition cards (DAQ).

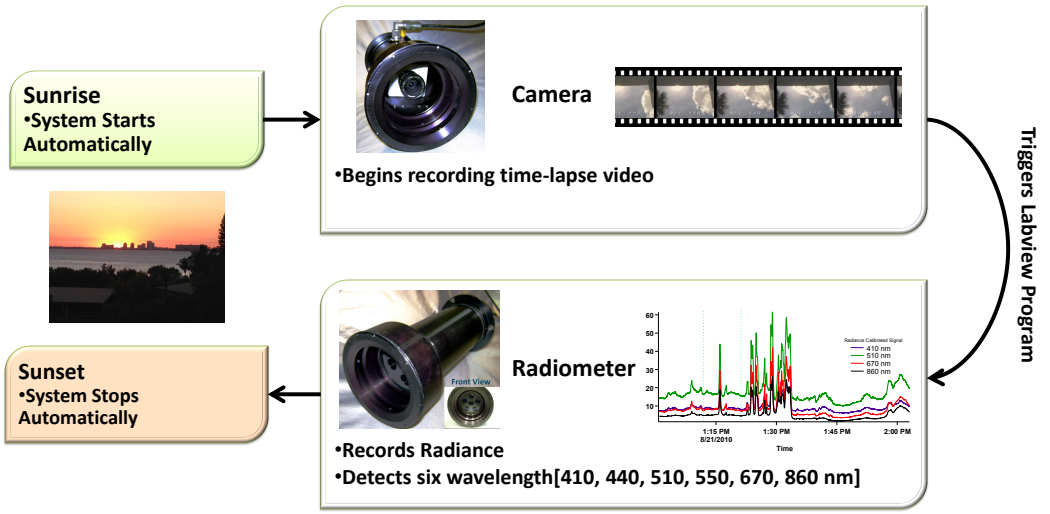

(a) Process

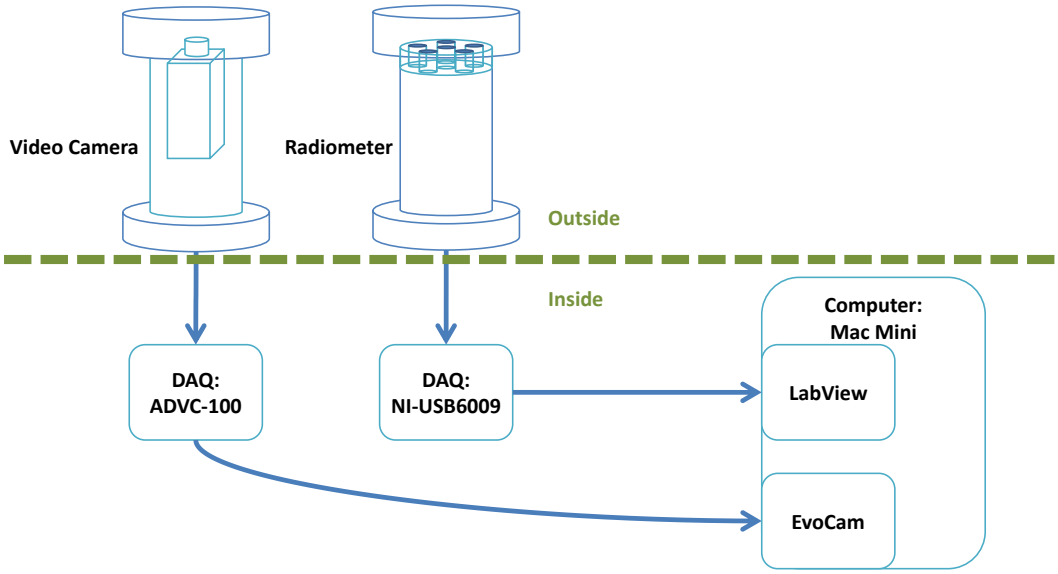

(b) Wiring Diagram

Figure 2.2: Cloud Radiometer and Time-lapse Video System

The video camera data is read by a webcam program (EvoCam) that has some very useful features. First, it allows time-lapse images to be saved. I set the time interval to 15 seconds in order to create the time-lapse video that allows us to review the clouds above the site as they were passing through the scene. This allows us to determine cloud cover during the radiometer measurements. As a side benefit, the time-lapse video can also be compared with the MPL data, which is located near the video camera. However, this is only useful during the day. The second feature is that the software has the ability to start recording when it senses daylight. This is done in two ways, by calculating sunrise and sunset times based on the latitude and longitude, or by setting a threshold of daylight. Throughout this research project, I've tried both options. The threshold of daylight is set using a slider in EvoCam and was set to 20% of the threshold which seemed to work well for our purposes. But in the end calculating the start and stop time based on the solar zenith angle for the location seemed to be more reliable, because it was less reliant on the weather conditions and gave more consistent start and stop times. The third feature is that the web cam program allows shell scripts to be triggered when certain events occur.

At sunrise, a shell script begins the radiometer's LabView data acquisition program. Likewise, at sunset, the system stops recording data. The radiometer's program records the 6 wavelength channels into ascii files to be used for later analysis. The LabView program allows the files to be time stamped and sorted by year, and then by month. This allows us to keep the large amounts of data well organized and easily accessible. In the case of the spectrometer, data is acquired through Ocean Optics Spectra Suite software. There is another shell script that is responsible for uploading/backing up the radiometer and time-lapse data to our remote servers.

2.1.1 Radiance Calibration

On its own, the radiometer measures the incoming light in volts or instrument counts, and is converted to radiance units through calibration. In order to calibrate the radiometer response we use the experimental layout shown in Fig. 2.3a. We start with a 1000 W FEL standard lamp with known irradiance spectrum, $E_0(\lambda)$, at a specific distance, as in Fig. 2.3b. The light from this lamp is reflected from a Lambertian plaque placed at 50 cm from the lamp. The radiometer is aimed at the center of the plaque at an angle of 45 degrees. The radiance from the plaque is well defined for a Lambertian surface with reflectance (ρ) and related to the irradiance by:

$$E = 2\pi \int_0^{\frac{\pi}{2}} \left(\frac{L \cos\theta}{\rho} \right) \sin\theta \, \mathrm{d}\theta = \pi L \tag{2.1}$$

where E is the irradiance and L is the radiance. The radiance from the plaque is:

$$L = \frac{E}{\pi} \rho \tag{2.2}$$

where ρ is the plaque reflectance (0.95 ± 0.01). In the end, the radiance reaching the radiometer is:

$$L_{cal}(\lambda) = \frac{0.95 E_0(\lambda)}{\pi} \tag{2.3}$$

The ratio of the plaque radiance to measured volts will give us the calibration coefficient in radiance units per volt, or:

$$C_{coef}(\lambda) = \frac{L_{cal}(\lambda)}{V(\lambda)} \tag{2.4}$$

In the following section, we'll go through an example of this calibration.

The latest radiance calibration was performed July 21, 2014. I started with the raw radiometer lamp measurement in volts, $V_{raw}(\lambda)$. This was followed by a dark measurement, $V_{dark}(\lambda)$. The dark measurement was taken by simply placing a lens cap on the radiometer, blocking the light going to it. This accounts for any

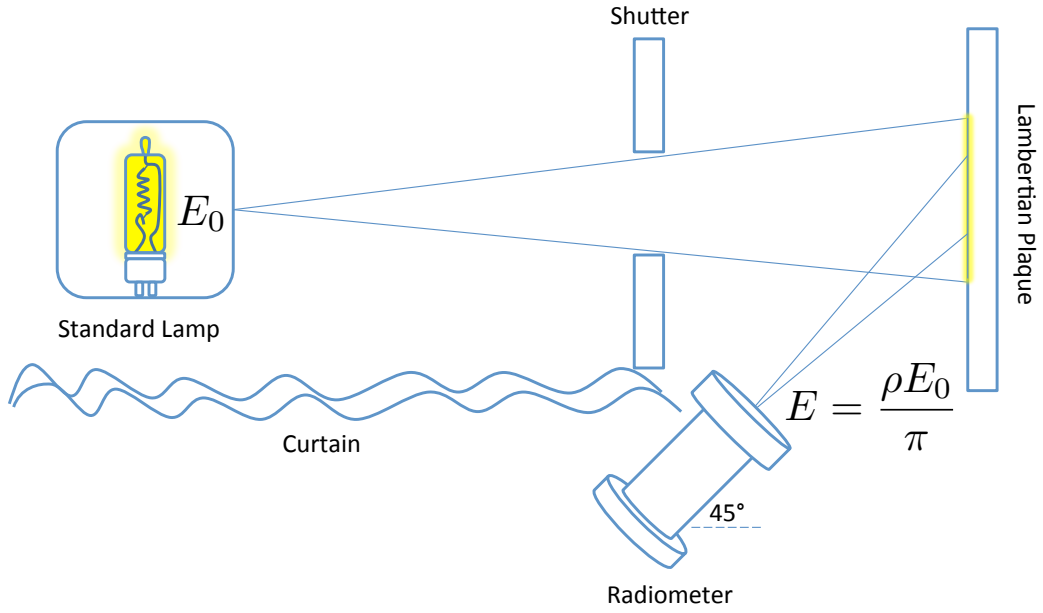

(a) For the Radiance Calibration the Plaque was placed 50cm from the standard lamp, #91795.

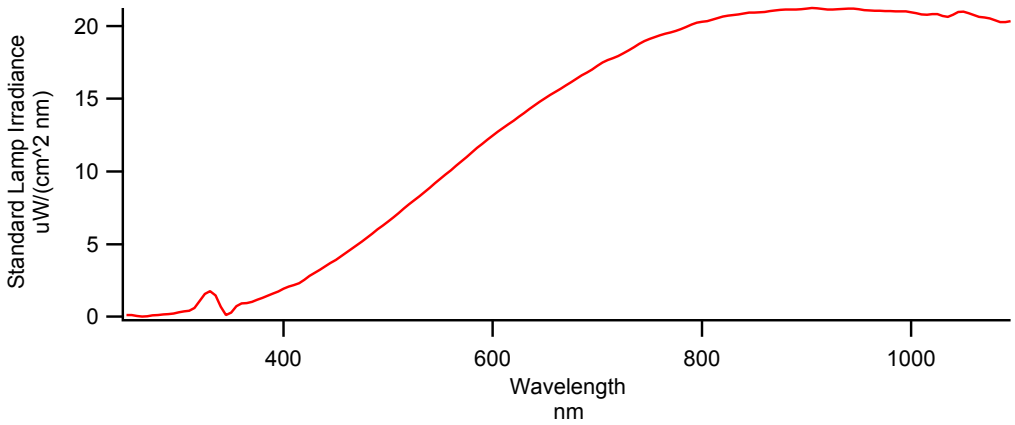

(b) Standard Lamp Irradiance, E_0, at 50cm away.

Figure 2.3: Experimental Layout and Standard Lamp Irradiance Spectrum

Table 2.1: Radiance Calibration Results

Wavelength (nm)	Calibration Coefficient Average $\left(\frac{\mu W}{cm^2 nm\ sr}\frac{1}{V}\right)$	Coefficient of Variation $\left(\frac{\mu W}{cm^2 nm\ sr}\frac{1}{V}\right)$
410	8.56	0.0130
510	73.1	0.0311
670	5.63	0.000672
860	4.18	0.000765

internal dc offsets in the radiometer for that given time. The radiometer lamp data is then dark corrected by subtracting the dark offset so that we have:

$$V(\lambda) = V_{raw}(\lambda) - V_{dark}(\lambda) \tag{2.5}$$

The dark corrected voltage, $V(\lambda)$, is then put into Eq. 2.4 to get the calibration coefficients. The 410, 670, and 860 nm channels seem to have similar calibration coefficients, but the 510 nm had a much higher calibration coefficient than the rest. This filter had a very low transmission relative to the other wavelengths.

In order to calculate statistics for this calibration coefficient, I found the average and coefficient of variation (COV), Std/mean, of the time series. The results are shown in Table 2.1. The time series ran for 14 minutes 20 seconds with a sample period of 1 second. The COV was small, but was higher for the 410 nm channel, because the plaque radiance was small, and the 510 nm channel, because the filter transmission was low. It should be noted that COV is not an assessment of accuracy. The COV of the calibrations does indicate that we have good precision, or little variation from one measurement to the next. The standard lamps that we use for routine calibrations in the lab have been calibrated to a higher standard lamp, which was calibrated in an independent laboratory. The lamps which we used have an estimated accuracy of 4%.

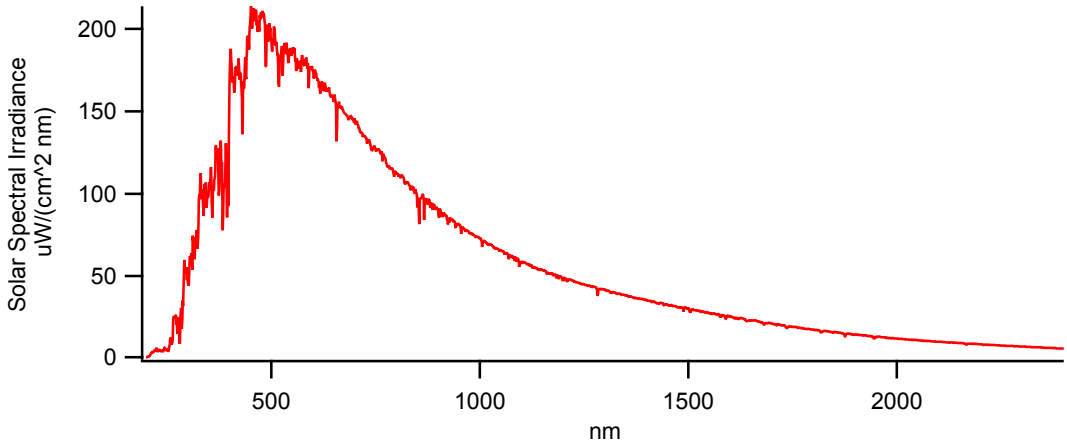

Figure 2.4: Solar Spectral Irradiance, F_0, from Thuillier et al 2003 [2].

2.1.2 Radiance Normalization

It is often useful to look at the normalized radiance. In the case of the cloud optical depth determined with the zenith radiance method, we will compare the measured radiance with the radiance modeled with a radiative transfer calculation, which is in units of normalized radiance. To normalize the radiometer data, we need to use a corrected solar irradiance. The solar irradiance on a unit horizontal area [3] varies with solar zenith angle, θ, as:

$$E = F_0 \cos(\theta) \tag{2.6}$$

where F_0 is the extra terrestrial direct normal solar irradiance. It is a common convention to denote:

$$\mu_0 = \cos(\theta). \tag{2.7}$$

The normalization constant would then be:

$$E_{nc} = \mu_0 \overline{F_0(\lambda \pm 5nm)} \tag{2.8}$$

where $\overline{F_0(\lambda \pm 5nm)}$ is the reference solar irradiance at the top of the atmosphere at wavelength λ, bandwidth averaged over a range of $\pm$ 5nm of a given wavelength

λ from the reference solar irradiance F_0. This provides a better match with the radiometer as its filters have a Full Width at Half Maximum (FWHM) of about 10 nm. We use the extra terrestrial solar irradiance provided in Thuillier[2], which is shown in Fig. 2.4. The normalized radiance has the form:

$$L_{norm} = \frac{L_{meas}}{E_{nc}} \tag{2.9}$$

where L_{meas} is the dark corrected radiance measured in units of $\frac{\mu W}{cm^2 nm\ sr}$ and E_{nc} is normalization constant.

2.2 Cimel Sunphotometer

At our Key Biscayne site, we have two AERONET Cimel Automated Sun-Sky Scanning Radiometer (ASSR) with identification numbers of #631 and #632. AERONET, a NASA project, consists of a network of Cimel sunphotometers located all over the world [31]. This instrument is capable of taking automated measurements of the sky radiance and direct solar irradiance at various angles in the sky. The device has a filter wheel and measures radiance at several wavelengths: 440, 675, 870, and 1020 nm. #632 included polarization measurements in addition to the different spectral channels. A time series comparing the AOD of the two Cimels can be seen in Fig. 2.5. My main interest with the Cimel is the aerosol optical depth calculated from the direct solar irradiance measurements. This data is very useful during data reduction of other devices. The micro-pulse lidar, for example, can use the Cimel aerosol optical depth as a reference to determine the micro-pulse lidar's measurement of optical depth and the backscatter coefficient. This is discussed in detail in a later chapter.

Our two devices, are located at Key Biscayne at a latitude and longitude of 25.73197 N, 80.16333 W degrees. They are placed side by side on a platform on top of the Marine Science Center on University of Miami RSMAS campus as shown in

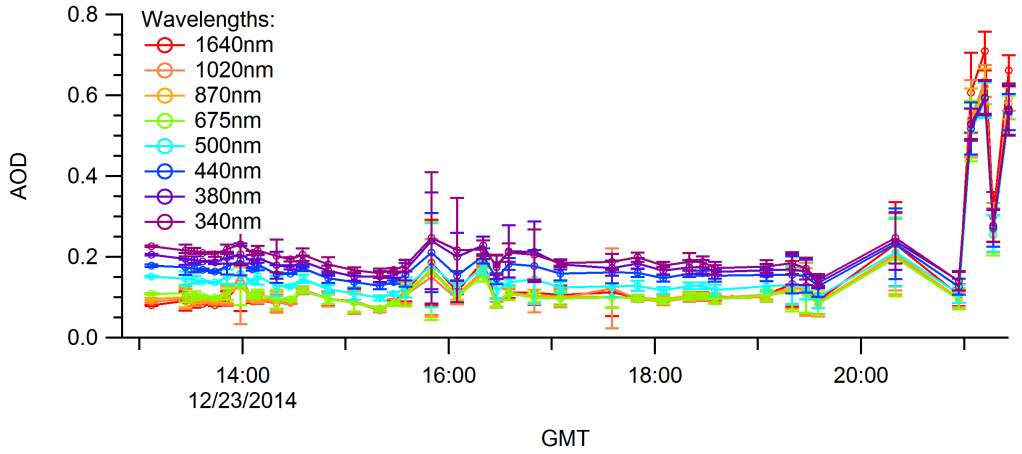

(a) Cimel #631 AOD.

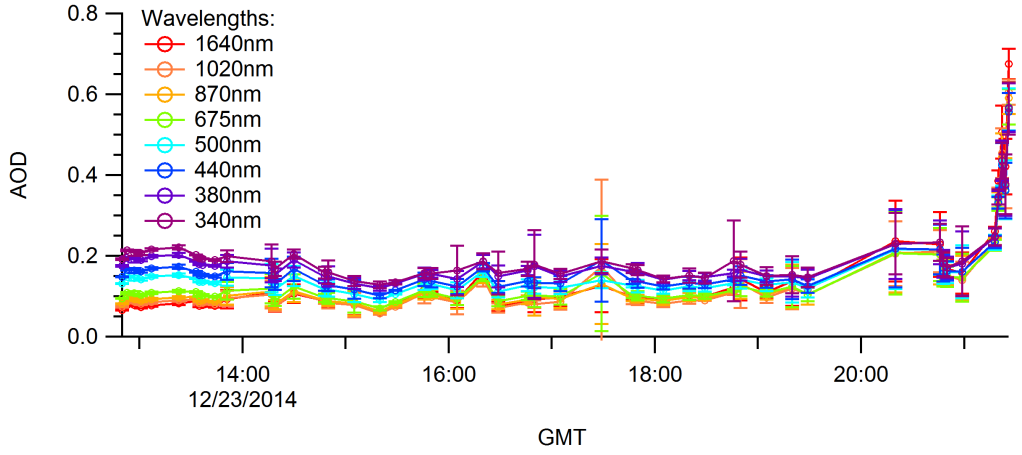

(b) Cimel #632 AOD.

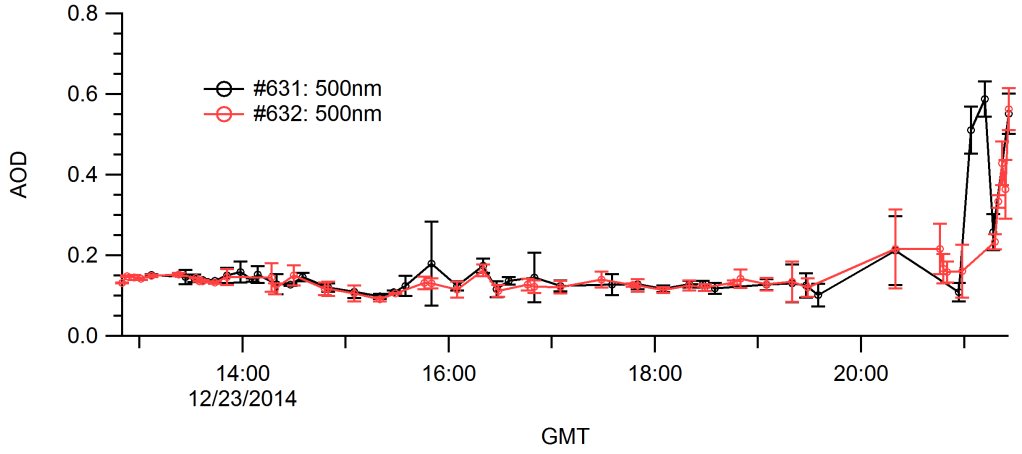

(c) Comparison between the two Cimels for 500 nm wavelength channel.

Figure 2.5: Aeronet Cimel AOD Time Series.

Figure 2.6: Aeronet Cimels at the Key Biscayne, FL: #632 on the left and #631 on the right

Fig. 2.6. They require routine maintenance since they have a tendency to become tangled on their own cables once every few months. This happens because the radiometer heads rotate to take measurements as the sun moves across the sky and the cables can become tangled in the process. This can happen if the instrument goes back to its park position from an awkward direction, or when strong winds cause the cables to tangle. In this case they must be manually untangled. Another problem is that a faulty or corroded wet sensor can cause the cimel to fail to realize that it is raining, and water can enter the device. When large problems like this occur, the instruments must be sent back to NASA's Goddard Space Flight Center (GSFC) for repair. Routine calibrations of the instrument are done at GSFC. With the two Cimels on location, when one is out for repair or calibration, the other is usually still in place and working well. This is a big advantage because the Cimel is required for calibrating the MPL.

We need aerosol optical depth for 532nm in our analysis of the MPL data. However, there is no corresponding channel in the Aeronet data. Consequently, we need to interpolate the Aeronet data to find the AOD corresponding to 532 nm by

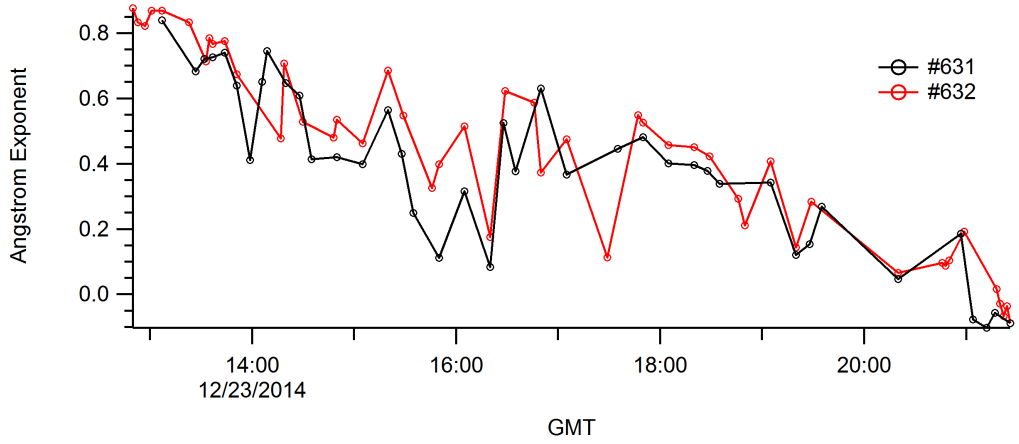

(a)

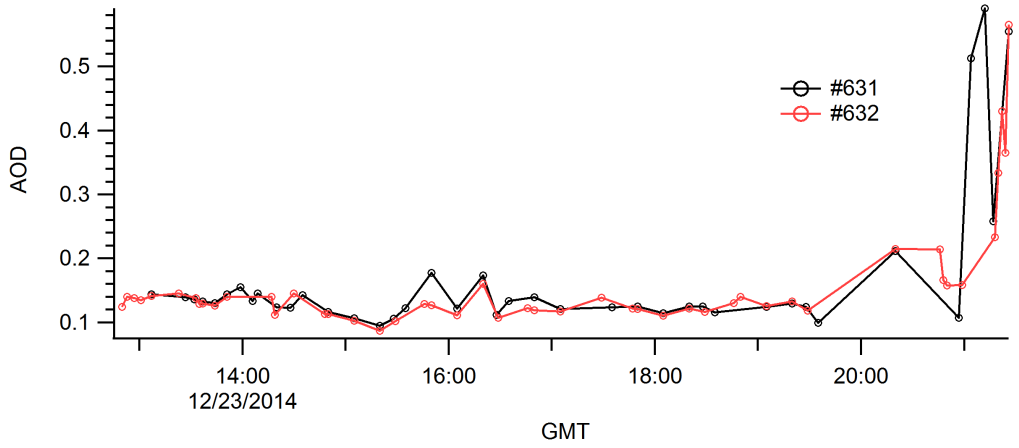

(b)

Figure 2.7: AOD interpolation. (a) Angstrom exponent time series found by fitting AOD from 500 to 870 nm to the Angstrom power law. (b) Interpolated 532nm AOD.

applying the Angstrom power law [32]:

$$\tau(\lambda) = \tau_1 \lambda^{-\alpha} \tag{2.10}$$

where α is the Angstrom exponent, τ_1 is the AOD at 1 μm, and $\tau(\lambda)$ is the AOD as a function of wavelength. Taking the ratio of Eq. 2.10 for two wavelengths and solving for $\tau(\lambda_2)$, we find:

$$\tau\left(\lambda_2\right) = \tau\left(\lambda_1\right)\left(\frac{\lambda_2}{\lambda_1}\right)^{-\alpha} \tag{2.11}$$

Figure 2.7a is an example of the Angstrom exponent provided by Aeronet. Using the Angstrom exponent and 500 nm AOD, we find the 532 nm AOD, which is shown in Fig. 2.7b.

2.3 Polarized Micro-Pulse Lidar

We used a polarized micro-pulse lidar (MPL) in the course of this research. It is a Sigma Space Model MPL-4B-IDS-532/POL-FS. The laser light wavelength is 532 nm, or green light. The laser sends pulses of light directly up into the sky and measures the returned signal as a function of the time to get a vertical profile of the aerosol properties. When the light encounters particles, some of it is backscattered. Since we know the speed of light, the time it takes for the light to get back is proportional to the distance traveled. The lidar collects the counts as a function of time into different bins with the size of bins determining the range resolution. For example a $200\,ns$ bin results in a resolution of 30 meters from:

$$\Delta y = 2c\Delta t \tag{2.12}$$

where Δy is the altitude bin, c is the speed of light, and Δt is the time bin. In our case, data beyond 25 km are usually too noisy to be of any use, but this is also beyond the range where we expect to find most aerosol particles. The MPL has a

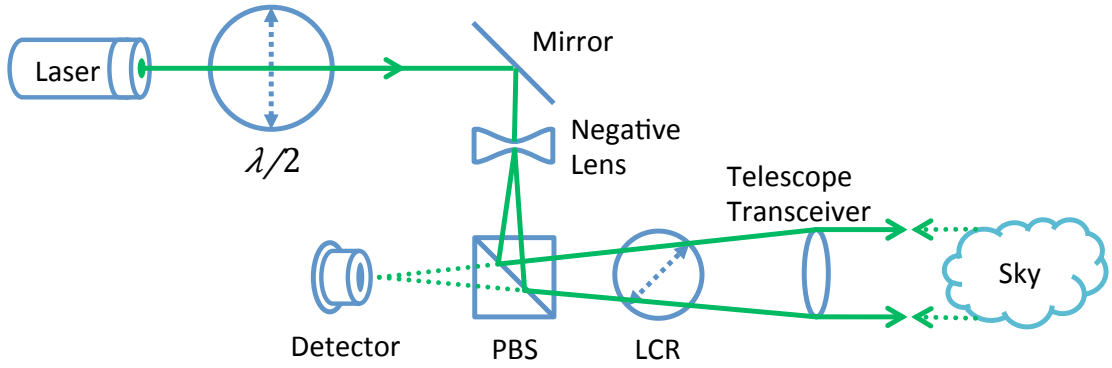

Figure 2.8: MPL Optical Layout: PBS is the polarizing beam splitter and LCR is the liquid crystal retarder.

weak pulse energy (6-8 μJ) but has a high pulse rate (2500 Hz) that is averaged to increase the signal while also remaining eye safe. The pulse width is 11 ns.

2.3.1 Depolarization Ratio

With polarization sensitivity, the lidar is capable of telling us something about the scattering particle (cloud or aerosol) shape. Ice clouds and irregularly shaped particles tend to have high depolarization; and water clouds or spherical particles tend to have very little, or no, depolarization [11]. Measurement of the depolarization is possible through the MPL's actively controlled liquid crystal retarder (LCR) [33]. The LCR varies the retardance of its fast axis depending on the voltage applied to the device. To better understand the design, we consider the optical layout shown in Fig. 2.8. The laser beam first goes through a half wave plate, which rotates the plane of polarization of the beam to match the polarizing beam splitter, then reflects off a mirror and goes through a negative lens to match the telescope and produce an output collimated beam. Next, the light goes into a polarizing beam splitter (PBS), which reflects the outgoing light at a 90 degree angle [33]. The laser light then travels through the LCR and the telescope transceiver. The signal backscattered in the atmosphere travels back down the optical system and to

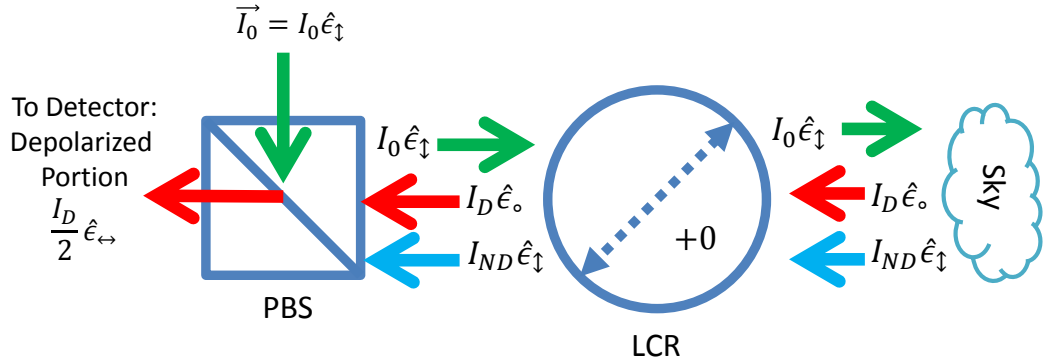

(a) LCR Mode 0 returns half of the unpolarized light to the detector as $\frac{I_D}{2}\hat{\epsilon}_\leftrightarrow$.

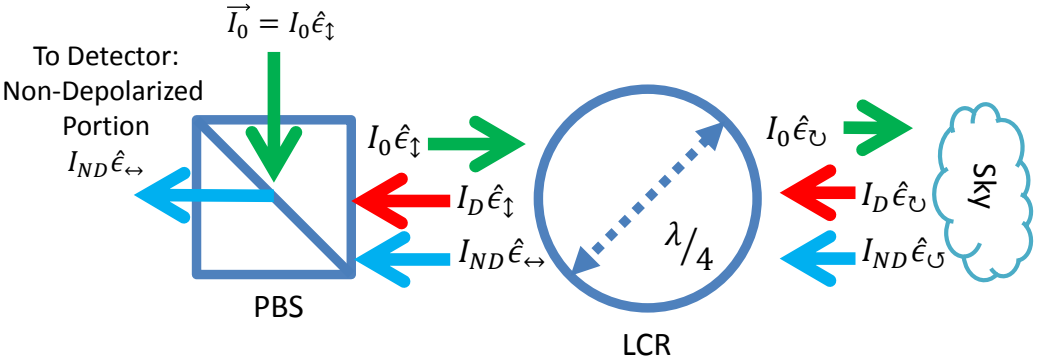

(b) LCR Mode 1 returns the non-depolarized portion to the detector as $I_{ND}\hat{\epsilon}_\leftrightarrow$.

Figure 2.9: The LCR functions as a waveplate with fast axis set to 45° and switches retardance between 0 (mode 0) and $\lambda/4$ (mode 1) in order to measure depolarized (I_D) and non-depolarized (I_{ND}) portions of the backscattered light from the atmosphere. Since the PBS transmits horizontal $\hat{\epsilon}_\leftrightarrow$ and reflects vertical $\hat{\epsilon}_\updownarrow$ polarization, only horizontally polarization $\hat{\epsilon}_\leftrightarrow$ returns to the detector.

the PBS, which only transmits light orthogonal to the original polarization state through to the detection optics, which includes a pinhole aperture, filters, focusing lenses, and finally the photo detector.

Given that each optical element has a Mueller matrix[34], we can find the Stokes vectors at different stages of the optical layout. In this setup, we will refer to five polarization states:

$$\hat{\epsilon}_\updownarrow = \begin{pmatrix} 1 \\ -1 \\ 0 \\ 0 \end{pmatrix}, \hat{\epsilon}_\leftrightarrow = \begin{pmatrix} 1 \\ 1 \\ 0 \\ 0 \end{pmatrix}, \hat{\epsilon}_\circlearrowleft = \begin{pmatrix} 1 \\ 0 \\ 0 \\ -1 \end{pmatrix}, \hat{\epsilon}_\circlearrowright = \begin{pmatrix} 1 \\ 0 \\ 0 \\ 1 \end{pmatrix}, \hat{\epsilon}_\circ = \begin{pmatrix} 1 \\ 0 \\ 0 \\ 0 \end{pmatrix} \quad (2.13)$$

where $\hat{\epsilon}_\updownarrow$ is vertical linear, $\hat{\epsilon}_\leftrightarrow$ is horizontal linear, $\hat{\epsilon}_\circlearrowleft$ is left-handed circular, $\hat{\epsilon}_\circlearrowright$ is

right-handed circular, and $\hat{\epsilon}_\circ$ is unpolarized. The laser light starts out as vertical linear:

$$\overrightarrow{I_0} = I_0 \hat{\epsilon}_\updownarrow \tag{2.14}$$

The PBS acts as a linear polarizer with vertical polarization for reflection and horizontal polarization for transmission. The PBS Mueller matrices will be [34]:

$$M_{LPV} = \frac{1}{2}\begin{bmatrix} 1 & -1 & 0 & 0 \\ -1 & 1 & 0 & 0 \\ 0 & 0 & 0 & 0 \\ 0 & 0 & 0 & 0 \end{bmatrix}, M_{LPH} = \frac{1}{2}\begin{bmatrix} 1 & 1 & 0 & 0 \\ 1 & 1 & 0 & 0 \\ 0 & 0 & 0 & 0 \\ 0 & 0 & 0 & 0 \end{bmatrix} \tag{2.15}$$

where M_{LPV} is for reflection and M_{LPH} and for transmission. Applying the first reflection of the PBS:

$$\overrightarrow{I_1} = M_{LPV}\overrightarrow{I_0} = \overrightarrow{I_0} \tag{2.16}$$

we see that the polarization state is unaltered.

Next in the path is the LCR, which oscillates back and forth between two retardances, controlled by an electronic signal. The process is summarized in Fig. 2.9. In Mode 0, the LCR is set to 0 retardance and acts as a clear piece of glass. In Mode 1, the LCR keeps the same fast axis at 45° with retardance of $\lambda/4$. For the LCR we use the Mueller matrix corresponding to a linear retarder with retardance φ and fast axis $\pm 45°$:

$$M_{LCR}(\varphi, \pm 45°) = \begin{bmatrix} 1 & 0 & 0 & 0 \\ 0 & \cos(\varphi) & 0 & \mp\sin(\varphi) \\ 0 & 0 & 1 & 0 \\ 0 & \pm\sin(\varphi) & 0 & \cos(\varphi) \end{bmatrix} \tag{2.17}$$

where φ is 0 for mode 0 and $\pi/2$ for mode 1. As the light traveling towards the sky goes through the LCR it sees a fast axis at $+45°$ but backscattered light from the atmosphere sees the reverse sense of the fast axis, or $-45°$. The intensity exiting

the LCR is:

$$\overrightarrow{I_2} = M_{LCR}(\varphi, 45^\circ)\,\overrightarrow{I_0} = I_0 \begin{pmatrix} 1 \\ -cos(\varphi) \\ 0 \\ -sin(\varphi) \end{pmatrix} = \begin{cases} I_0\hat{\epsilon}_{\updownarrow} & \text{for} \quad \varphi = 0 \\ I_0\hat{\epsilon}_{\circlearrowleft} & \text{for} \quad \varphi = \pi/2 \end{cases} \tag{2.18}$$

where $\overrightarrow{I_2}$ is vertical for mode 0 and left hand circular for mode 1.

The laser light then interacts with the atmosphere. To describe the scattering matrix for the atmosphere we consider single scattering of particles with a plane of symmetry and random orientation along the line of sight [33]:

$$M_{ATM} = a \begin{bmatrix} 1 & 0 & 0 & 0 \\ 0 & 1-d & 0 & 0 \\ 0 & 0 & d-1 & 0 \\ 0 & 0 & 0 & 2d-1 \end{bmatrix} \tag{2.19}$$

where a is proportional to the magnitude of the return signal and d the depolarization of the atmosphere, d=0 corresponds to no depolarization while d=1 corresponds to full depolarization. The backscattered light would be:

$$\overrightarrow{I_3} = M_{ATM}\overrightarrow{I_2} = aI_0 \begin{pmatrix} 1 \\ -(1-d)cos(\varphi) \\ 0 \\ -(2d-1)sin(\varphi) \end{pmatrix} = \begin{cases} I_D\hat{\epsilon}_{\circ} + I_{ND}\hat{\epsilon}_{\updownarrow} & \text{for} \quad \varphi = 0 \\ I_D\hat{\epsilon}_{\circlearrowleft} + I_{ND}\hat{\epsilon}_{\circlearrowleft} & \text{for} \quad \varphi = \pi/2 \end{cases} \tag{2.20}$$

where I_D and I_{ND} represent the depolarized and non-depolarized portions.

$$I_D = adI_0 \quad \text{and} \quad I_{ND} = a(1-d)I_0 \tag{2.21}$$

The portion of the linearly polarized light that is not depolarized returns with its original polarization. However, when circularly polarized light undergoes backscatter the rotational-sense flips. The part that comes back right-handed actually corresponds to original left-handed state.

When the light goes back through the LCR it sees a fast axis with -45° since its reference frame is flipped on the trip back. The result is:

$$\overrightarrow{I_4} = M_{LCR}(\varphi, -45^\circ)\,\overrightarrow{I_3} \tag{2.22}$$

$$= aI_0 \begin{pmatrix} 1 \\ -(1-d)cos^2(\varphi) - (2d-1)sin^2(\varphi) \\ 0 \\ (1-d)sin(\varphi)cos(\varphi) - (2d-1)sin(\varphi)cos(\varphi) \end{pmatrix} \tag{2.23}$$

$$= \begin{cases} I_D\hat{\epsilon}_\circ + I_{ND}\hat{\epsilon}_\updownarrow & \text{for} \quad \varphi = 0 \\ I_D\hat{\epsilon}_\updownarrow + I_{ND}\hat{\epsilon}_\leftrightarrow & \text{for} \quad \varphi = \pi/2 \end{cases} \tag{2.24}$$

Notice that for $\varphi = \pi/2$ the left-hand circular part has become vertical and the right-hand circular part has become horizontal. In order to make it to the detector, the light has to transmit through the PBS, but this only happens for horizontal polarization. The vertical polarization will be reflected at the PBS, thus essentially lost to the receiver/detector as far as we are concerned. For mode 0, only half of the depolarized light transmits to the detector since the unpolarized light contains equal parts horizontal and vertical polarization. For mode 1, the non-depolarized portion is transmitted. We can also see this by applying the PBS matrix. The intensity of the light reaching the detector is:

$$\overrightarrow{I_F} = M_{LPH}\overrightarrow{I_4} = \frac{aI_0}{2}\left(1 - (1-d)\cos^2(\varphi) - (2d-1)\sin^2(\varphi)\right)\hat{\epsilon}_\leftrightarrow \tag{2.25}$$

For the intensity of the two modes we get:

$$\begin{array}{rl} \overrightarrow{I_F}(0) = \frac{adI_0}{2}\hat{\epsilon}_\leftrightarrow = \frac{I_D}{2}\hat{\epsilon}_\leftrightarrow & \text{for} \quad \varphi = 0 \\ \overrightarrow{I_F}(\pi/2) = aI_0\,(1-d)\,\hat{\epsilon}_\leftrightarrow = I_{ND}\hat{\epsilon}_\leftrightarrow & \text{for} \quad \varphi = \pi/2 \end{array} \tag{2.26}$$

The MPL only saves the intensity of the return signal, not the other Stokes vector components. Ultimately, we combine these two channels to measure the depolarization. The mpl depolarization ratio is:

$$\delta_{MPL} = \frac{\left|\overrightarrow{I_F}(0)\right|}{\left|\overrightarrow{I_F}(\pi/2)\right|} = \frac{d}{2(1-d)} \tag{2.27}$$

However, many descriptions of scattering particles in the literature often refer to their linear depolarization which is defined as the ratio of the perpendicular and parallel components of the backscatter intensities. The linear depolarization ratio

is:

$$\delta_{linear} = \frac{I_{\perp}}{I_{\parallel}} \tag{2.28}$$

In the case of the MPL, you can think of these as horizontal and vertical component of the backscatter intensity $\overrightarrow{I_4}$ before hitting the PBS, or:

$$I_{\perp} = \hat{\epsilon}_{\leftrightarrow} \cdot \overrightarrow{I_4}(0) = \frac{adI_0}{2} \tag{2.29}$$

$$I_{\parallel} = \hat{\epsilon}_{\updownarrow} \cdot \overrightarrow{I_4}(0) = aI_0(1 - \frac{d}{2}) \tag{2.30}$$

The corresponding linear depolarization ratio would then be:

$$\delta_{linear} = \frac{I_{\perp}}{I_{\parallel}} = \frac{d}{2 - d} \tag{2.31}$$

Solving for d from Eq. 2.27, and substituting into Eq. 2.31 we can find the relationship between the linear and MPL depolarization ratios:

$$\delta_{linear} = \frac{\delta_{MPL}}{1 + \delta_{MPL}} \tag{2.32}$$

This relationship between the MPL and linear depolarizations are predicated on the fact that the particle in the atmosphere have a scattering matrix described by Eq. 2.19. However, the Mueller matrix is always changing and in some cases this approximation may not be applicable. For example if the aerosol or cloud particles are not randomly oriented the relationship shown in Eq. 2.32 could be different. Other cases of concern could be if the atmosphere changes faster than the averaging time (15 sec) leading to incorrect ratios. Clouds with quickly changing phase or largely mixing phase could lead to inconsistencies in the measurement. Conversely, as long as the scattering particles do not change quickly and are well represented by the scattering matrix shown, the depolarization ratio will give insight into the particle shape. We also assume that the atmosphere, in the absence of particles, itself does not depolarize the lidar signal due to effects such as turbulence. This is because our lidar pulses are long, with a larger beam cross section, relative to those needed to sense turbulance [35].

2.3.2 The Lidar Equation

Our goal is to extract the aerosol optical depth and backscatter coefficient from the lidar signal. To do this, we start with the lidar equation, which describes the signal that the lidar receiver measures. The raw MPL signal in counts/μsec [36] is:

$$\mathrm{RAW}(r) = \frac{1}{D\left(\mathrm{RAW}(r)\right)}\left(\frac{C \times E \times O(r)\left[\beta(r)e^{-2\tau(r)}\right]}{r^2} + A(r,E) + B(r,E)\right) \tag{2.33}$$

where r is the range, $D\left(\mathrm{RAW}(r)\right)$ is the detector dead time, C is the lidar constant, E is the lidar pulse energy, $O(r)$ is the overlap function, $A(r,E)$ is the afterpulse, and $B(r,E)$ is the background signal, β is the total backscatter coefficient, and τ is the total integrated optical path length, defined as the integral of the extinction coefficient from the surface to an altitude r:

$$\tau(r) = \int_0^r \sigma(r')\,\mathrm{d}r' \tag{2.34}$$

where σ is the the volume extinction coefficient in units of $1/m$. When r goes to infinity, the integrated optical path length is equivalent to the optical depth τ. The total backscatter coefficient and integrated optical path length have contributions from both aerosol (β_A, τ_A) and Rayleigh (β_R, τ_R) scattering.

$$\tau(r) = \tau_R(r) + \tau_A(r) \tag{2.35}$$

$$\beta(r) = \beta_R(r) + \beta_A(r) \tag{2.36}$$

It also useful to define the backscatter to extinction coefficient R as:

$$R_i \equiv \frac{\beta_i}{\sigma_i} \text{ in } \mathrm{sr}^{-1} \tag{2.37}$$

where $i = A$ for aerosol, and $i = R$ for Rayleigh. With the backscatter to extinction coefficient R_i we can find the components of the integrated optical path length $\tau_i(r)$

from the backscatter coefficient β_i, assuming constant R_i:

$$\tau_i(r) = \int_0^r \frac{\beta_i(r')}{R_i}\,\mathrm{d}r' \tag{2.38}$$

To retrieve the aerosol data, we remove the pulse energy E, the overlap function $O(r)$, the afterpulse $A(r,E)$, the background signal $B(r,E)$, the detector dead time $D\left(\text{RAW}(r)\right)$, and the range ,$r^2$, terms from the raw MPL signal[37]. The resulting signal is called the normalized relative backscatter, or NRB:

$$\text{NRB}(r) = \frac{\text{RAW}(r)D\left(\text{RAW}(r)\right) - A(r,E) - B(r,E)}{E \times O(r)} r^2 \tag{2.39}$$

which results in:

$$\text{NRB}(r) = C\beta(r)e^{-2\tau(r)} \tag{2.40}$$

2.3.3 The Rayleigh Signal

We want the aerosol information, but how do we discern the aerosol and the Rayleigh part of our signal and what about the lidar constant C? Fortunately, Rayleigh scattering is well known and well developed. Reconstruction of the Rayleigh optical depth and backscatter will allow us to remove it from the NRB signal. It is possible to reconstruct the Rayleigh component using the 1976 US Standard Atmosphere [38] pressure profile $P(r)$ and following Hansen and Travis [7]:

$$\tau_R(r) = \tau_0\left(1 - \frac{P(r)}{P_0}\right) \tag{2.41}$$

$$\tau_0 = 0.008569\lambda^{-4}\left[1 + 0.0113\lambda^{-2} + 0.00013\lambda^{-4}\right] \tag{2.42}$$

$$P_0 = 101,325 \text{ Pa} \tag{2.43}$$

where P_0 the surface level standard atmospheric pressure. We find the Rayleigh backscatter coefficient $\beta_r(r)$ by taking the derivative of the Rayleigh optical depth with respect to height in Eq. 2.38 to get:

$$\beta_R(r) = R_R\frac{\mathrm{d}\tau_R(r)}{\mathrm{d}r} \tag{2.44}$$

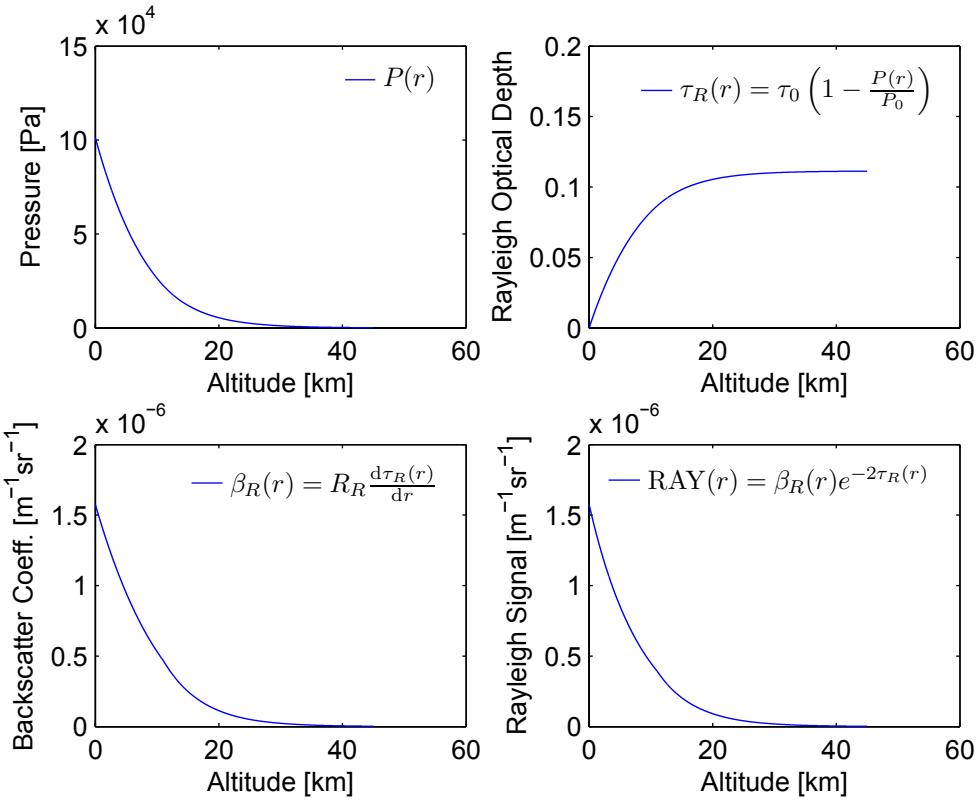

Figure 2.10: Rayleigh Profile using 1976 US Standard Atmosphere

The Rayleigh backscatter to extinction ratio $R_R(r)$ is $3/8\pi$ sr^{-1}. We can now reconstruct the Rayleigh part of the MPL signal, RAY(r), as:

$$\text{RAY}(r) = \beta_R(r) e^{-2\tau_R(r)} \tag{2.45}$$

When aerosols are not present, the Rayleigh component of the NRB in Eq. 2.40 dominates. The Saharan dust layer we are most interested in typically does not extend above 5 km in altitude. We define the top of the aerosol layer as r_{max}.

Above r_{max} using Equations 2.36 and 2.40 we get:

$$\beta_A(r) \rightarrow 0 \tag{2.46}$$

$$\beta(r) \rightarrow \beta_R(r) \tag{2.47}$$

$$\mathrm{NRB}(r) \rightarrow C\beta_R(r)e^{-2\tau_R(r)}e^{-2\tau_A(r)} \tag{2.48}$$

$$\mathrm{NRB}\,(r >= r_{max}) = Ce^{-2\tau_A}\mathrm{RAY}(r) \tag{2.49}$$

Since the aerosol backscatter coefficient approaches zero above r_{max}, the integrated path length stops changing. This can be seen by breaking the integral into two parts to get:

$$\tau_A(r > r_{rmax}) = \int_0^{r_{max}} \frac{\beta_A(r')}{R_i}\,\mathrm{d}r' + \int_{r_{max}}^{r} \frac{\beta_A(r')}{R_i}\,\mathrm{d}r' \to 0 \tag{2.50}$$

where the term on the right vanishes given $\beta_A \rightarrow 0$ above r_{max}. The aerosol optical depth is defined as:

$$\tau_A = \int_0^{\infty} \frac{\beta_A(r')}{R_i}\,\mathrm{d}r' \tag{2.51}$$

but if $\beta_A(r') \rightarrow 0$ above r_{max}:

$$\tau_A = \int_0^{r_{max}} \frac{\beta_A(r')}{R_i}\,\mathrm{d}r' = \tau_A(r > r_{rmax}) \tag{2.52}$$

The NRB above r_{max} is:

$$\mathrm{NRB}\,(r >= r_{max}) = Ce^{-2\tau_A}\mathrm{RAY}(r) \tag{2.53}$$

2.3.4 The Lidar Constant

The NRB above the aerosol layer, found in Equation 2.53, has two unknowns: the lidar constant C and the aerosol optical depth $\tau_A(r)$. If we know either one of them, we can use the MPL data to find the other. For example, if we have an independent measurement of aerosol optical depth, we can find the lidar constant C. At the Key Biscayne site on a building in the University of Miami RSMAS campus, as

part of South Florida's Cloud-Aerosol-Rain Observatory (CAROb), we have two AERONET Cimels collecting aerosol optical depth data. These sun photometers work well, but have the disadvantage that they can only operate during the day, as the name implies. However, the MPL is always on, day and night.

Using the AERONET aerosol optical depth data during the day, we calculate the lidar constant C by a least squares curve fit to the Rayleigh component $\mathrm{RAY}(r)$.

$$C = \frac{\mathrm{NRB}\,(r >= r_{max})\, e^{2\tau_A(r)}}{\mathrm{RAY}(r)} \tag{2.54}$$

Once we settle on a value of C, we can then find $\tau_A(r_{max})$ for night time data also using our MPL data, which is coincidentally the cleanest MPL data. During the day, the lidar signal has noise due to background solar light, which obviously goes away at night. Coincidentally, this results in a synergy between the Cimel and MPL to obtain a complete τ_A record. The lidar constant C is largely dependent on cleanliness of the lidar window. With this in mind, one must calibrate against the Cimel to find C at least every three days. In this work, we calibrate the MPL against the Cimel daily.

The challenge becomes finding the aerosol boundary, r_{max}. We varied the starting altitude, r_{start}, of the fit to find the best coefficient of determination, R^2, which is defined as [39]:

$$R^2 = 1 - \frac{SS_{res}}{SS_{tot}} \tag{2.55}$$

where SS_{res} is the residual sum of squares:

$$SS_{res} = \sum_i (f_i - \overline{y})^2 \tag{2.56}$$

and SS_{tot} is the total sum of squares:

$$SS_{tot} = \sum_i (y_i - \overline{y})^2 \tag{2.57}$$

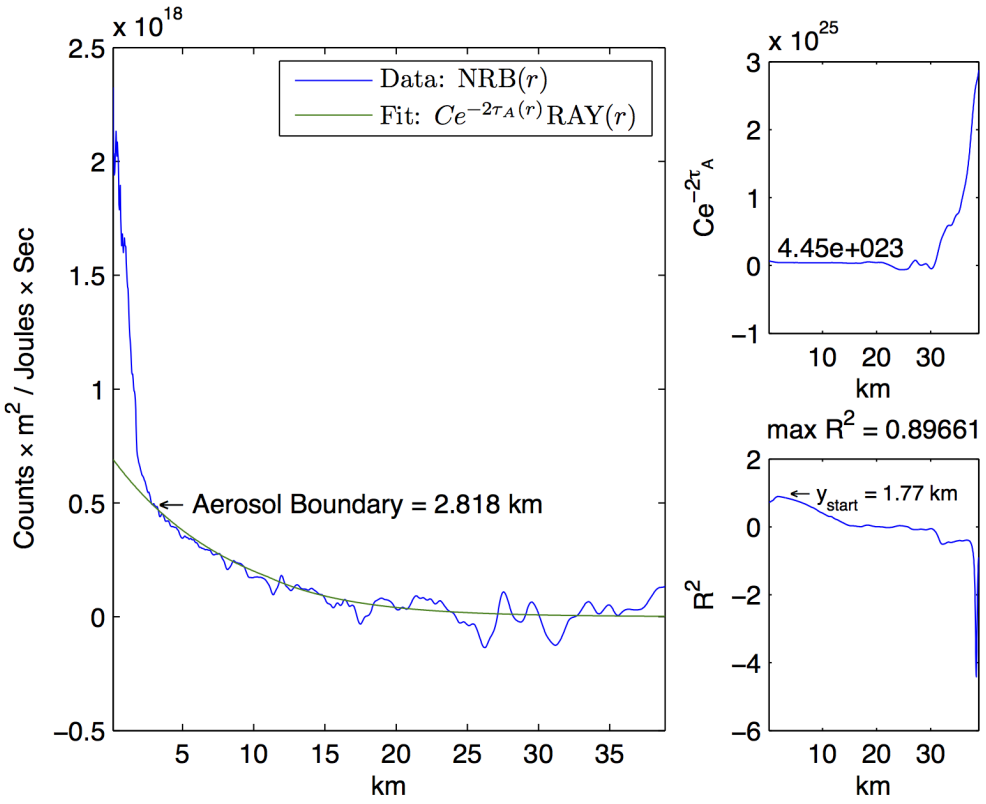

Figure 2.11: Rayleigh fit to NRB data

where f_i is the model, y_i is the data, and $\overline{y}$ is the average data. $R^2 = 0$ means that the Rayleigh Model RAY(r) does not explain the variation in NRB(r), and $R^2 = 1$ means it explains the variation perfectly. Above 25 km, R^2 is dominated by noise resulting in poor fits to the Rayleigh Model. With Eq. 2.55, the estimates of R^2 can become negative, as in Fig. 2.11, when the residual sum of squares is bigger than the total sum of squares, meaning that the average of the data is a better representation than the Rayleigh model for altitude above 25 km. The best r_{start} specifies the altitude at which the data best fits the pure Rayleigh component.

The starting altitude, r_{start}, did not always turn out to be the same as r_{max}. Often, r_{max} was above r_{start}. Visual inspection often shows clearly where r_{max} is located (Fig. 2.11). Starting from bottom to top, it is where the Rayleigh fit

starts to align with the NRB data. Using this idea, starting from the surface level altitude, I created an algorithm to find where the model fit first intersects the data and defined this to be r_{max}.

Once C is known, we are not limited to just the column aerosol optical depth τ_A. We can also find the volume extinction profile $\sigma(r)$ and the backscatter profile $\beta_a(r)$ through the Fernald lidar inversion algorithm, which will be discussed in detail in Chapter 3.

Chapter 3

MPL Measured Cloud and Aerosol Optical Depth

The aerosol optical depth can be found from the MPL NRB profile when calibrated against an independent instrument, such as the Aeronet Cimel. Once the aerosol optical depth is known, the aerosol extinction and volume backscatter profiles can be inverted from the MPL NRB signal. I've used two inversion techniques to do this. One inversion relies on having an independent simultaneous aerosol optical depth measurement, which I refer to as the "Lidar Fernald Inversion with AOD," where "AOD" stands for aerosol optical depth. The need for an independent measurement reasserts the importance of having the Cimel sun photometers on location. The other inversion relies on having a known lidar constant, which I refer to as the "Lidar Fernald Inversion with C," where "C" stands for the lidar constant, C. In this Chapter, I will discuss these two inversion techniques, along with their similarities and differences. This will include measured aerosol extinction and backscatter profiles for a sample date.

We have years of data to pick from, but it would be too much to show and the selection shown is a good representation of the other data. We started by calibrating the raw co-polarized MPL channel to find the co-polarized NRB (Normalized Relative Backscatter) (Fig. 3.1), which is then inverted to find aerosol extinction and backscatter. Ultimately, we want to retrieve cloud optical depth from NRB. Consequently, we will end the chapter by describing cloud optical depth retrievals from MPL data.

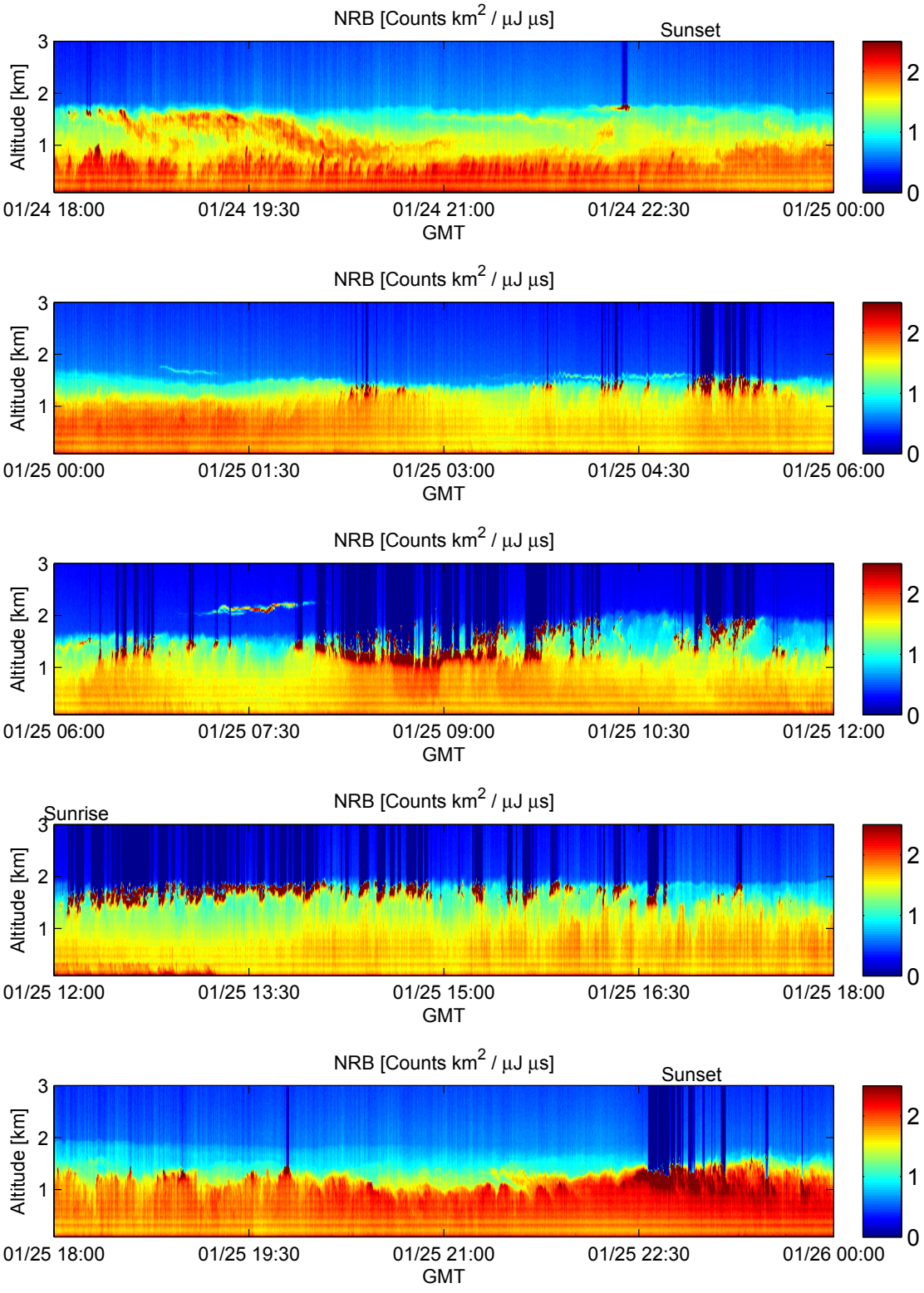

Figure 3.1: NRB co-polarized signal.

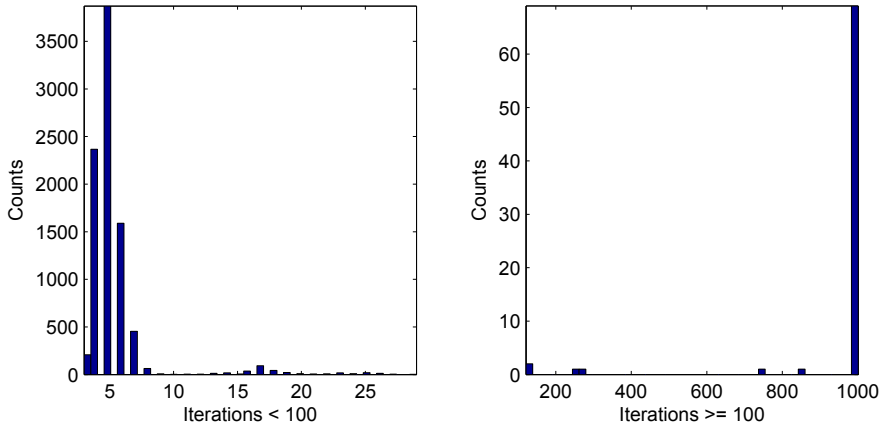

Figure 3.2: Histogram of the number of iterations taken in the Fernald Loop, 1/24/2013 17:16:24 to 1/26/2013 11:59:55 GMT

3.1 Lidar Fernald Inversion with AOD

Standard practice is to use the Fernald lidar inversion algorithm to find the aerosol profile properties by constraining to a known AOD [40]. This approach assumes a vertically homogeneous value for R_A which in turn depends on a vertically constant aerosol size distribution. It starts at the top of the aerosol layer r_{max} where the aerosol backscatter coefficient β_a is zero. Then, using the recursive Fernald algorithm (Eq. 3.1) [41], the backscattering coefficient for the next altitude point below this point can be found, and this process is repeated until reaching the surface. The Fernald lidar inversion can be summarized as:

$$\beta_A(n-1) = \frac{\mathrm{NRB}(n-1)\Psi(n)}{\dfrac{\mathrm{NRB}(n)}{\beta(n)} + \dfrac{\Delta r}{R_A}\left[\mathrm{NRB}(n) + \mathrm{NRB}(n-1)\Psi(n)\right]} - \beta_R(n-1), \quad (3.1)$$

where:

$$\Psi(n) = \exp\left(\left[\frac{1}{R_A} - \frac{1}{R_R}\right]\left[\beta_R(n-1) + \beta_R(n)\right]\Delta r\right). \quad (3.2)$$

The first iteration starts with an $R_A = 1$, which is quickly updated to a more realistic value after one iteration of the Fernald loop. After the entire aerosol backscatter profile $\beta_A(r)$ is found, we can re-arrange Eq. 2.38 to find the new

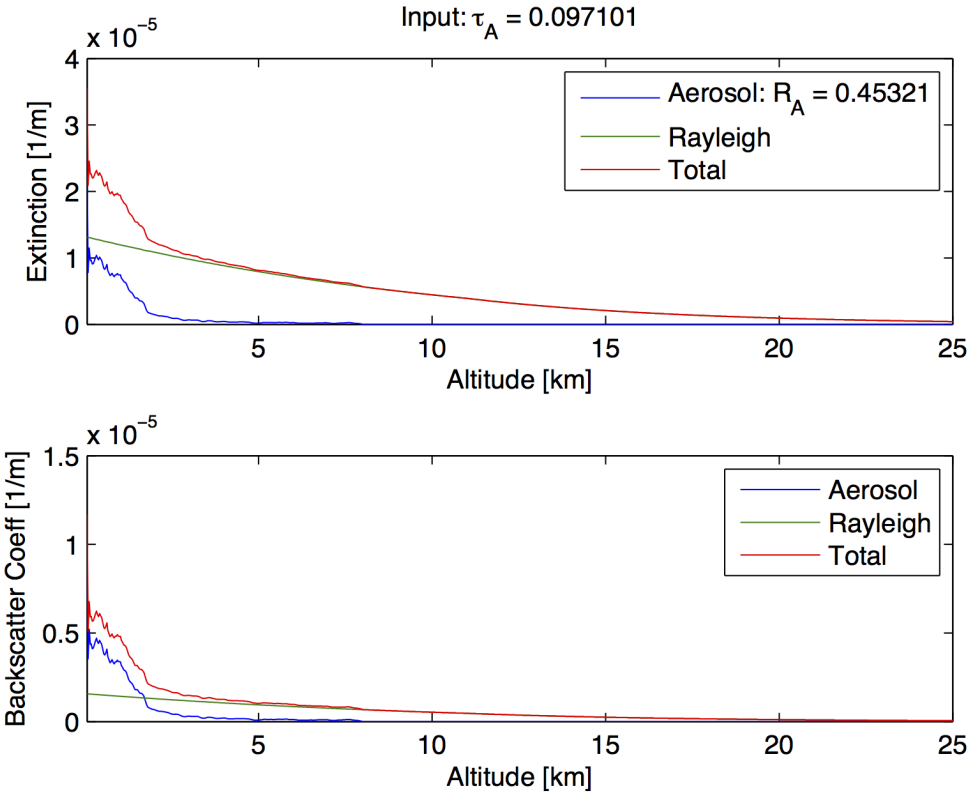

Figure 3.3: Extinction and backscatter profile generated with Fernald algorithm and an independently measured Aerosol optical depth (Aeronet data), 1/24/2013 20:41:57.

backscatter to extinction Ratio:

$$R_{new} = \frac{\int_0^{r_{max}} \beta_A(r')\,\mathrm{d}r'}{\tau_A(r_{max})}. \tag{3.3}$$

Then, we use R_{new} in the Fernald inversion (Eq. 3.1) and proceed to calculate the $\beta_A(r)$ profile again. This process continues until R_{new} changes by less than 5% of its previous value. The Fernald inversion takes an average of 5 iterations to reach a stable R_A, see Fig. 3.2. The aerosol extinction then is simply $\frac{\beta_A(r)}{R_A}$, and the aerosol optical depth can be found by:

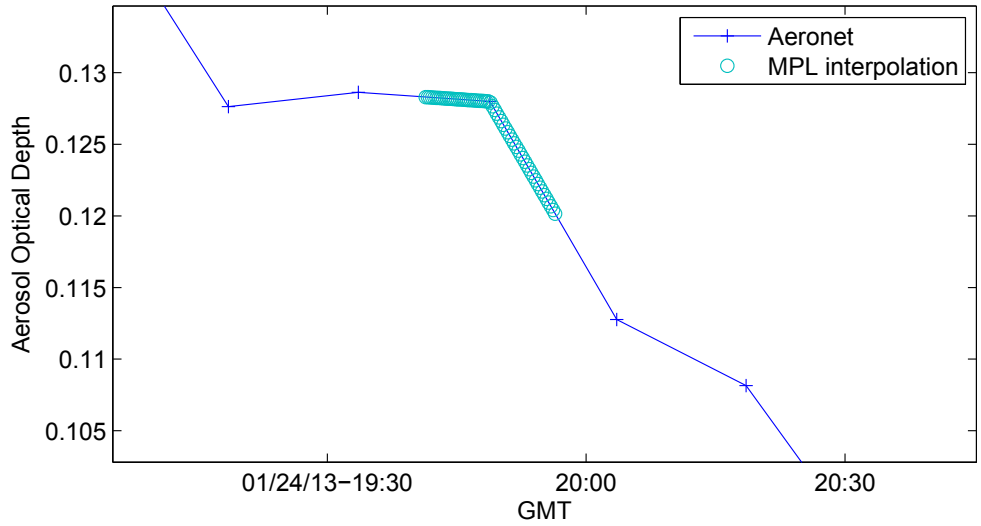

Figure 3.4: Aeronet AOD and the interpolation values used by MPL Inversion. The Aeronet AOD is obtained over a time resolution of 15 minutes (1 min time average per data point) and the MPL is a result of a 15 s average.

$$AOD = \tau_A = \int_0^{r_{max}} \frac{\beta_A(r')}{R_A}\, \mathrm{d}r'. \tag{3.4}$$

Figure 3.3 shows an example of a profile inverted using the Fernald inverson with AOD technique.

As an example we will focus on MPL data from 1/24/2013 18:00 to 1/26/2013 00:00 GMT. This specific time was picked because it corresponds to a time when we have good Aeronet data from Cimel #631 and the lidar had just come back from repair.

Although we have MPL data consistently throughout the time frame between 1/25/2013 17:00 to 1/26/2013 00:00 GMT, there is limited Aeronet data. It does not make sense to interpolate AOD values to all the MPL data in this time frame. Instead, we limit the MPL data to within one hour of the Aeronet data and we linearly interpolate the AOD data to the MPL data in this 1 hour interval. An example of the interpolation can be seen in Fig. 3.4. The Aeronet AOD has a time interval of about 20 min and the MPL has a time interval of 15 sec.

The aerosol backscatter profiles found using the inversion with AOD are shown in Fig. 3.5. Most of the aerosols are located in altitudes less than 2 km. There is a cloud period between 1/25/13 13:00 to 15:00 GMT leading to a large aerosol backscatter coefficient greater than 6×10^{-3} km^{-1} in the cloud layer. By dividing the backscatter β_A by the backscatter to extinction ratio R_a, we can also produce aerosol extinction σ_A profiles, see Fig 3.6. The cloud period has aerosol extinction greater than 0.1 km^{-1}. For 1/25/13 15:00 to 16:00 GMT there is a gap in data because there is no Aeronet AOD data for that time period. The reason is because we used level 1.5 Aeronet AOD, which is cloud screened. However, Aeronet's filtering scheme failed to filter out the clouds between 1/25/13 13:00 to 15:00 GMT. The Aeronet Cimel is not capable of retrieving accurate AOD in the presence of clouds. Consequently, we should not expect the Fernald inversion with AOD to work well for cloudy periods. This limitation is why we are interested in developing the Fernald inversion with C. The idea being that we want to establish a good C number (the LIDAR constant) during cloud free scenarios by calibrating to Aeronet AOD in order to apply that C number to cloudy periods and retrieve the cloud optical properties.

3.2 Lidar Fernald Inversion with C

We can use the same equations in the Fernald inversion (Eq. 3.1) to calculate aerosol extinction profiles using a previously determined calibration coefficient, C, which is calibrated to Aeronet AOD during cloud free skies daily. The calibration procedure for C is discussed in the previous chapter. To find aerosol extinction, we just have to replace the $\tau_A(r_{max})$ in Eq. 3.3 with one determined from the lidar constant C. Above the aerosol layer, the NRB equation becomes:

$$\mathrm{NRB}\,(r) = Ce^{-2\tau_A}\mathrm{RAY}(r). \tag{3.5}$$

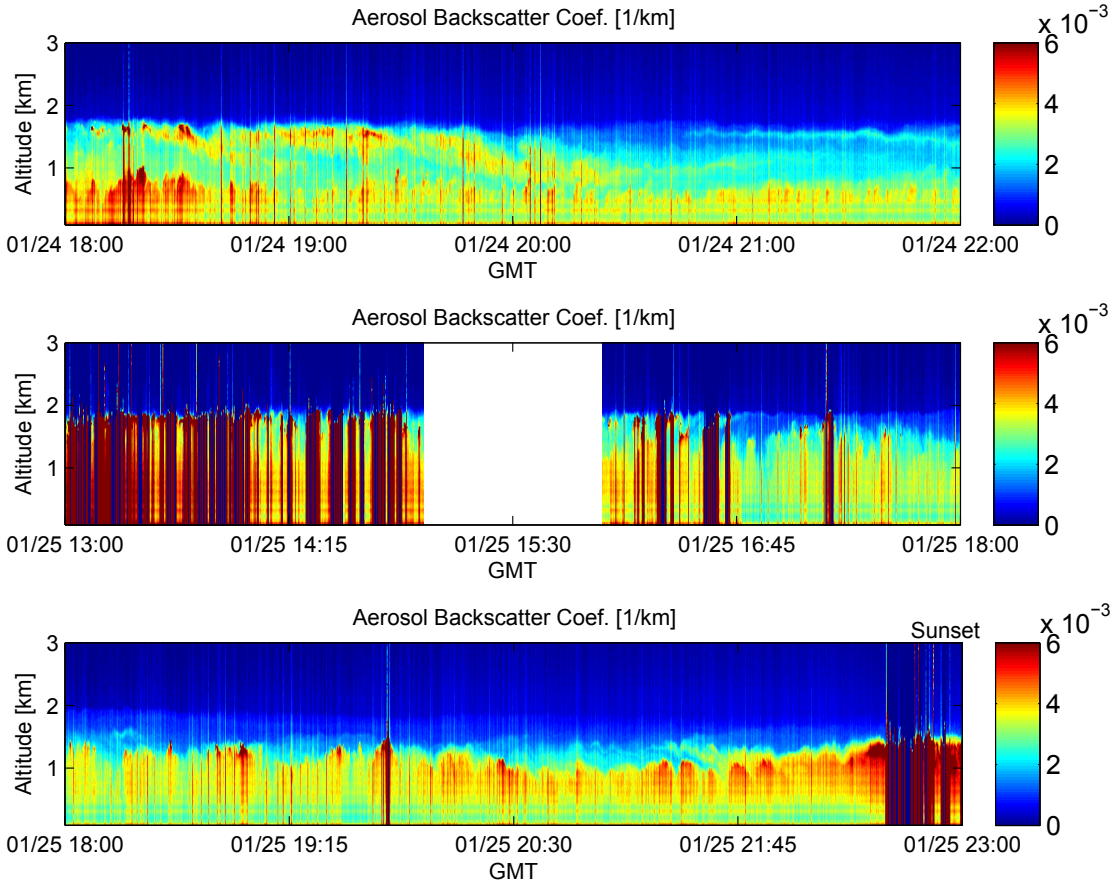

Figure 3.5: Aerosol backscatter coefficient using the Fernald inversion with AOD.

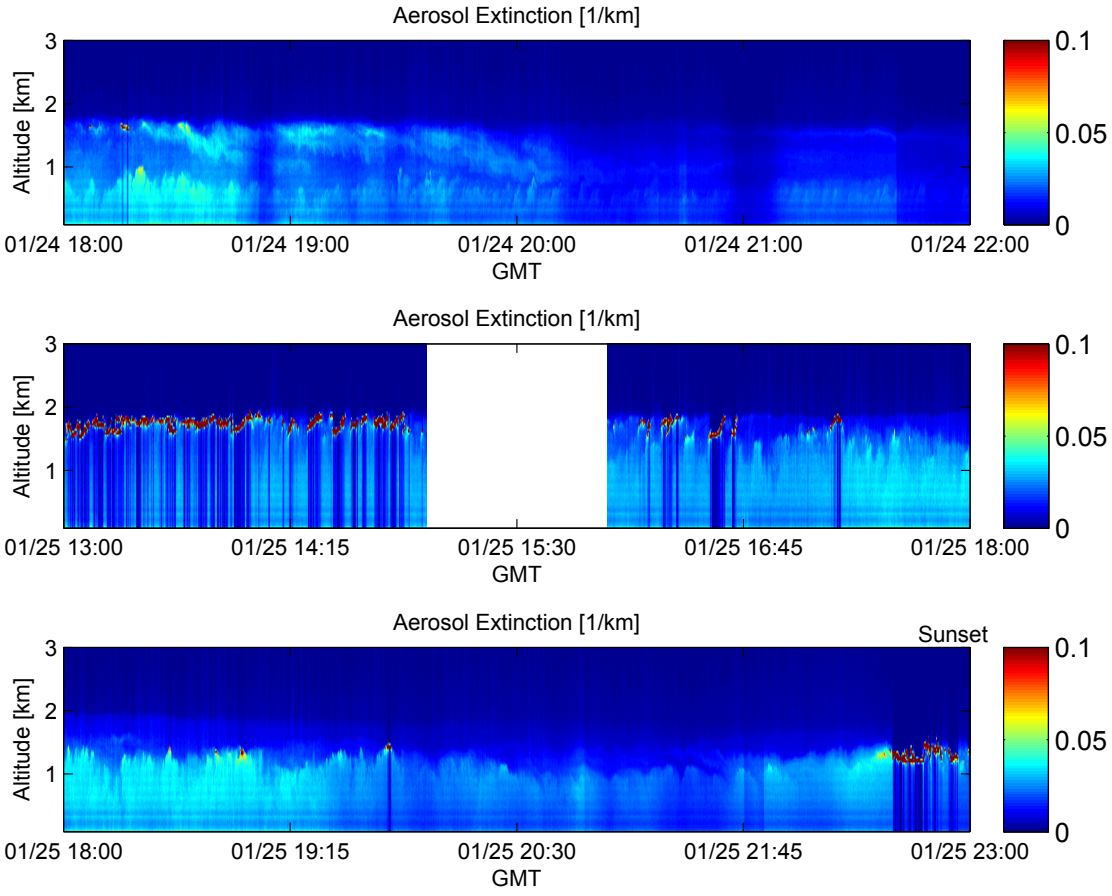

Figure 3.6: Aerosol extinction coefficient using the Fernald inversion with AOD.

By fitting a $C_{new}\text{RAY}(r)$ to NRB, we find a new calibration coefficient C_{new} that is related to the lidar constant C by:

$$C_{new} = Ce^{-2\tau_A}. \tag{3.6}$$

Then, we solve for AOD with:

$$AOD = \tau_A = \frac{1}{2}\ln\left(\frac{C}{C_{new}}\right). \tag{3.7}$$

An example extinction and backscatter profile from the Fernald inversion with C is shown in Fig. 3.7. For altitudes greater than 5 km, the Rayleigh portion of the extinction dominates, which can be seen when the Rayleigh extinction and the total extinction overlap in Fig. 3.7.

The benefit of this technique is that we no longer rely on the Aeronet aerosol optical depth data given at that specific moment in time. This does not mean that we do not need the Aeronet data, because it is what allows us to find the lidar constant C in the first place. The difference is that we can extend our measurements and use the lidar constant C to measure the aerosol optical depth at night as well, when no sun photometer data is possible, or other times when we do not have sunphotometer data.

Next, we show the aerosol basckscatter (Fig. 3.8) and extinction (Fig. 3.9) profiles inverted with C.

Now, there is the matter of whether the derived aerosol properties (i.e AOD, β_a, σ_a, and R_a) from the Fernald inversion with C corresponds well to the inversion with AOD. Let us start by comparing the Aeronet Cimel to the MPL (Fernald Inversion with C) aerosol optical depth. In Fig. 3.10a, we see that the MPL AOD is more varied than the Aeronet AOD. One reason for this is that the MPL has a time interval of 15 seconds between data points and each time sample represents a 15 second time average. Each Aeronet AOD time sample, however, is an average of

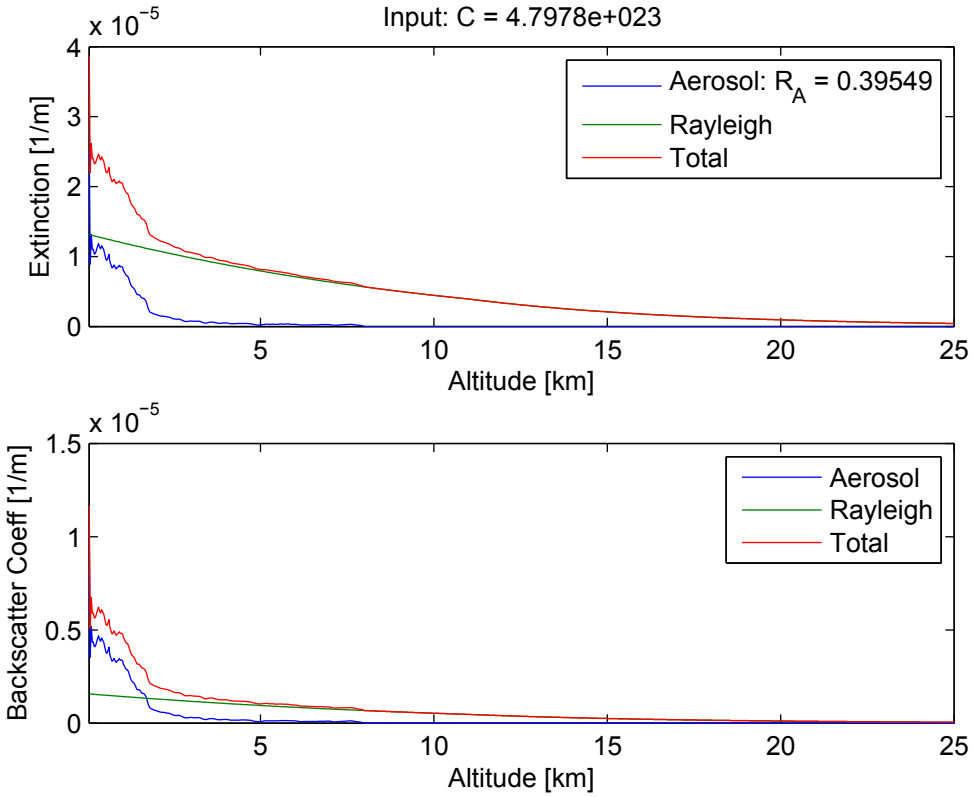

Figure 3.7: Extinction and backscatter profile generated with Fernald algorithm and the lidar constant C, 1/24/2013 20:41:57. Extinction if found by dividing the backscatter by R.

three measurements taken 30 seconds apart, or a 60 second average and 15 minutes between time samples [31]. Given the different time averages and time between data points, a more relevant comparison can be obtained by averaging the MPL AOD over 60 seconds and centered around times corresponding to the Aeronet times (Fig. 3.10b). The average MPL and Aeronet AOD has a strong correlation with a correlation coefficient of 0.93. However, the MPL AOD tends to be greater than the Aeronet AOD. The average difference between MPL and Aeronet AOD is 0.018 (Fig. 3.10c).

With the Fernald inversion with AOD, we interpolate the Aeronet AOD to match the time scale of the MPL data. The time gap of 15 minutes between the

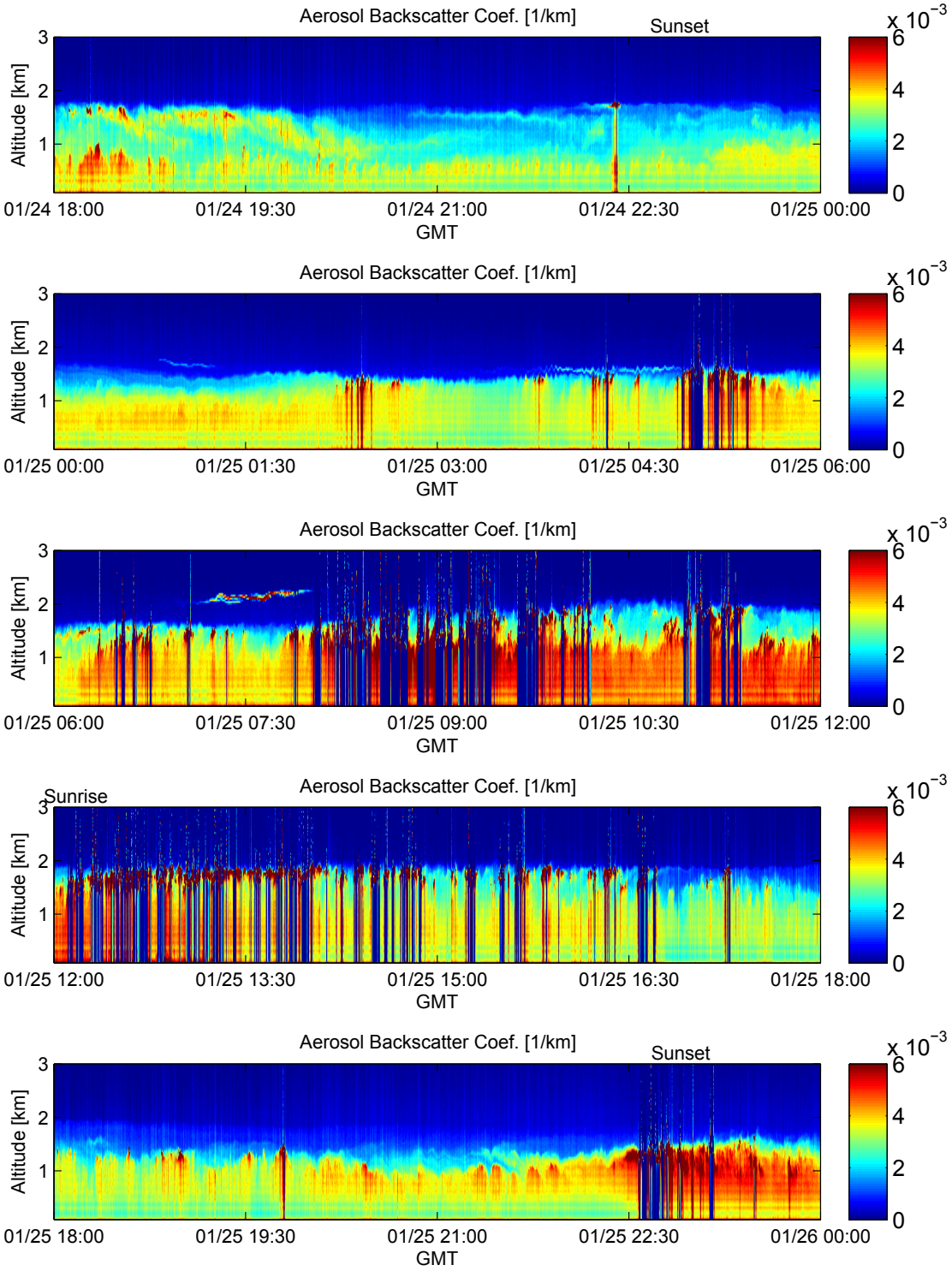

Figure 3.8: Aerosol backscatter coefficient using the Fernald inversion with C.

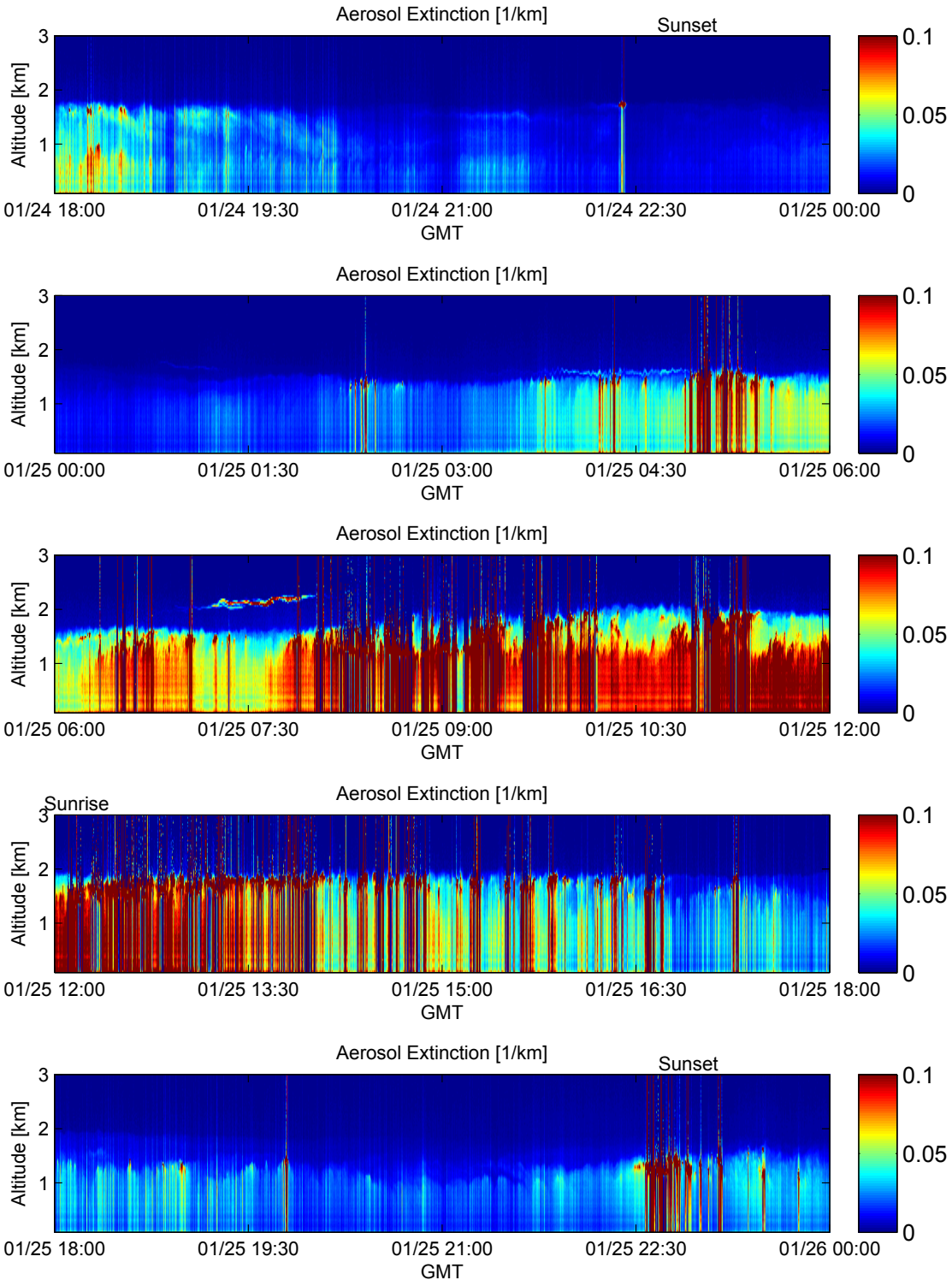

Figure 3.9: Aerosol extinction coefficient using the Fernald inversion with C.

Aeronet data can lead to incorrect interpolated AOD, as would extinction and backscatter, when the aerosols evolve on a time scale smaller than 15 minutes. For example, in Fig. 3.11a, the interpolated AOD does not resolve the two clouds peaks at 18:15 and 18:17, which can be seen on closer inspection of the NRB image starting at 18:15 (Fig. 3.11b. The inversion with C AOD starts at 0.20 at 18:00, which is followed by a sharp peak equal to 1.1 at 18:17, and then goes down to 0.18 by 18:30. The AOD inversion with C better depicts what we see in the NRB images (Fig. 3.11b). Consequently, there is not a good agreement between the Fernald inversion with AOD and C for 18:00 to 18:30. Conversely, aerosol optical properties for both inversions have good correlation when AOD is stable, as in 18:30 to 22:00, where the correlation coefficient between the inversions is 0.81 (Fig. 3.12a) for R_A and an average difference between R_A with C and R_A with AOD equal to -0.031 (Fig. 3.12b). The aerosol backscatter between the two methods also agree strongly with a correlation coefficient 0.99 and an average difference of 1.2×10^{-7} m^{-1} (Fig. 3.13). Similarly, the aerosol extinction has a correlation coefficient equal to 0.94 between the two inversions and an average difference of 2.4×10^{-6} m^{-1}.

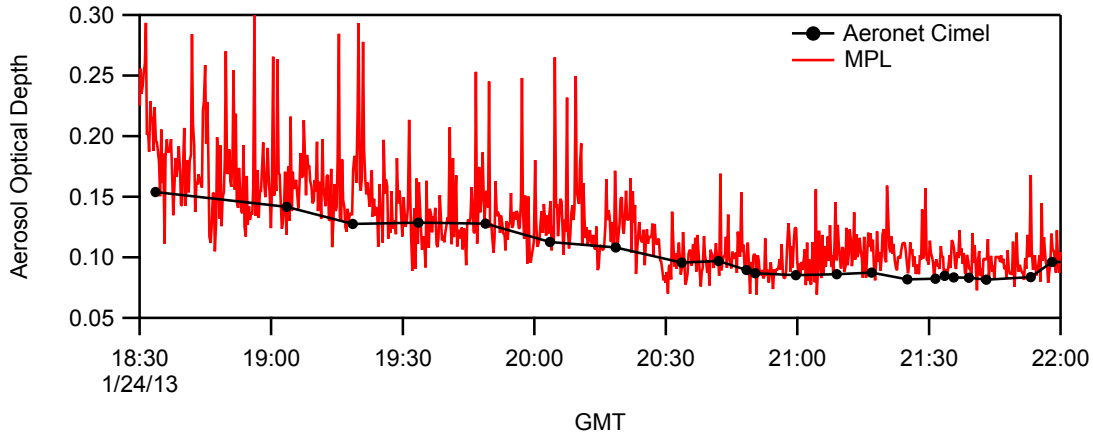

(a)

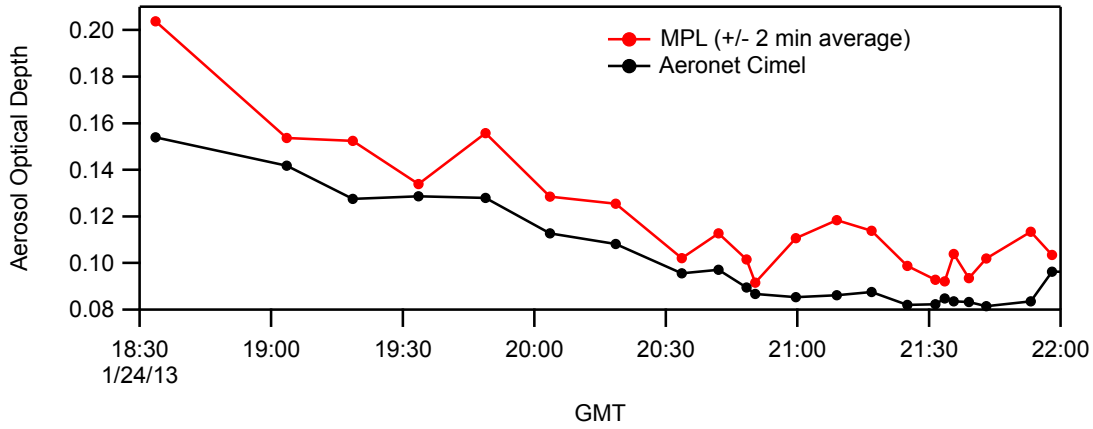

(b)

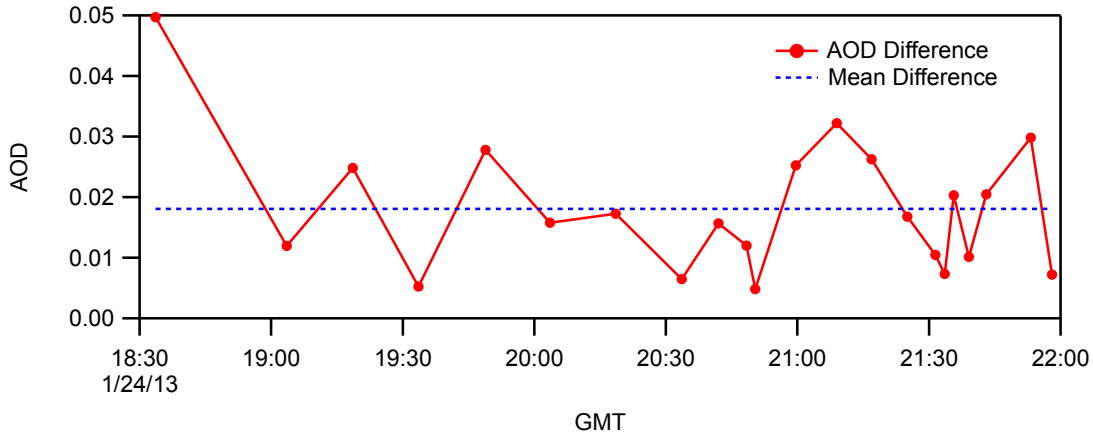

(c)

Figure 3.10: (a) MPL vs Aeronet Cimel #631 AOD, 1/24/2013. (b) 90 Sec average MPL vs Aeronet Cimel #631 AOD, 1/24/2013. Correlation Coefficient is 0.93 between Cimel and MPL AOD. (c) AOD Difference between averaged MPL and Aeronet AOD. The mean difference is 0.018.

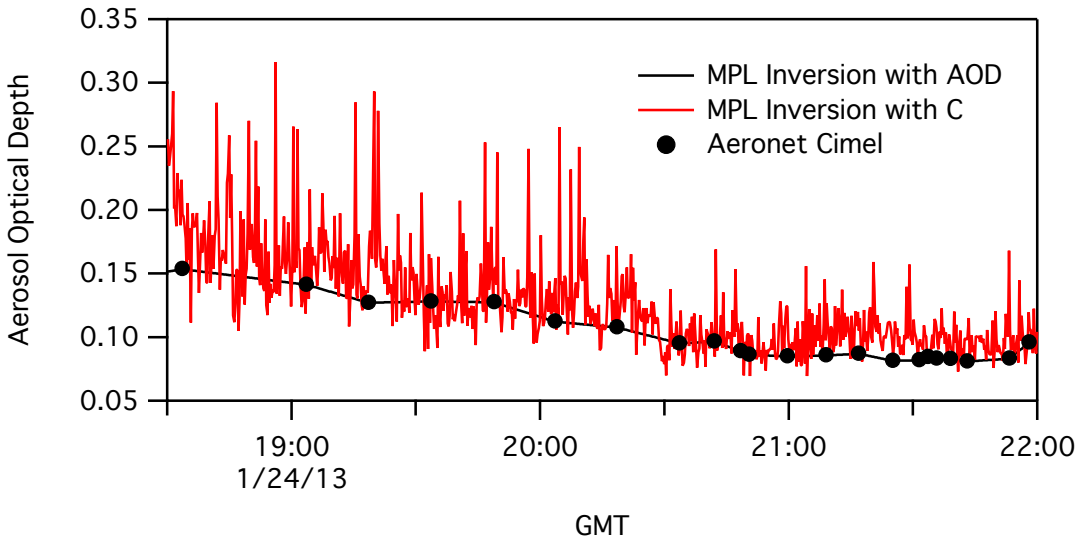

(a)

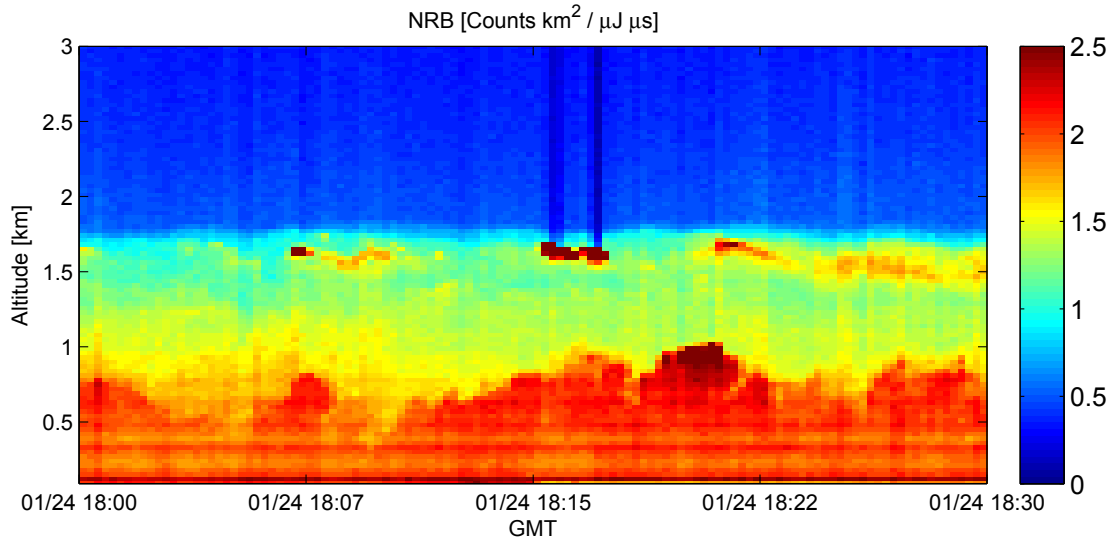

(b)

Figure 3.11: (a) AOD comparision: Fernald inversion with C and interpolated Aeronet AOD for 1/24/13 18:00 to 20:00. (b) Co-polarized NRB for 1/24/13 18:00 to 18:30. The two small clouds seen in the NRB image around 18:15 and 18:17 and around 1.5 km cause the two large AOD peaks (0.7 and 1.0) seen in the AOD time series.

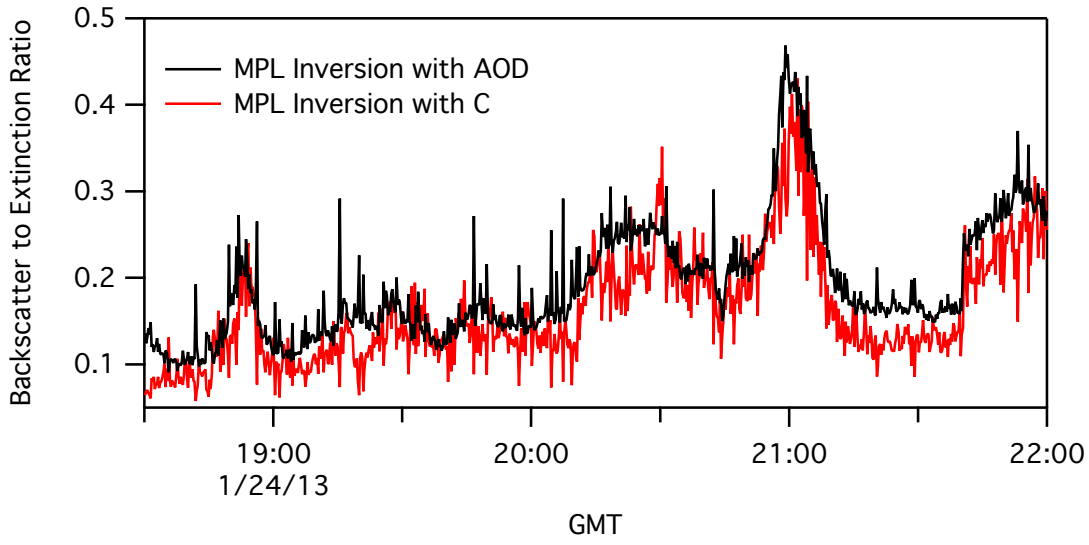

(a)

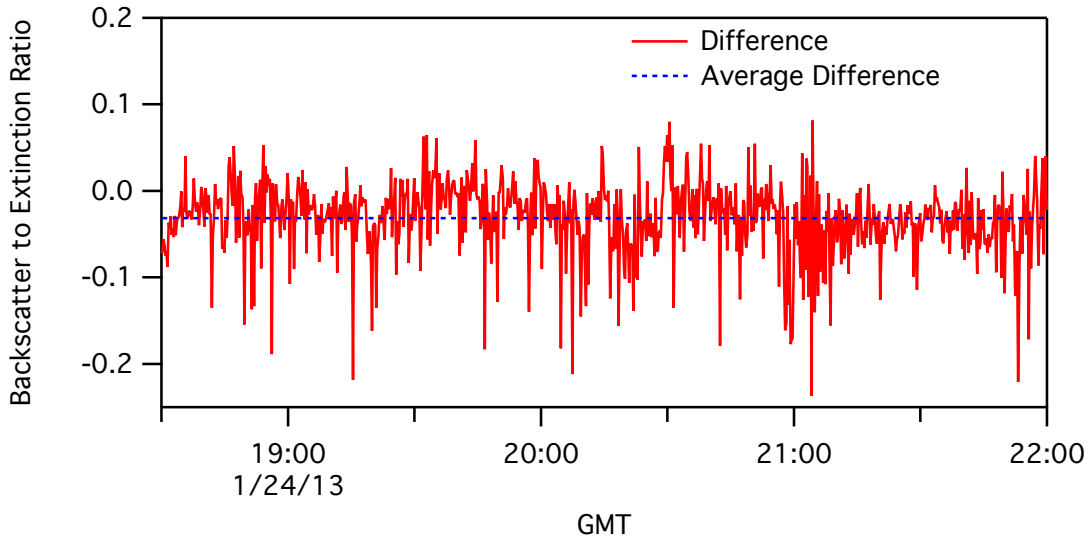

(b)

Figure 3.12: (a) Backscatter to extinction coefficient R_A comparison of Fernald inversions with C and AOD. (b) Difference between Fernald inversions with C and AOD. Average difference is -0.031.

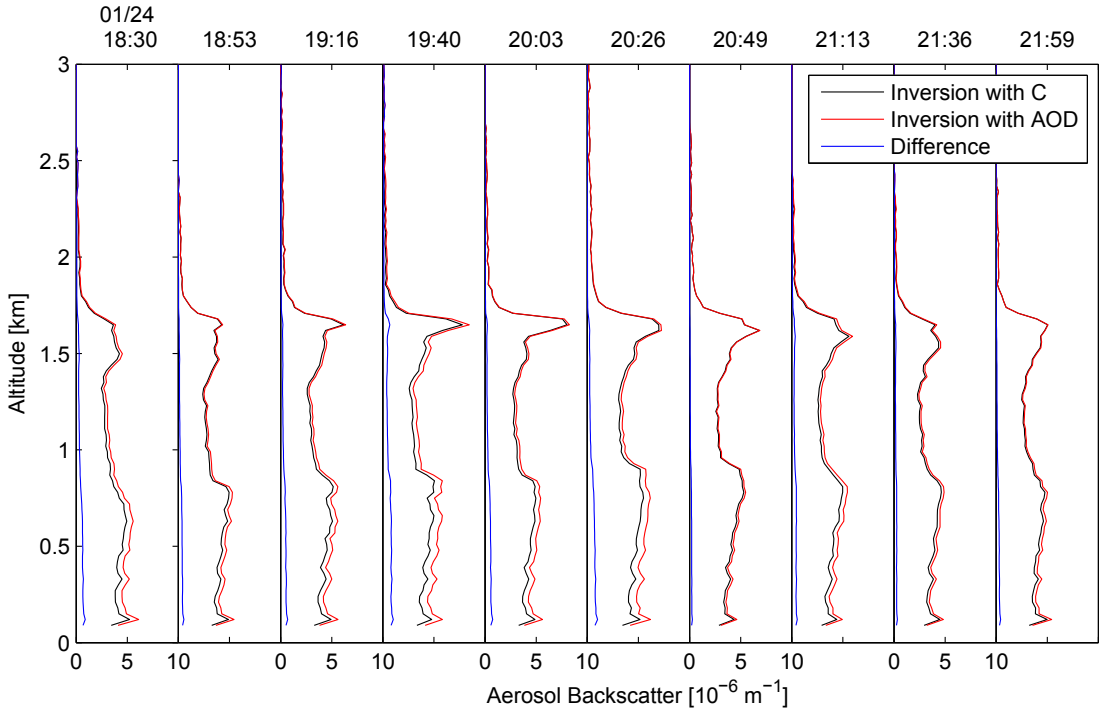

(a)

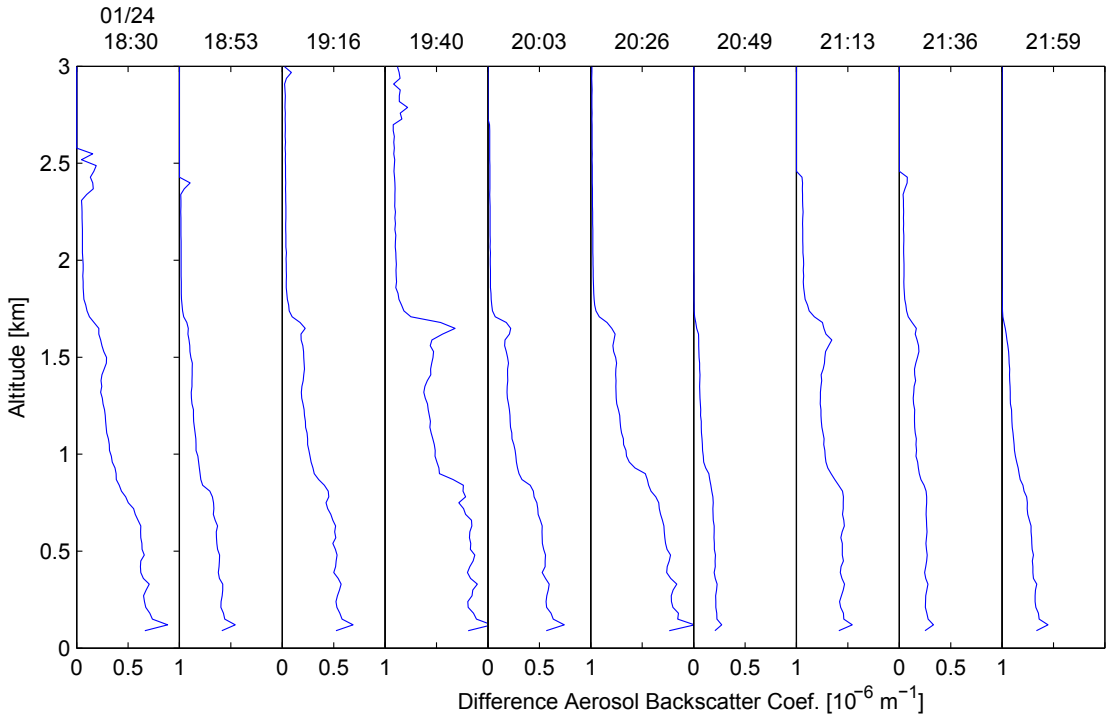

(b)

Figure 3.13: (a) Aerosol backscatter profile comparison between inversions. (b) The average absolute difference between the inversions is 1.2×10^{-7} m^{-1}.

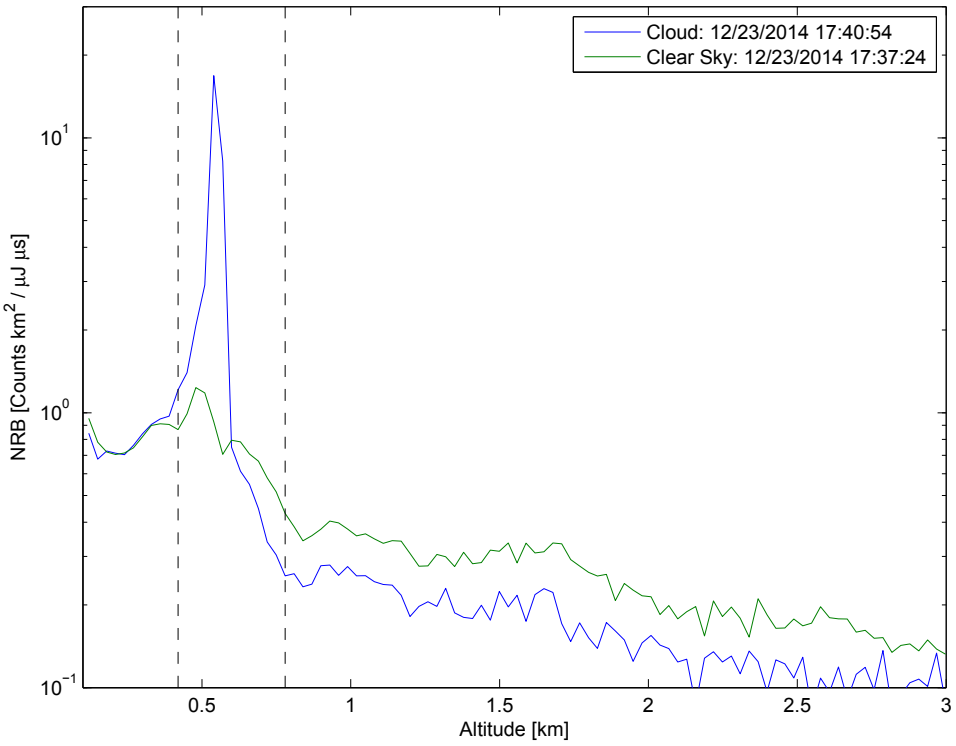

Figure 3.14: NRB profile comparison between cloud and clear sky. The dashed lines correspond to the limits of the clouds layer (0.42 to 0.78 km). The decrease in NRB from the beginning of the cloud layer to the end is used to find cloud optical depth (0.20). The cloud case had a total AOD equal to 0.27.

3.3 Cloud Optical Depth from MPL data

Cloud optical depth is a portion of the total AOD is found from Eq. 3.7. In order to retrieve the optical depth portion pertaining to a cloud, we use the change in NRB(r) across the cloud from lower altitude limit (r_-) and the upper altitude limit (r_+) along with the aerosol backscatter profile found from the Fernald algorithm (Fig. 3.14). The NRB at the bottom of the cloud is:

$$\mathrm{NRB}\,(r_-) = C\,[\beta_A(r_-) + \beta_R(r_-)]\,e^{-2[\tau_A(r_-)+\tau_R(r_-)]}, \tag{3.8}$$

where $\tau_A(r_-) + \tau_R(r_-)$ is integrated total extinction up to altitude r_+. Similarly, the NRB at top of the cloud is:

$$\mathrm{NRB}\,(r_+) = C\,[\beta_A(r_+) + \beta_R(r_+)]\,e^{-2[\tau_A(r_+)+\tau_R(r_+)]}. \tag{3.9}$$

Dividing Eq. 3.8 by Eq. 3.9, and solving for $\tau_A(r_+) - \tau_A(r_-)$ we find the cloud optical depth:

$$\Delta\tau_{cloud} = -\Delta\tau_R - \frac{1}{2}\ln\left(\frac{\mathrm{NRB}(r_+)\,[\beta_A(r_-) + \beta_R(r_-)]}{\mathrm{NRB}(r_-)\,[\beta_A(r_+) + \beta_R(r_+)]}\right), \tag{3.10}$$

where $\Delta\tau_{cloud} = \tau_A(r_+) - \tau_A(r_-)$ is the cloud optical depth and $\Delta\tau_R = \tau_R(r_+) - \tau_R(r_-)$. For example, in Fig. 3.14, $r_+ = 0.78$ km and $r_- = 0.27$ km and we found a cloud optical depth equal to 0.20. A time series of cloud optical depth found from MPL data (12/23/14 17:00 to 18:00 GMT) is shown in Fig. 3.15. In later chapters we will compare this cloud optical depth to data found from our zenith radiance detector. Given the agreement between the inversion with C and AOD, and the power of the MPL laser, we expect the MPL cloud optical depth to be a good measurement for optically thin clouds. For optically thick clouds, the MPL signal becomes attenuated beyond the cloud layer. This leads to bad Rayleigh fits (Eq. 3.6) and consequently bad inversions of cloud optical depth (Eq. 3.10).

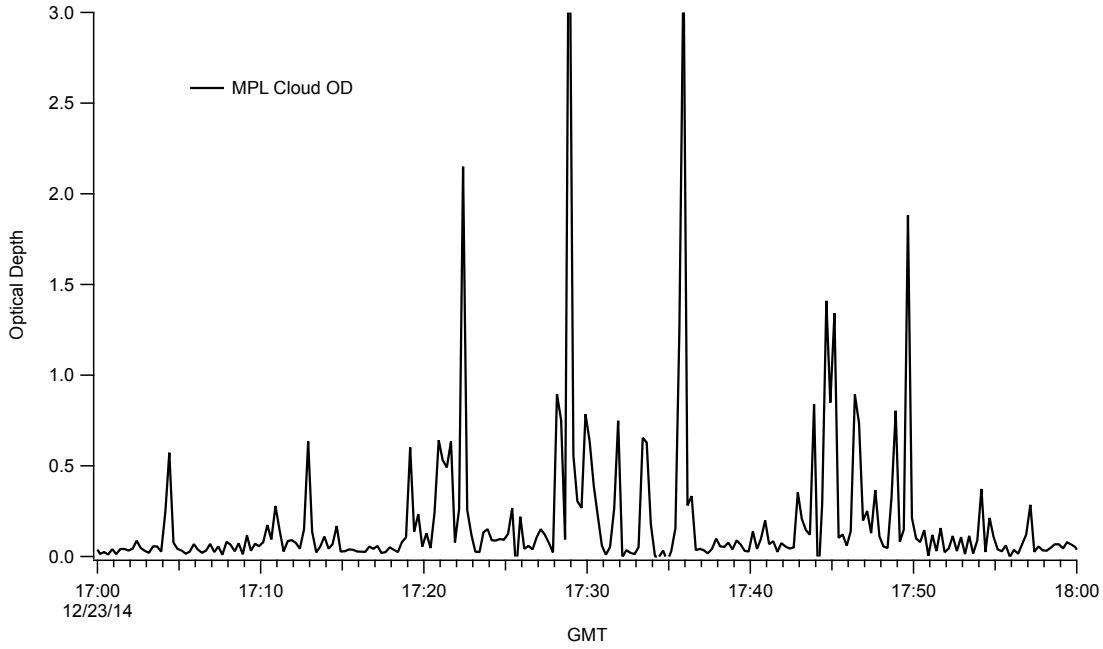

Figure 3.15: Cloud optical depth time series.

Chapter 4

Spectral Albedo Measurements

The surrounding surface albedo is one of the biggest inputs into the cloud optical depth model; and our Key Biscayne measurement site is very different from the site used in Marshak et al. [1] whose method is discussed in detail in a later chapter. In Marshak et al. [1], the measurements were located at the ARM Oklahoma site, see Fig. 4.1a. The albedo was bright in the near infrared and dark in the red. The contrast in the albedo at these wavelengths allowed the authors to use this technique to measure the cloud optical depth. We want to apply this method to our site at RSMAS (Key Biscayne, FL). If you take a look at the surface surrounding our site, as shown in Fig. 4.1b, three main surface types stand out: water, vegetation, and general city type surfaces. The question is how much of an impact does the surrounding water have on the effective surface albedo. Will we be able to find wavelengths with sufficient contrast? With this in mind, I took measurements of several sites around RSMAS to classify the surface types and create an albedo map. With the map, I can estimate the effective albedo for the site.

4.1 Effective Radius for Surface Albedo

The first main concern is how to weight the various surfaces at different distances from the measurement site. Associated with this is at what distance do surface albedo properties no longer have an effect on the data or model. In order to get a handle on this, we considered light coming in, E_0, at zenith angle, θ_0, and then

(a) ARM(Atmospheric Radiation Measurement) Program Site: Lamont, OK [42].

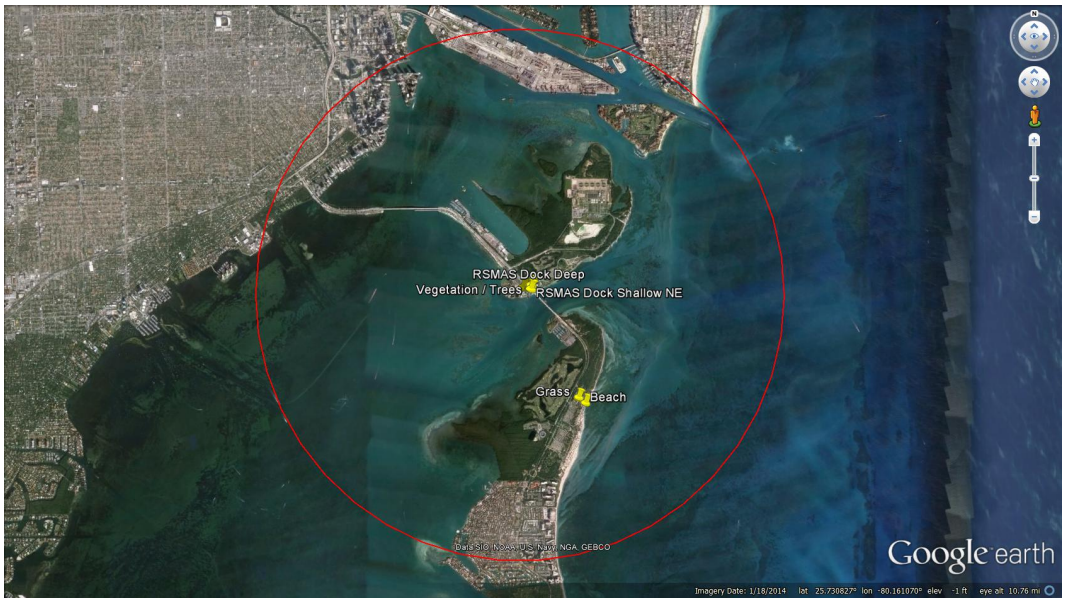

(b) RSMAS: Key Biscayne, FL [43].

Figure 4.1: Satellite Images of ARM and RSMAS sites.

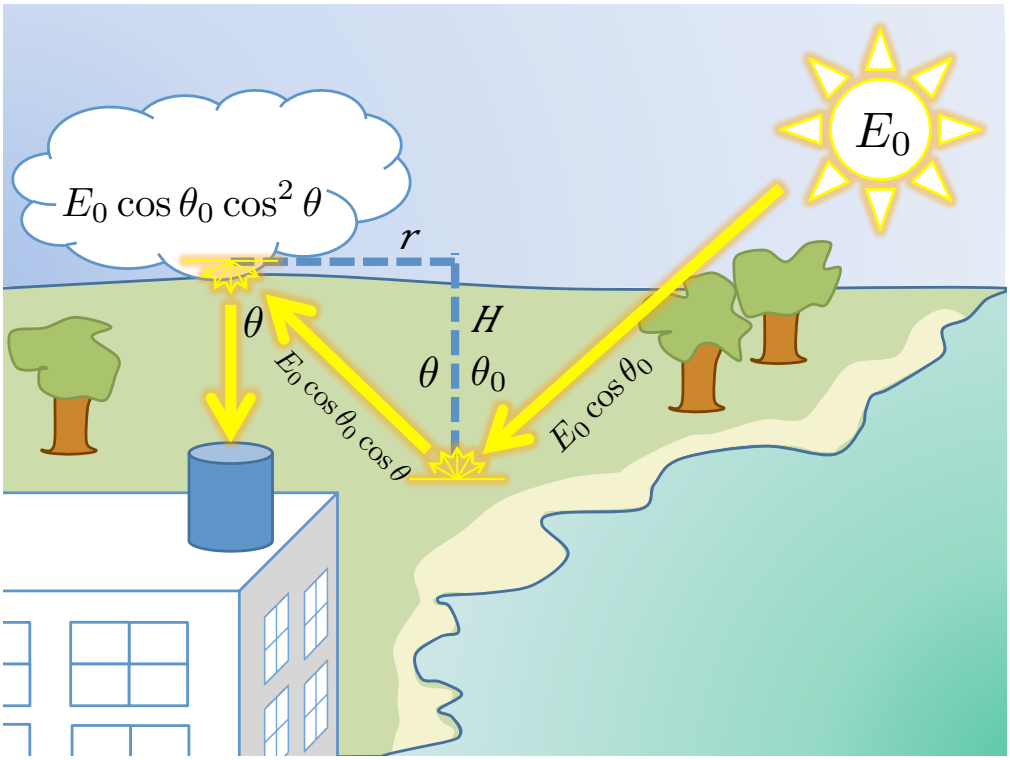

Figure 4.2: Scenario considered in finding the effective radius for surface albedo. The light comes from the sun with irradiance, E_0 reflects from the surface and then reflects again from the cloud.

reflecting off the surface with an albedo ρ. Call this E_1. This light then reflects off a cloud located at a height, H (see Fig. 4.2 for the scenario being considered). Assuming Lambertian reflection for each interaction, and using Lambert's Cosine Law, we find that each reflection picks up a $\cos\theta$. The light coming to the radiometer would then be $E_2 = E_0 \cos\theta_0 \cos^2\theta$. Applying the geometry of the problem ($\tan\theta = r/H$) we get:

$$E_2 = E_0 \cos\theta_0 \frac{H^2}{H^2 + r^2}. \tag{4.1}$$

This puts the problem in terms of the radius, r, which allows us to estimate how distance affects the light making it to the measurement site. After simplification we find:

$$E_2 = E_0 \cos\theta_0 \frac{1}{1 + (r/H)^2}. \tag{4.2}$$

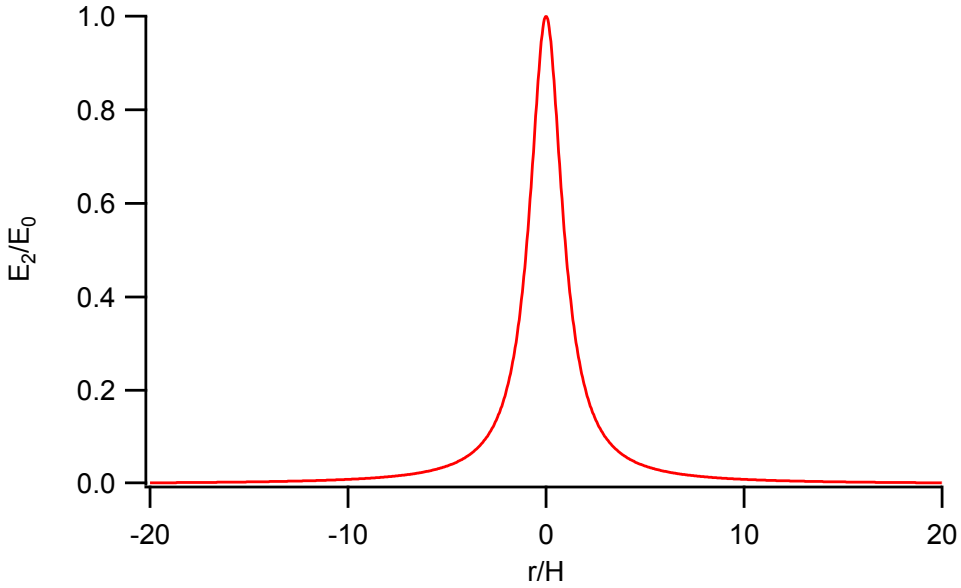

Figure 4.3: Incoming irradiance contribution as a function of ratio between the radius and cloud height, r/H.

We can now see that points far away from the radiometer contribute very little (Fig. 4.3). For example, a distance r equal to the cloud height will have an effective weighting of 0.5. The weight of the surface at 5 times the cloud height is 0.04 given a typical cloud base height of 1 km. I considered surfaces up to 5 km from our site.

4.2 Spectral Albedo for Different Surface Types

Using a Google Earth satellite image of the measurement site at RSMAS, and establishing a 5 kilometer radius around the latitude and longitude of the radiometer's location, I identified 7 surface categories: Shallow Water, Buildings, Vegetation, Grass, Beach, Asphalt, and Baseball Field. By creating an overlay on the still image, I created a surface albedo category map. For every surface identified, the map was overlapped by the color representing that category of surface. Once the albedo for each category of surface was determined, the map can be populated with the surface albedo measured for that category. Figure 4.4 is the

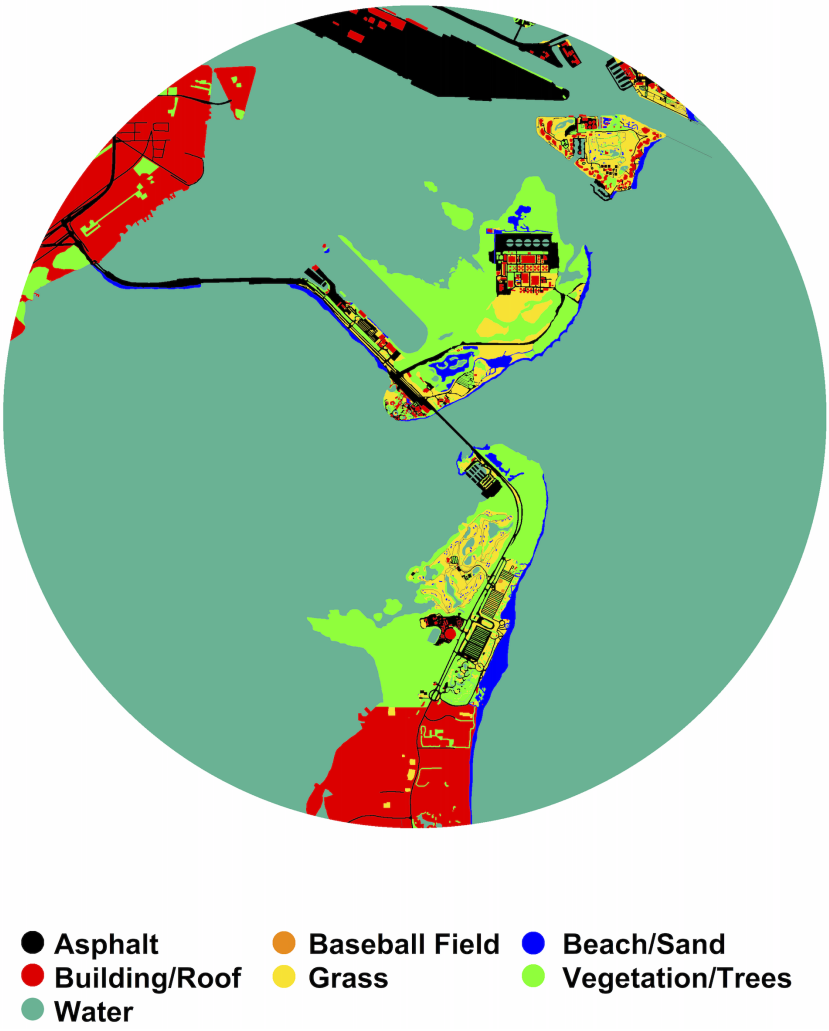

Figure 4.4: Surface Albedo Category Map of RSMAS: Surface categories identified for effective surface albedo of RSMAS centered at 25.73197 N, 80.16333 W in degrees.

category map. The advantage of this mask technique is that it is easy to update the map if better or alternative albedo values are found.

Once the surface types were identified, I went out and measured the albedo for each type. To measure the albedo, I used an Ocean Optics spectrometer (USB4000) connected to an optical fiber with a cosine irradiance collector on the fiber input. The procedure was as simple as taking one measurement with the irradiance collector pointing up and another measurement pointing down. Albedo is simply the

ratio of the up and downward irradiance. With the collector facing up, one measures the total downwelling irradiance, $E_{\downarrow}(\lambda)$. Whereas in the down measurement, one measures the upwelling or reflected irradiance, $E_{\uparrow}(\lambda)$, from the surface. The albedo is the ratio of these measurements:

$$\alpha(\lambda) = \frac{E_{\uparrow}(\lambda)}{E_{\downarrow}(\lambda)}. \tag{4.3}$$

Once we integrate and weight the individual albedo values, the integral albedo is used in the radiance cloud models, discussed in a later chapter, to estimate the zenith radiance as a function of cloud optical depth.

Most albedo measurements sites were located close to RSMAS to match the conditions actually seen in our map. However, the asphalt type was measured in the parking lot behind the University of Miami's Physics Building in Coral Gables. To estimate the albedo of water, I took three measurements at the RSMAS Dock. For the current model, I used the deep end dock data since most of the water in the map is deep. However, in the future it may be interesting to separate the water parts of the map into additional water environments, such as shoal, sea grass, and deep water. The measurements were taken during clear and sunny days. Screen captures of Google Maps indicating the GPS location and photos at the measurement location were recorded concurrently with the albedo measurements (Fig. 4.5).

The results of the albedo measurements are summarized in Fig. 4.6. For example we can see the typical behavior that we expect for plants in the grass and vegetation/trees spectra. There is little reflection, or high absorption, in the visible part of the spectrum, from about 400 to 700 nm, and it is highly reflective in the near infrared, or greater than 750 nm. If all of the surface near our measurement site matched this signature, then we could proceed with Marshak et al.'s [1]'s procedure directly. However, our case is not that simple. The spectral albedo of

(a) Asphalt
25.723570° N, 80.279780° W

(b) Baseball Field
25.713058° N, 80.152828° W

(c) Beach/Sand
25.712391° N, 80.151488° W

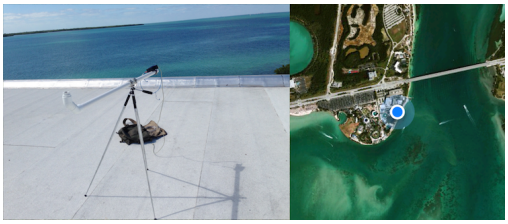

(d) Building/Roof
25.731796° N,80.163419° W

(e) Grass
25.713333° N, 80.152778° W

(f) Vegetation/Trees
25.732227° N, 80.161841° W

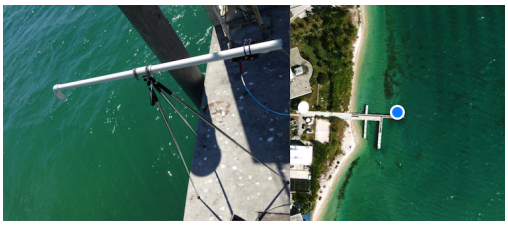

(g) Water: RSMAS Dock Deep End
25.731547° N, 80.161936° W

(h) Water: RSMAS Dock Shallow NE
25.731669° N, 80.161905° W

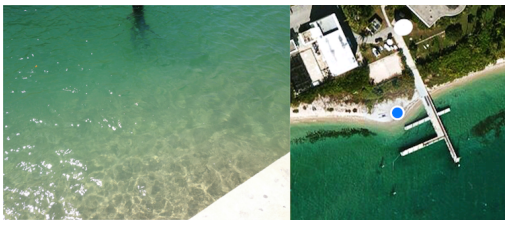

(i) Water: RSMAS Dock Shallow SW
25.731571° N, 80.162154° W

Figure 4.5: Albedo Measurement Sites. Satellite images are taken from screen captures of smart phone's Google Maps App at the location of the measurements.

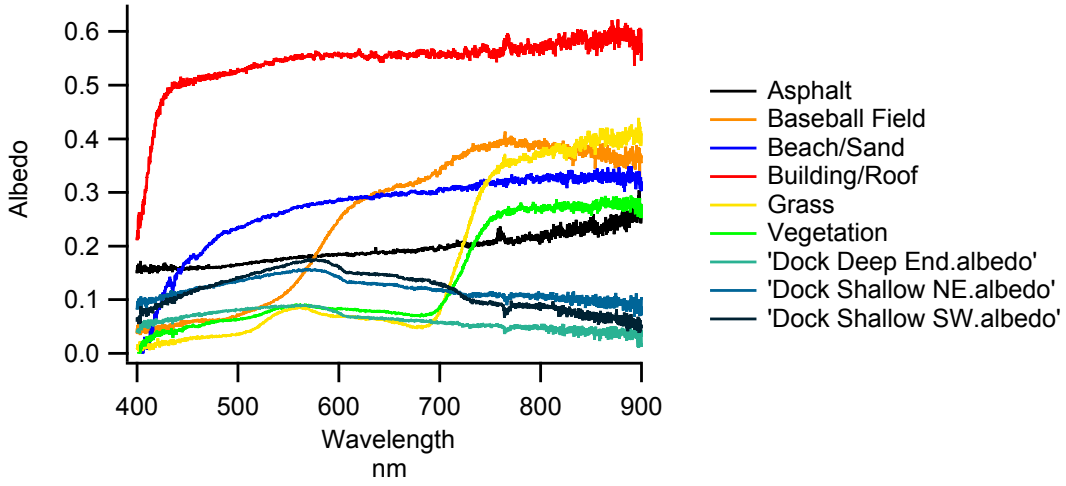

Figure 4.6: Albedo for different surface types corresponding to the locations in Fig. 4.5

Asphalt, Building/Roof, and Water surfaces are relatively flat compared to the plant surfaces. Baseball fields, interestingly, turn out to not be that flat, which makes sense considering their red color, but are highly reflective in the red region of the spectrum, around 620 to 700 nm.

The question then is can we find a wavelength pair in the integral spectral albedo with sufficient contrast to apply the technique of Marshak et al. [1]?

4.3 RSMAS Albedo Maps

With the albedo measurements we can fill in the albedo map (Fig. 4.7). To do this, we use the scenario described in Fig. 4.2. Figure 4.7 shows the albedo for each wavelength in our radiometer. They have been uniformly scaled from zero to one in order to intercompare the map for these wavelengths. There is a lot of water in the scene and, as shown in Fig. 4.6, the water's albedo varies little compared to the rest of the surfaces. Much of the land is bright in the near infrared, 860 nm, but dark in the red, 670 nm. The Key Biscayne area is vegetated in general with a couple of big parks and a golf course in the area. Starting 3 km from the center we start to

see buildings which are significantly brighter in all the wavelengths except 410 nm, although it is still brighter than the other surfaces at that wavelength. However, the majority of the buildings are far away from the center so their contribution to the integrated albedo may not be significant.

Not all surfaces surrounding the radiometer will have the same impact. To determine the effective albedo, I found the average albedo weighted by distance as in Eq. 4.2. For clarity let us rename this function as the weighting function:

$$E_{weight}(r,\theta) = \frac{E_0(r,\theta)}{1+(r/H)^2}. \tag{4.4}$$

The average albedo per wavelength can be expressed as a polar integral as:

$$\overline{\alpha_\lambda} = \frac{\int_0^{r_f}\int_0^{2\pi} E_{weight}(r,\theta)A_\lambda(r,\theta)rdrd\theta}{\int_0^{r_f}\int_0^{2\pi} E_{weight}(r,\theta)rdrd\theta} \tag{4.5}$$

where E_0 is the source incoming irradiance, H is the cloud height, $A_\lambda(r,\theta)$ is the albedo map data as in Fig. 4.7, and r_f is the effective distance from our measurement point. As stated earlier, we consider up to 5 kilometers from the measurement site. I performed this procedure for all of the radiometer wavelengths.

We will be working under conditions of variable clouds - hence variable and uneven surface illumination. Thus, we wanted to be able to attach statistics to our albedo calculation. With this in mind, we added random Gaussian noise to the light source E_0 of the form:

$$E_0(r,\theta) = 1 + gnoise(\sigma) \tag{4.6}$$

where gnoise is a function that picks a number at random that obeys Gaussian statics with a standard deviation of σ. Dutton et al [44] indicated that surface illumination under cloudy conditions can vary with a σ of about twenty percent. Using this as our assumption,we factored in a light source that has a standard deviation of 0.2, or:

$$E_0(r,\theta) = 1 + gnoise(0.2). \tag{4.7}$$

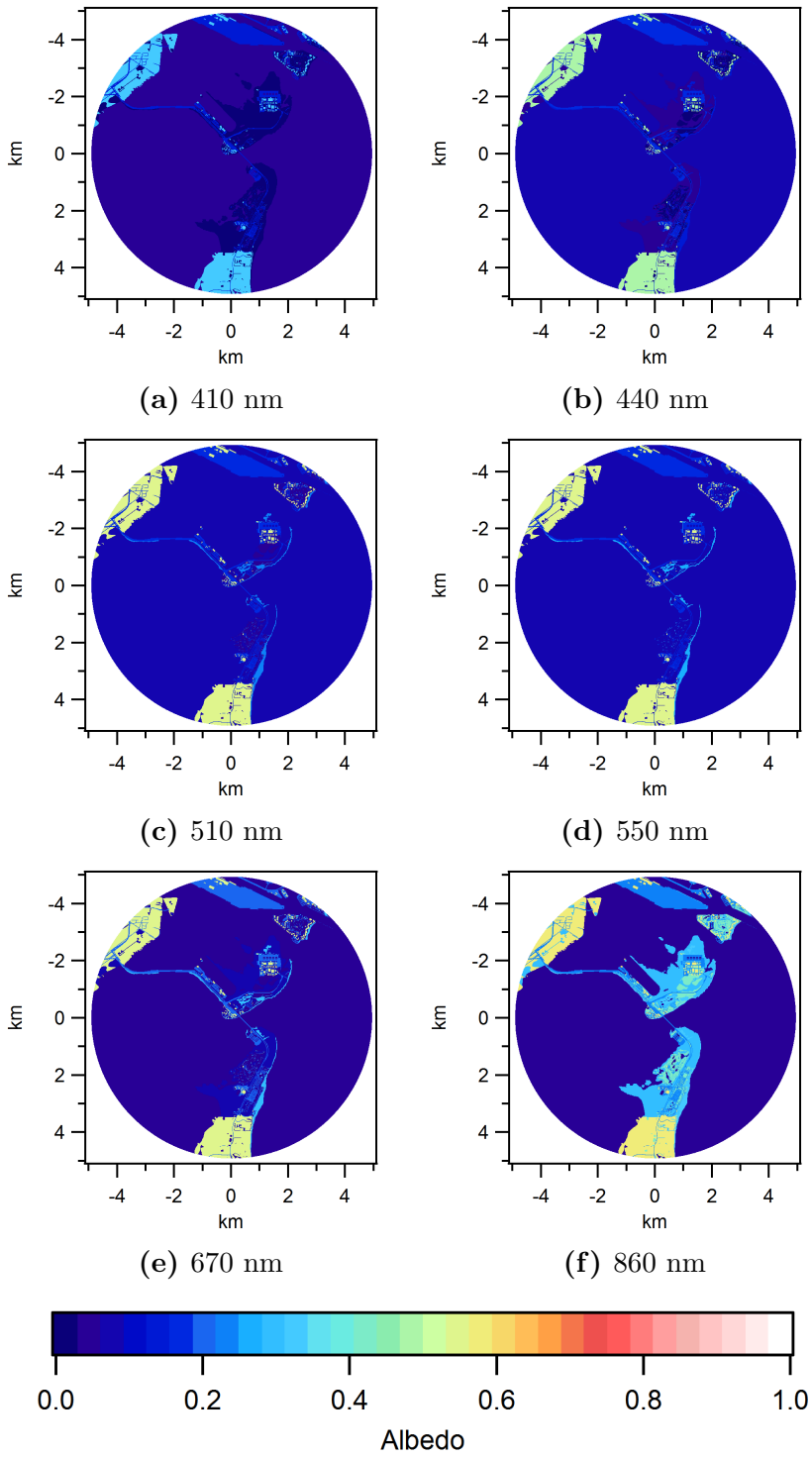

(a) 410 nm **(b)** 440 nm

(c) 510 nm **(d)** 550 nm

(e) 670 nm **(f)** 860 nm

Figure 4.7: Albedo Maps for different wavelengths, within a 5 km radius around the measurement site.

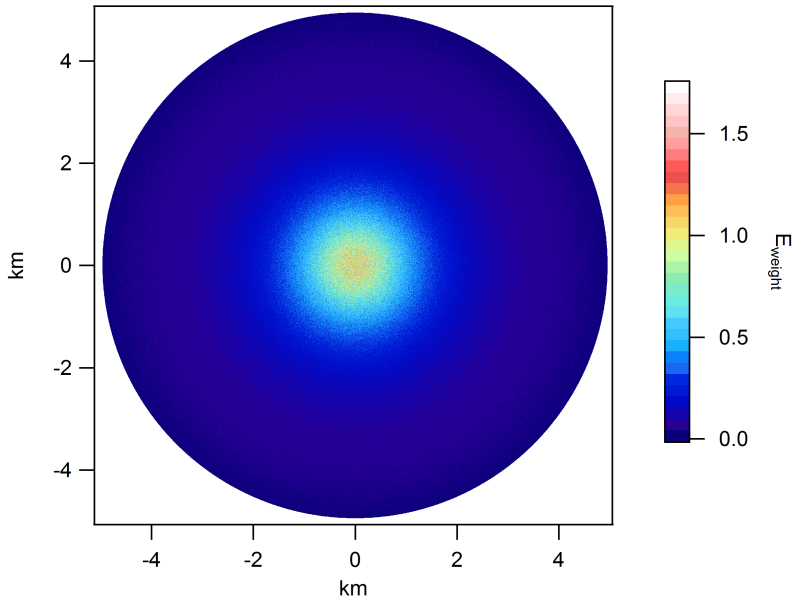

Figure 4.8: Typical random light source E_{weight} used for effective albedo calculation.

We calculated the albedo for a given wavelength using Eq. 4.5, with a random light source of the form of Eq. 4.7, one thousand times and calculated the average and standard deviation of these calculations. The results are summarized in Table 4.1.

Table 4.1: Average albedo with Monte Carlo performed.

Wavelength (nm)	Albedo Average	Albedo Standard Deviation
410	0.057979	6.28E-06
440	0.079622	9.62E-06
510	0.101101	1.06E-05
550	0.109588	1.05E-05
670	0.090216	1.25E-05
860	0.112089	2.00E-05

Given the hyperspectral resolution of the radiance spectrometer, we developed a more detailed picture of what is really going on. We calculated the albedo for a range of wavelengths ranging from 400 to 900 nm matching the spectrometer's

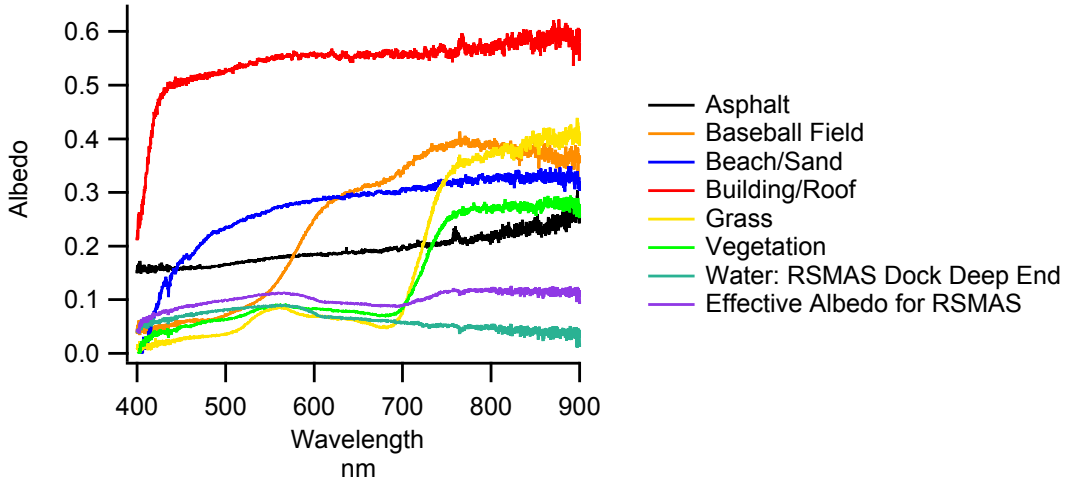

Figure 4.9: RSMAS Effective Albedo Spectrum in addition to spectrum for the surface types.

capabilities. For the sake of time and considering how small the standard deviation was found to be for the radiometer channels, we ran each wavelength once. What emerges is a spectrum that can be compared with the spectra of the different surface types (see Fig. 4.9). We can now start to answer the question of whether our site has sufficient contrast. RSMAS's effective albedo trends similar to water below 700 nm, but has a slightly higher albedo because of the other surfaces. Above 700 nm, the RSMAS albedo stops behaving like water, but instead trends up and then flattens out. The weighted percent contribution of each surface type is shown in Table 4.2. The top contributor is shallow water (74.18 %) and followed by vegetation/trees (10.92 %) and grass (4.33 %). Consequently, plant related surfaces add up to 15.25 % of the surface albedo contributions, making the land portion of the surface largely vegetated. Unfortunately, with the large contribution from water, there is still very little contrast in albedo, overall, between the different wavelengths.

Table 4.2: Weighted percent contribution to albedo by surface type.

Surface Type	Percent
Asphalt	5.34
Baseball Field	0.01
Beach	2.09
Buildings	3.14
Grass	4.33
Shallow Water	74.18
Vegetation	10.92

4.4 Comparison to MODIS Albedo

A possible option is to compare our albedo data with what is available from the MODIS satellite program. There is a filled albedo map available online that is an aggregate from the years 2000 to 2004 [45].

A concern with using this data is that it is ten years old and possible seasonal variation in the albedo. However, if you look at the seasonal variation of the MODIS albedo data, it seems like there is very little seasonal change, as seen in Fig. 4.10, reflecting our subtropical location. The one big change in the area surrounding our measurement site has been the white roof initiative at RSMAS and some new buildings on campus during this time. Other than campus, it is not likely that the parks have undergone many changes. Unfortunately, the MODIS product is only meant to be for the land thus does not give us much information on the water surface. My guess is that the ocean/shore albedo could be a source of large albedo variations, even on a seasonal scale.

There are two other issues, first the MODIS product is meant to be a land product, with a 1-minute resolution or a spatial resolution of 2 km near the equator [45], and our site has a lot of "mixed" pixels. The other issue is that the MODIS albedo wavelengths do not exactly correspond to ours. We can, however, interpolate the albedo for our wavelengths from the MODIS wavelengths. The in-

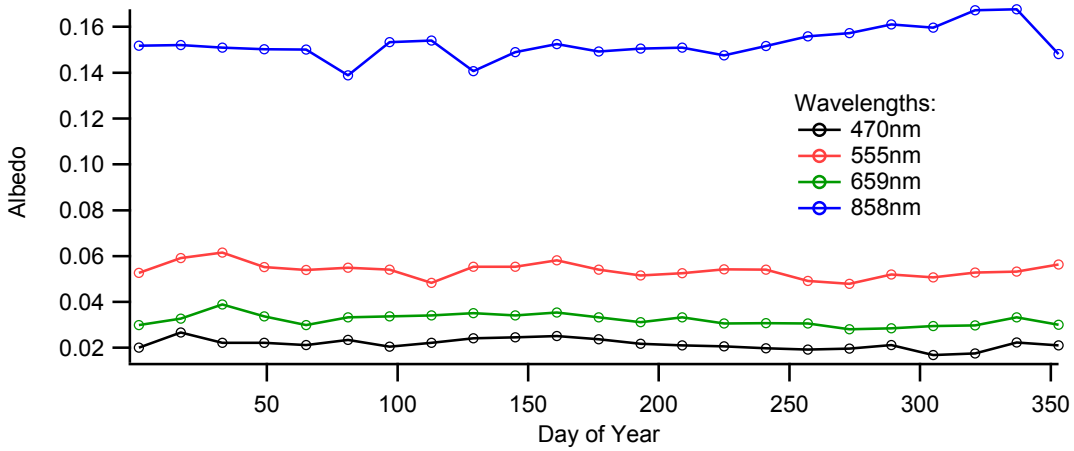

Figure 4.10: Seasonal MODIS Albedo for RSMAS site. The land surface albedo appears to be stable for this location

terpolation results are summarized in Table 4.3. We can also see how the MODIS albedo compares to our albedo measurements of surface types around RSMAS in Fig. 4.11. The MODIS albedo values seem to be a little lower than our Effective Albedo for RSMAS as it is labeled in Fig. 4.11, and the MODIS albedo has more contrast. It also corresponds closely to both the Grass and Vegetation albedo curves for the wavelengths below 700 nm. The 858 nm MODIS albedo seems to align more toward the effective albedo for RSMAS. It makes sense that the MODIS albedo agrees well with the vegetated surfaces given that it is a land product, and the presence of water in the effective albedo for RSMAS could account for the difference. However, which of these is the more accurate depiction of the albedo needed for the cloud model cannot truly be known without an independent third measurement from a high altitude. For example, some sky based measurement of the surface albedo may provide more pertinent information, and without the need of average surface types as we need to calculate the effective albedo for the RSMAS experiment. One could use a pair of calibrated irradiance spectrometers,

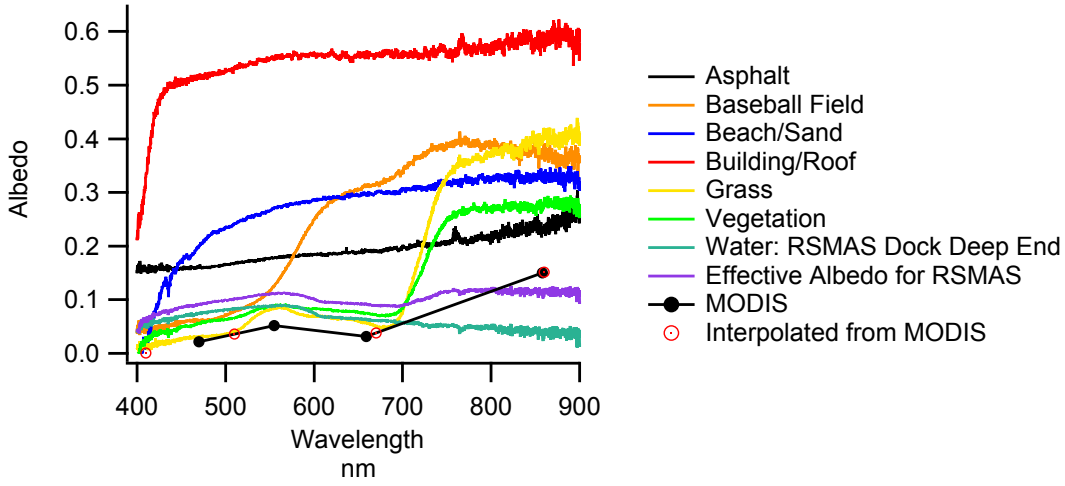

Figure 4.11: MODIS Albedo compared to RSMAS Albedo Map

Table 4.3: MODIS Surface Albedo for a day of year of 191

Wavelength (nm)	MODIS Albedo	Interpolation Wavelength (nm)	Interpolated Albedo
470	0.0219494	410	0.000809537
555	0.0518975	510	0.0360426
659	0.0313714	670	0.0379459
858	0.15031	860	0.151506

like the ones used in this experiment, to measure downwelling and upwelling irradiance simultaneously to retrieve surface albedo. Perhaps, this could lead to further research in the future.

Chapter 5

Cloud Optical Depth from Zenith Radiance

Marshak et al. [1] developed a method to determine the cloud optical depth using measurements of the spectral zenith radiance at red and near infrared wavelengths in a vegetated environment. The contrasting surface albedo at these wavelengths allows an ambiguity to be removed in what would be a double valued relationship between cloud optical depth and zenith radiance [1]. There was interest in seeing if we could reproduce their work at our very different site in Miami. What follows is a description of the method and adaptations taken.

First, in order to understand this method better, I show a typical curve for zenith radiance versus cloud optical depth, Fig. 5.1, using the DISORT 1D zenith radiance model assuming homogeneous clouds at 50 degrees solar zenith angle, which is discussed in detail later in this chapter. It can be seen that for many values of radiance there are two possible optical depths. Thus with radiance at just one wavelength, there is ambiguity about the true optical depth. However if we have another wavelength associated with another curve and pair of solutions, we can match the solution from each curve to isolate the unique solution. To do this in a practical way, we need to make a measurement of the radiance with wavelengths that have distinct curves of zenith radiance vs cloud optical depth, which happens when there is large contrast in the surrounding surface albedo for two wavelengths. For example in the case of a heavily vegetated surface, the albedo in the infrared is bright, but the albedo is significantly lower in the red. The method then depends on finding wavelengths with contrasting albedos.

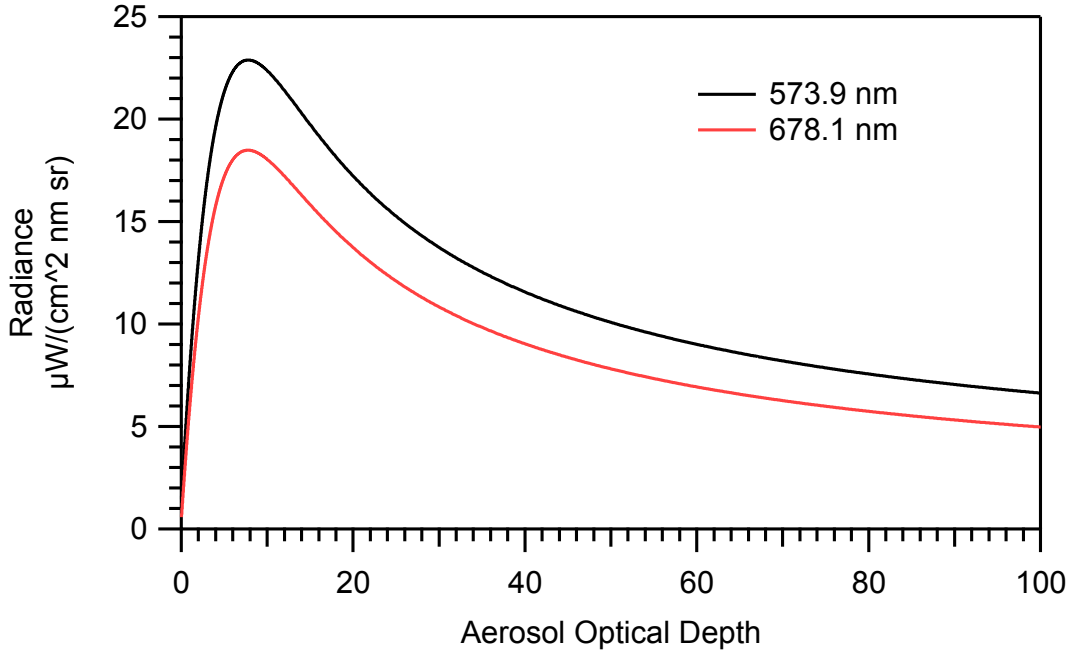

Figure 5.1: DISORT 1D zenith radiance model assuming homogeneous clouds for a solar zenith of 50 degrees and a cloud fraction of 0.5. The problem of solving for optical depth using one wavelength is that the model is not single valued for certain radiance values. If we can constrain the problem to low optical depth, however, it is possible to directly determine cloud optical depth for one wavelength. In this example, the maximum occurs at AOD = 7.88.

5.1 Mie Scattering

To apply this method, we need to understand the interaction between the light emitted from the sun, the atmosphere, and the surface reflections. Consider light entering the atmosphere at some angle. On its journey through the atmosphere the light is attenuated by both aerosols and molecules. The aerosol scattering contribution is taken into account by Mie scattering, while the molecular scattering can easily be calculated with the Rayleigh scattering approximation. Rayleigh scattering is a near constant presence in the atmosphere, but the most interesting part is the larger Mie scattering particles. More precisely speaking, Mie scattering can account for both situations as Rayleigh scattering can be thought of as the small particle approximation of Mie scattering. The determining factor is the ratio

between particle radius and the wavelength, or the size parameter:

$$x = \frac{2\pi a}{\lambda} \tag{5.1}$$

When the size parameter is 0.2 or lower, Rayleigh scattering is considered an effective solution, and makes calculation easy because the scattering phase function for Rayleigh is well known and independent of the exact particle details, such as shape [3].

$$p(\theta) = \frac{3}{4}\left(1 + \cos^2\theta\right) \tag{5.2}$$

where θ is the scattering angle.

Clouds fall into the Mie range for visible light. For example, an 8 μm cloud droplet illuminated by wavelengths starting in the visible, 410 nm, and ending in the near infrared, 860 nm, has size parameters varying from 15.3 to 7.3. Fig. 5.2 shows the different scattering regimes versus the size and wavelength of atmospheric particles. As seen in the figure, cloud droplets can fall into the Mie, Rayleigh, and Negligible Scattering categories depending on the wavelength of light. All of our measurements are below 1 micron in wavelength.

With this in mind, we used Miev, a Mie scattering code written in FORTRAN using Wiscombe's Mie scattering algorithm[46]. It requires as an input the size parameter and particle index of refraction. It outputs the scattering phase function along with the single scatter albedo and coefficients of the Legendre polynomial expansion of the scattering phase function.

Mie Theory is a solution to the Maxwell equations under specific requirements. It starts by assuming that the particles are homogeneous spheres, and by applying a separation of variables in spherical polar coordinates of the form:

$$u\left(r, \theta, \phi\right) = R\left(r\right) Y\left(\theta, \phi\right). \tag{5.3}$$

It is very similar to how the Schrödinger equation is solved in three dimensions.

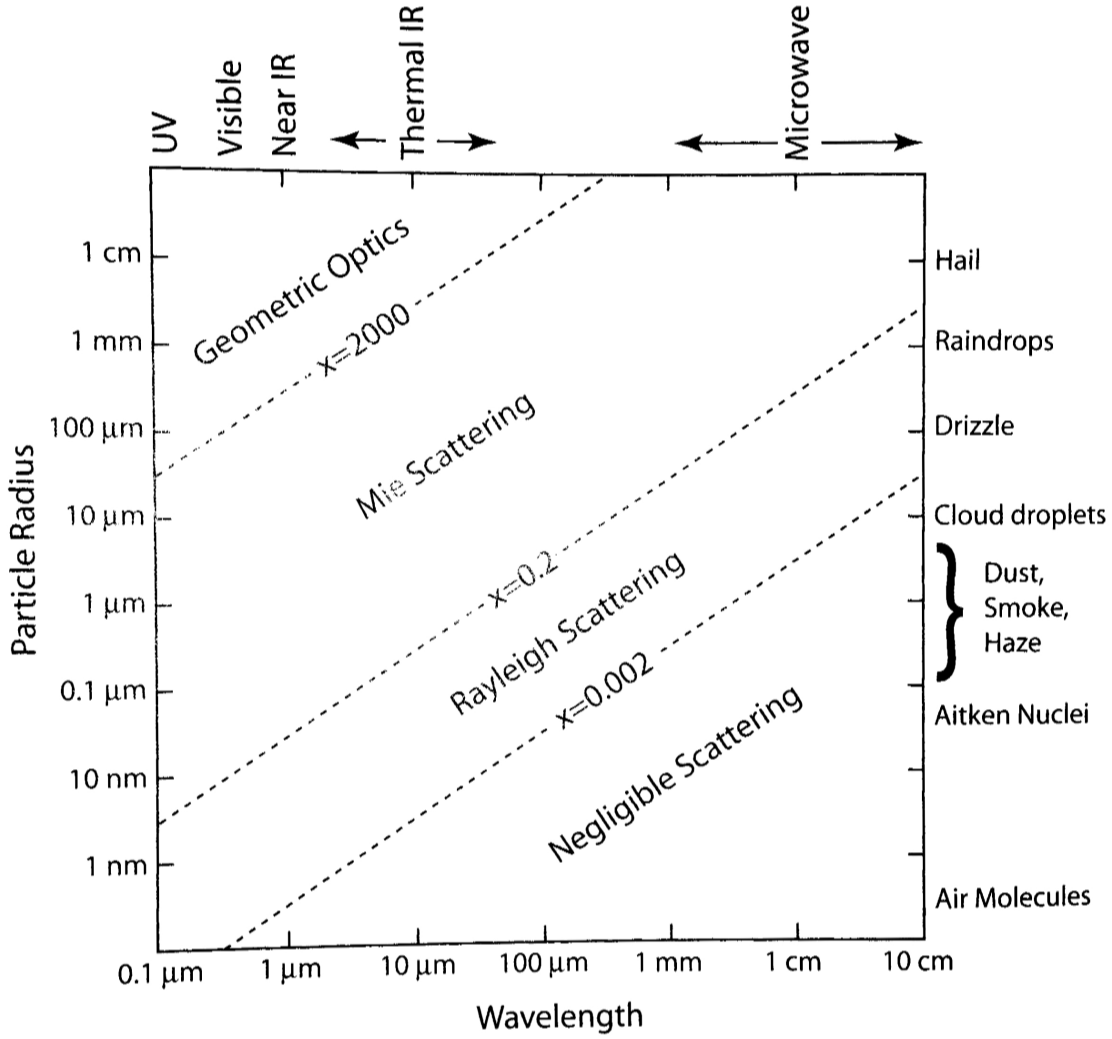

Figure 5.2: Relationship between particle size, radiation wavelength and scattering behavior for atmospheric particles. Diagonal dashed lines represent rough boundaries of the scattering regimes. Reproduced from Petty Fig 12.1 [3]

The solution will contain a radial component, $R(r)$, and a spherical harmonics component, $Y_l^m(\theta, \phi)$. Within the spherical harmonics component the zenith angle (θ) dependence contains the Legendre Polynomials, $P_l(\theta)$. In Mie Scattering, the Legendre Polynomials are important because the scattering phase function, $p(\cos\theta)$, can be described as an expansion in Legendre Polynomials [3, p.427,A.1]:

$$p(\cos\theta) = \sum_{l=0}^{\infty} \beta_l P_l(\cos\theta) \tag{5.4}$$

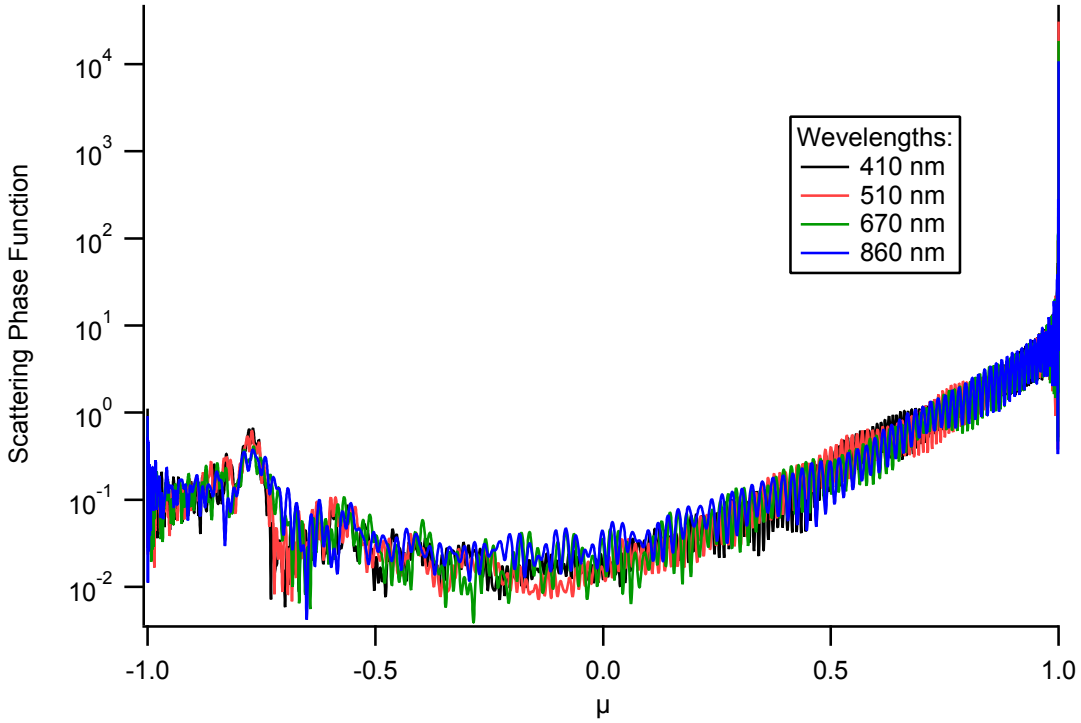

Figure 5.3: Cloud Droplet normalized scattering phase functions calculated from Mie Code for several wavelengths and an effective radius of 20 microns

We use Miev to calculate the β_l coefficients for a given size parameter and index of refraction. However the Miev Mie code outputs slightly modified coefficients, P_{mom} such that: [47]:

$$\beta_l = P_{mom}(l)\,(2l+1) \tag{5.5}$$

The radiative transfer code DISORT accepts these coefficients, $P_{mom}\,(l)$, in this same form, and will be discussed in further detail the following section.

5.2 DISORT Zenith Radiance Model

For our model, we considered cloud droplets of radius 20 μm averaged over ± 5 μm using a Gaussian distribution with width 2.5 μm and the wavelength from 400 to 900 nm, corresponding to the radiometer's measurement wavelengths. We based the droplet radius and standard deviation on values for cumulus clouds [48], which

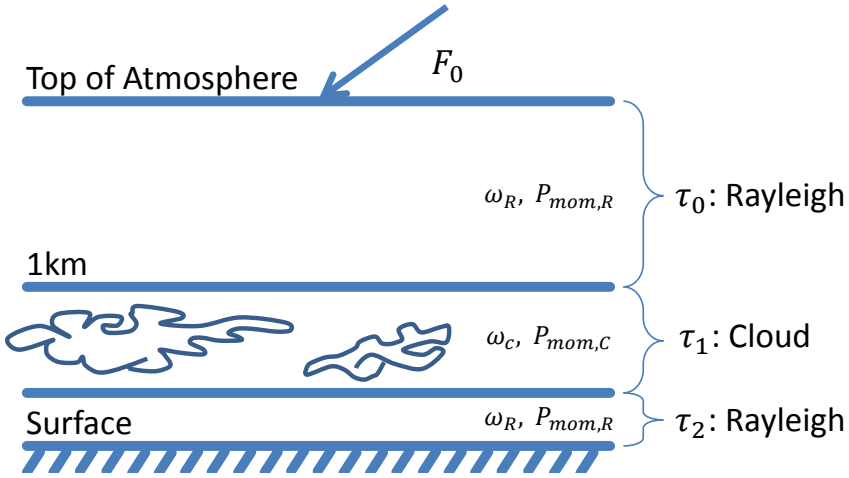

Figure 5.4: Scattering Medium considered for zenith radiance model where τ_0 is Rayleigh optical depth from the top of the atmosphere to 1 km, τ_1 is cloud optical depth for the cloud layer at 1 km, τ_2 is the Rayleigh optical depth from 1 km to the surface, and F_0 is solar extraterrestrial irradiance.

are the typical clouds seen in Miami. We also assumed that the clouds are liquid water and used the complex refractive as measured by Hale and Querry [1973] [8]. For each wavelength, we modeled the zenith radiance for our site assuming a plane parallel atmosphere using DISORT, a program that solves the radiative transfer equation in a multiple scattering atmosphere [49]. The key inputs of DISORT are top of atmosphere incoming irradiance, solar zenith angle, surface albedo, and layer optical properties such as single scatter albedo, optical depth and Legendre polynomials as defined in Eq. 5.5. For the incoming irradiance at the top of the atmosphere we used direct normal extraterrestrial solar irradiance F_0 provided in Thuillier[2].

The scattering medium has three layers which are two Rayleigh layers surrounding a cloud layer located at 1 km. Figure 5.4 illustrates the scattering medium. For each layer we have to determine the single scatter albedo, ω, and Legendre polynomials coefficients, P_{mom}. We start with the Rayleigh layer. To find P_{mom} we

use the Rayleigh scatter phase function from Eq. 5.2 and set it equal to Legendre Polynomial expansion from Eq. 5.5:

$$p(\theta) = \frac{3}{4}\left(1 + \cos^2\theta\right) = \sum_{l=0}^{\infty}\left(2l+1\right)P_{mom}\left(l\right)P_l\left(\cos\theta\right) \tag{5.6}$$

The Rayleigh Legendre polynomial coefficients are:

$$P_{mom,R}(0) = 1,\ P_{mom,R}(2) = 1/10,\ \text{and}\ P_{mom,R}(others) = 0 \tag{5.7}$$

The single scatter albedo for Rayleigh scattering:

$$\omega_R = 1 \tag{5.8}$$

We calculated the Rayleigh optical depth for a solar light source using the 1976 US Standard Atmosphere [38] pressure profile $P(r)$ and following Hansen and Travis [7]:

$$\tau_R(r) = \tau_s\frac{P(r)}{P_0} \tag{5.9}$$

$$\tau_s = 0.008569\lambda^{-4}\left[1 + 0.0113\lambda^{-2} + 0.00013\lambda^{-4}\right] \tag{5.10}$$

$$P_s = 101,325\ \text{Pa} \tag{5.11}$$

where $\tau_R(r)$ is the Rayleigh optical depth as function of distance from the surface r, τ_s is Rayleigh optical depth at the surface, and P_s is the surface pressure. These equations are a modification of the equations for the Rayleigh profile in the MPL signal to account for the difference in perspective. With zenith radiance, the light source (the Sun) is the top of the atmosphere and heads towards the surface. Consequently, the optical depth from Rayleigh scattering will be greatest at the surface. Conversely, with the MPL, the light source is at the surface and heads towards the top of the atmosphere, and the optical depth from Rayleigh scattering will be greatest at the top of the atmosphere. For the top layer, we have:

$$\tau_0 = \tau_R(1km) \tag{5.12}$$

For the bottom layer, we have total column optical depth minus the Rayleigh component to the cloud layer:

$$\tau_2 = \tau_s - \tau_0 \tag{5.13}$$

We use Mie scattering to find ω_C and $P_{mom,C}$ for the cloud layer. Then, we compute the zenith radiance as a function of cloud optical depth. The surface radiance due to cloud and surface interaction can be expressed as [50]:

$$L(\tau, A_c) = L_0(\tau) + \frac{\rho T_0(\tau, A_c) L_s(\tau)}{1 - \rho R(\tau)} \tag{5.14}$$

where the first term L_0 is the downwelling radiance calculated for a black surface, and the second term is the cloud-surface interaction assuming a Lambertian surface with albedo ρ; and where L_s is the radiance from the surface, $T_0(\tau, A_c)$ is the transmittance of monochromatic radiance over a black surface from the surface to the bottom of the cloud, A_c is effective cloud fraction, and R is the spherical albedo of clouds [51, 1]. The transmittance $T_0(\tau, A_c)$ is approximated by:

$$T_0(\tau, A_c) = 1 - A_c + A_c \cdot T_{0,pp}(\tau) \tag{5.15}$$

where $T_{0,pp}$ is total transmittance over a black surface in a plane-parallel atmosphere.

5.3 Two Wavelength Method for Cloud Optical Depth Method from Zenith Radiance

The two wavelength method for cloud optical depth, works by creating zenith radiance models at different cloud optical depths and effective cloud fractions for wavelength pairs. I start with a pair of matrices, one for each wavelength, populated with radiance values from the cloud model. The rows represent varying cloud optical depths from 0 to τ_{max}. The columns represent varying effective cloud

fraction from 0 to $A_{c_{max}}$. The model zenith radiance matrices have the form:

$$L_{\tau,A_c}(\lambda,\theta_s,\alpha_\lambda) = \begin{bmatrix} L_{\tau_1,A_{c_1}} & L_{\tau_1,A_{c_2}} & \cdots & L_{\tau_1,A_{c_{max}}} \\ L_{\tau_2,A_{c_1}} & L_{\tau_2,A_{c_2}} & \cdots & L_{\tau_2,A_{c_{max}}} \\ \vdots & \vdots & \ddots & \vdots \\ L_{\tau_{max},A_{c_1}} & L_{\tau_{max},A_{c_2}} & \cdots & L_{\tau_{max},A_{c_{max}}} \end{bmatrix} \tag{5.16}$$

where τ is cloud optical depth, A_c is effective cloud fraction, λ is wavelength, θ_s is solar zenith angle, α_λ is surface albedo. Since we look at pairs of wavelength, we have two matrices. Let us label a matrix for one wavelength $L_{\tau,A_c}(\lambda_1,\theta_s,\alpha_{\lambda_1})$ as L_1 and another $L_{\tau,A_c}(\lambda_2,\theta_s,\alpha_{\lambda_2})$ as L_2.

We want to create a two dimensional lookup table to find cloud optical depth through 2d interpolation. The routine that we use for 2d interpolation uses the row and column values to return the interpolation value. With this in mind, we need a lookup table whose elements are populated by cloud optical depth values, the rows are defined by one wavelength's model radiances, and the columns are defined by the other wavelengths model radiances. The desired matrix has the form:

$$\tau_{L_1,L_2}(\lambda_1,\lambda_2,\theta_s,\alpha_{\lambda_1},\alpha_{\lambda_2}) = \begin{bmatrix} \tau_{L_{1_1},L_{2_1}} & \tau_{L_{1_1},L_{2_2}} & \cdots & \tau_{L_{1_1},L_{2_{max}}} \\ \tau_{L_{1_2},L_{2_1}} & \tau_{L_{1_2},L_{2_2}} & \cdots & \tau_{L_{1_2},L_{2_{max}}} \\ \vdots & \vdots & \ddots & \vdots \\ \tau_{L_{1_{max}},L_{2_1}} & \tau_{L_{1_{max}},L_{2_2}} & \cdots & \tau_{L_{1_{max}},L_{2_{max}}} \end{bmatrix} \tag{5.17}$$

To achieve this result, we stack the columns of matrix L_1 from Eq. 5.16 so that it forms a vector:

$$L_{vec\,1} = \begin{bmatrix} \begin{bmatrix} L_{\tau_1,A_{c_1}} \\ \vdots \\ L_{\tau_{max},A_{c_1}} \end{bmatrix} \\ \begin{bmatrix} L_{\tau_1,A_{c_2}} \\ \vdots \\ L_{\tau_{max},A_{c_2}} \end{bmatrix} \\ \vdots \\ \begin{bmatrix} L_{\tau_1,A_{c_{max}}} \\ \vdots \\ L_{\tau_{max},A_{c_{max}}} \end{bmatrix} \end{bmatrix} \tag{5.18}$$

Similarly, we create vectors for L_2 and τ. Then, we use a routine which converts XYZ data to matrix form, with X as $L_{vec\,1}$, Y as $L_{vec\,2}$, and Z as τ_{vec}. The result of the routine is the matrix from Eq.5.17. Then, it just becomes a question of using a two dimensional interpolation on the optical depth matrix, τ_{L_1,L_2}, with the pair of radiance values as the x and y coordinates of that matrix. Similarly, I created a two dimensional lookup table for effective cloud fraction.

5.4 Cloud Optical Depth Measurements

At the CARObb Site in RSMAS, we have several devices capable of measuring parameters which can be used to calculate the optical depth, such as the polarized micro-pulse LIDAR (MPL), the two Aeronet Cimel photometers, and the zenith radiometer. We were interested in comparing the cloud optical depth obtained from the MPL and zenith radiance for optically thin clouds. We attempted to adapt the method of Marshak et al. [1] for measuring cloud optical depth from zenith radiance. In their case, they used high/bright surface albedo in the near infrared and low/dark surface albedo in the red for contrasting albedo. In our case, we need to use two very different wavelengths. We also found that since we are focusing on optically thin clouds a much simpler one wavelength approach could be taken to derive the cloud optical depth from our zenith radiance measurements.

Initially, we were using the radiometer located outside on the roof to measure zenith sky radiance, but we discovered that changes in instrument temperature were causing large variations in the data due to dark current variations. In order to avoid temperature variations we decided to bring the device indoors and put it next to the LIDAR viewing window in the roof, but now with the instrument temperature stabilized. However, the radiometer was too large and we switched to the Ocean Optics fiber coupled spectrometer which we had previously used to measure the surface albedo. The advantage is that it has a very small footprint

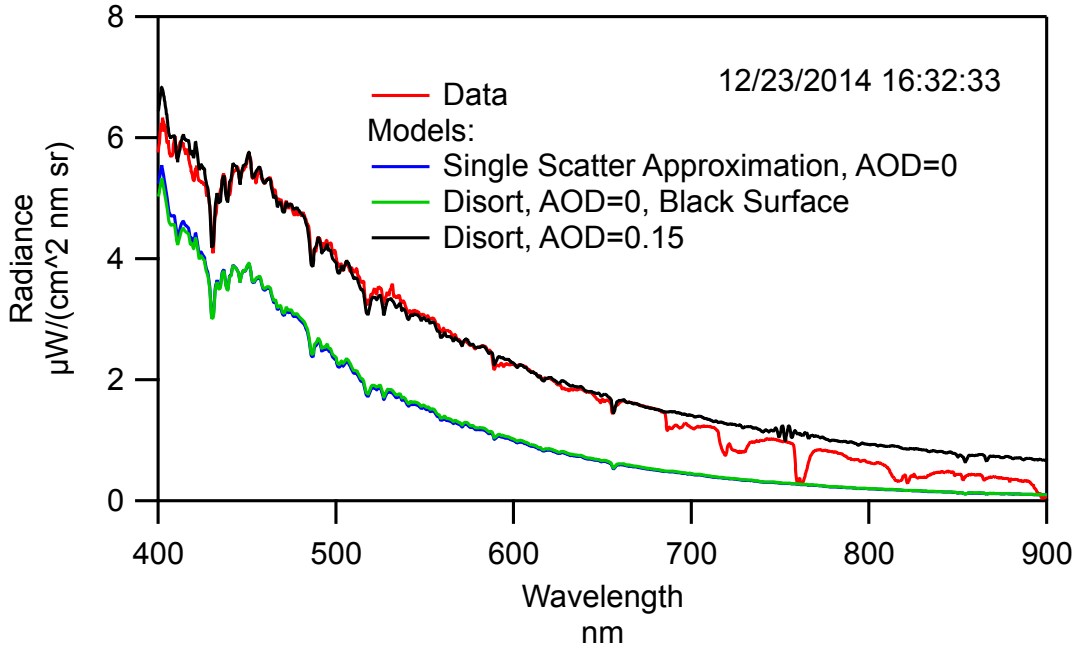

Figure 5.5: Clear sky radiance spectrum. The single scatter approximation, assuming AOD = 0, is a simple model which we used to compare with the DISORT model. If we assume AOD = 0 and a black surface albedo, the DISORT cloud model corresponds well to the single scatter approximation. However, you can still see that both of those models lie below the radiance data. If you assume an optical depth of 0.15 for this time slice and the effective surface albedo, as in Fig. 4.11, the DISORT model matches the radiance data very well. The deviations, or dips, can be attributed to the water vapor and other gas absorption lines.

and in addition is hyperspectral with 1.2 nm spectral resolution from 400 to 900 nm. The old radiometer was multichannel with only 6 discrete wavelengths. This gives us more freedom to pick wavelengths that work well for this experiment.

Analysis of spectral radiance, as in Fig. 5.5, shows that there is very good agreement between model and data up until 685 nm. Above this region, we can start to see the effect of water vapor and other atmospheric gas absorption bands which are not currently accounted for in our model. Nevertheless, we have many wavelengths which we can use to solve for cloud optical depth. We started with 573.9 and 678.1 nm because they seemed to provide the largest contrast in the surface albedo spectrum. Fig. 5.5 shows three models: two DISORT models and

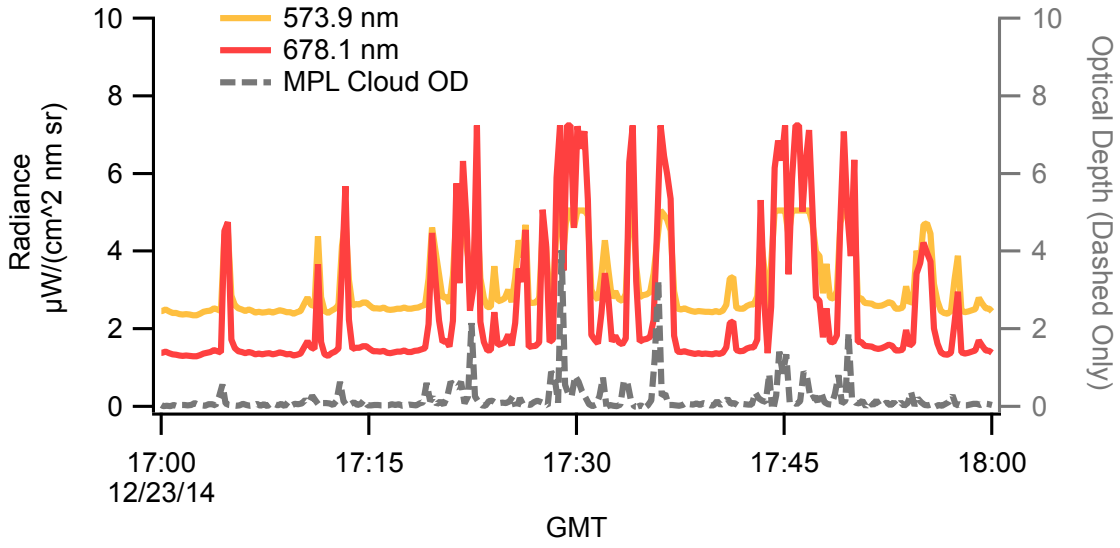

Figure 5.6: Radiance time series for various wavelengths. (Right Axis): MPL Cloud Optical Depth Time Series. Compare the radiometer's radiance response to the MPL's clouds optical depth. Peaks coincide with clouds. We developed criteria for how big a cloud's NRB peak must be to be considered a cloud. The radiance can saturate when optically thick clouds are overhead which corresponds to the flat peaks particularly at 575 nm. This loss of data can be avoided by lowering the integration time on the spectrometer.

a single scattering approximation. To check the consistency we compare the single scattering approximation and the DISORT zenith radiance for a black surface and zero AOD. The single scattering approximation for zenith radiance and zero AOD is [52]

$$L_{SSA}(\lambda) = \frac{3}{16\pi}\tau_R(\lambda)F_0(\lambda)\left(1+\cos^2\theta_s\right) \tag{5.19}$$

where $F_0(\lambda)$ is the extraterrestrial solar irradiance. We find that DISORT and single scatter approximation have very good agreement. However, if we want DISORT to match the data, we have to consider the albedo and AOD. In Fig. 5.5 we needed to use an AOD of about 0.15 for that time sample, which matches the Aeronet AOD for that time.

For comparison, we calculated the cloud optical depth from the LIDAR data during the same time interval. The time series can be seen in Fig. 5.6. The time-

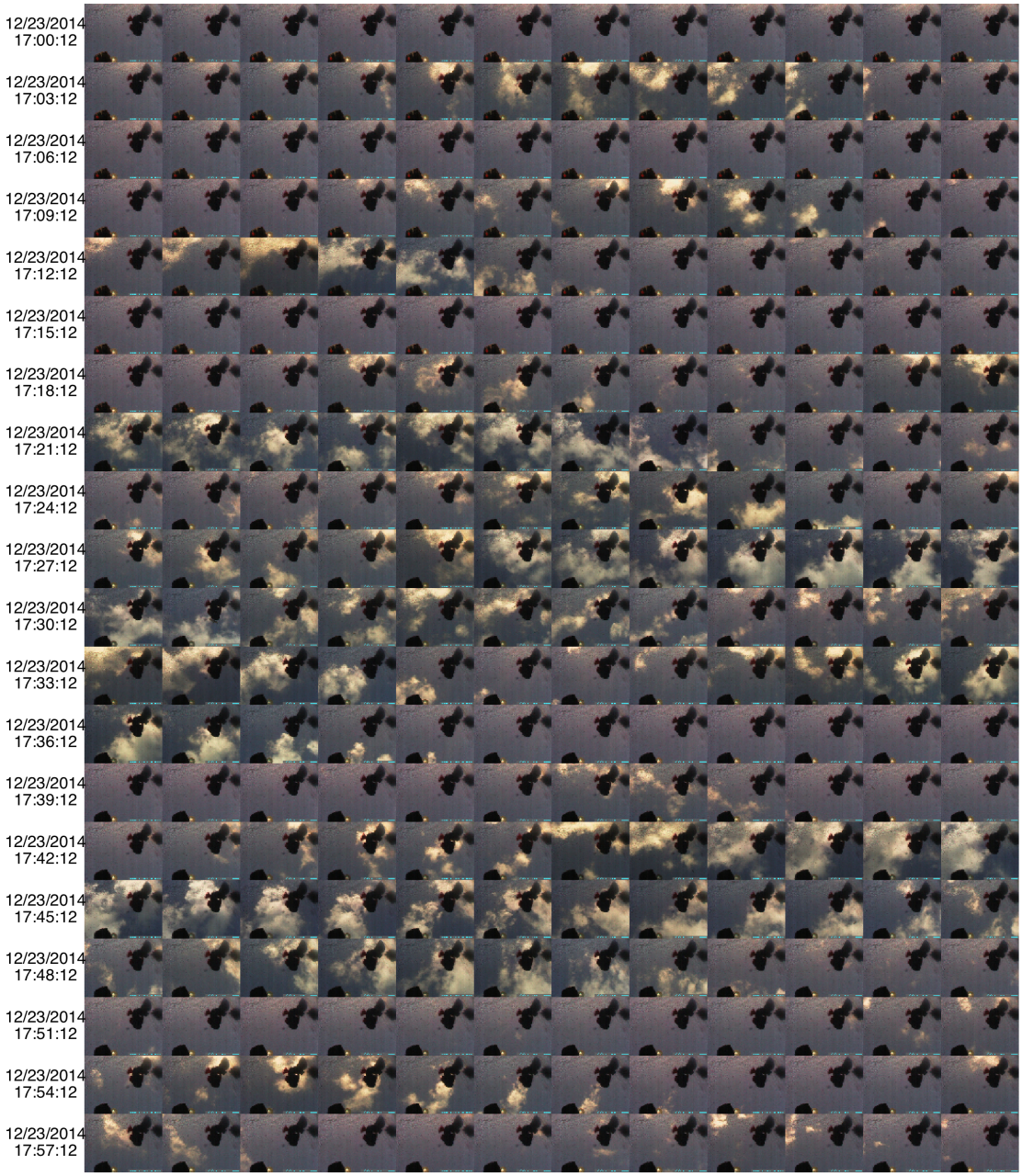

Figure 5.7: Time-lapse images on 12/23/2014 17:00 to 18:00 GMT. Every row consists of 3 minutes of consecutive images taken every 15 seconds. These images serve as a realistic check for the true cloud scenario above the LIDAR and radiometer. For example, the MPL cloud optical depth data indicates that there are clouds between 17:42 to 17:48, which are also present in the time-lapse images.

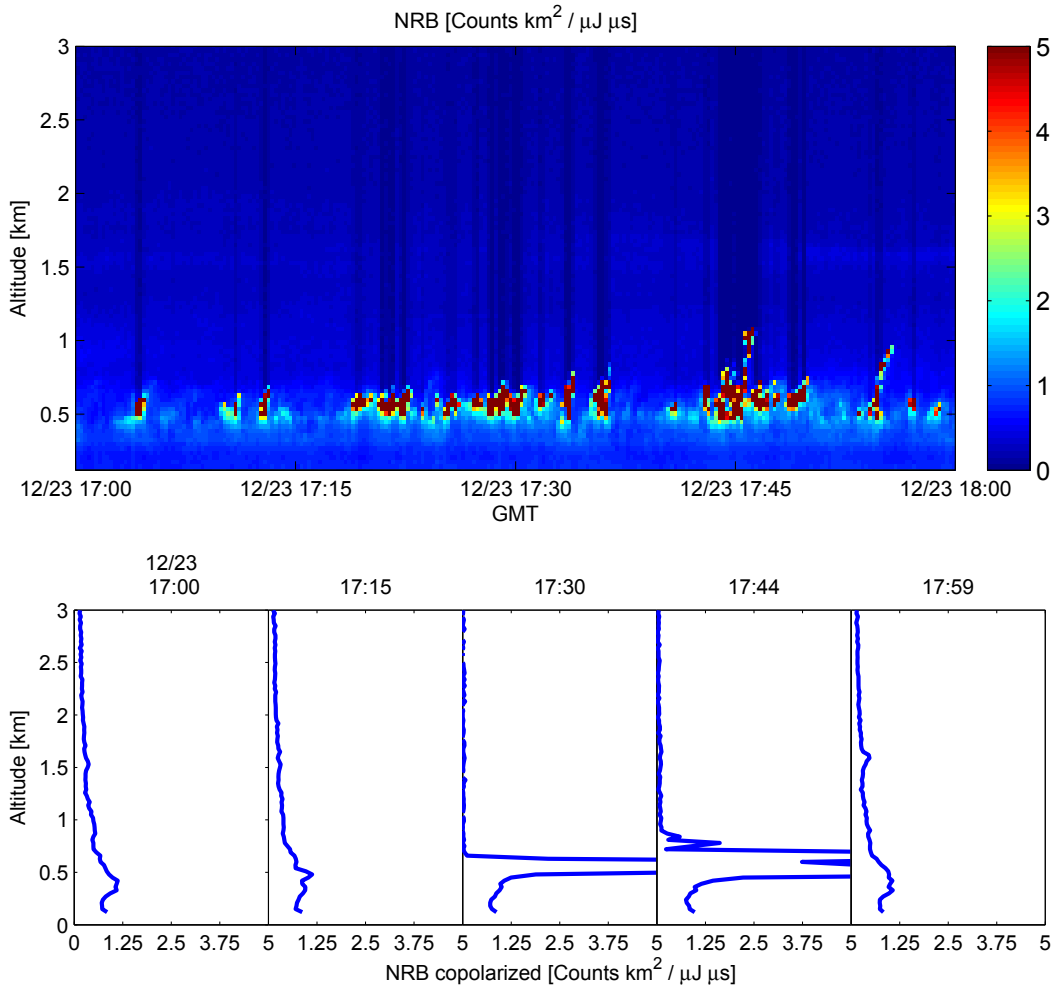

Figure 5.8: Co-polarized NRB profiles for 12/23/2014 17:00 to 18:00 GMT. Clouds in this image have an NRB greater than 5 Counts $km^2/\mu J\mu s$.

lapse images in Fig. 5.7 are used to compare occurrences of radiance maxima to real-world clouds. The Normalized Relative Backscatter (NRB) profile from Fig. 5.8 reveals that visible clouds in this time period typically surpassed 5 Counts $km^2/\mu J\mu s$.

We considered two methods to calculate cloud optical depth from the zenith sky radiance. First, we followed the method outlined in Marshak et al. [1] with pairs of wavelengths, unfortunately with our radiometer settings our radiometer saturates at one of the wavelengths for higher optical depth (Fig. 5.9). Also, our

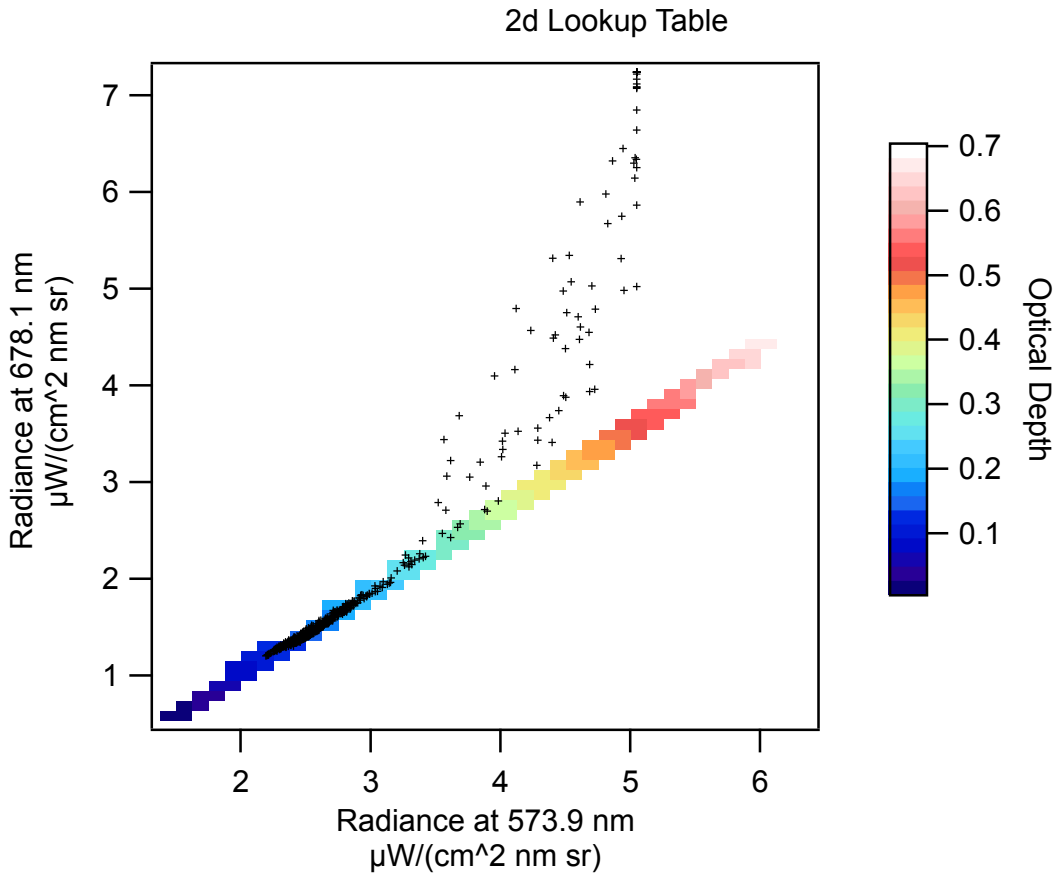

Figure 5.9: 678.1 nm vs 573.9 nm Radiance with the color map representing the cloud model, and the black crosses represent the radiometer data. By finding the radiance pair's location on the model, one can find the optical depth. Notice that the data starts to leave the model at optical depths over 0.30. This is likely due to saturation. For example, the maximum radiance for 573.9 nm is around 5.05 $\mu W/(cm^2 nm\ sr)$. Any data beyond this radiance would be lost. The other points below this limit that are outside the model area were likely saturated but averaged with lower radiance values in the 15 second time interval between data points.

MPL routine was limited to optically thin clouds as they could be reliably retrieved by the LIDAR inversion. Since our situation is really in the linear portion of the sky radiance model, we realized that we only needed one model wavelength.

Comparison of these two methods for determining cloud optical depth from sky radiance are shown in Fig. 5.10. The two wavelength method, Fig. 5.10a, fails to capture optically thick cloud peaks that are picked up by the MPL, but this is due

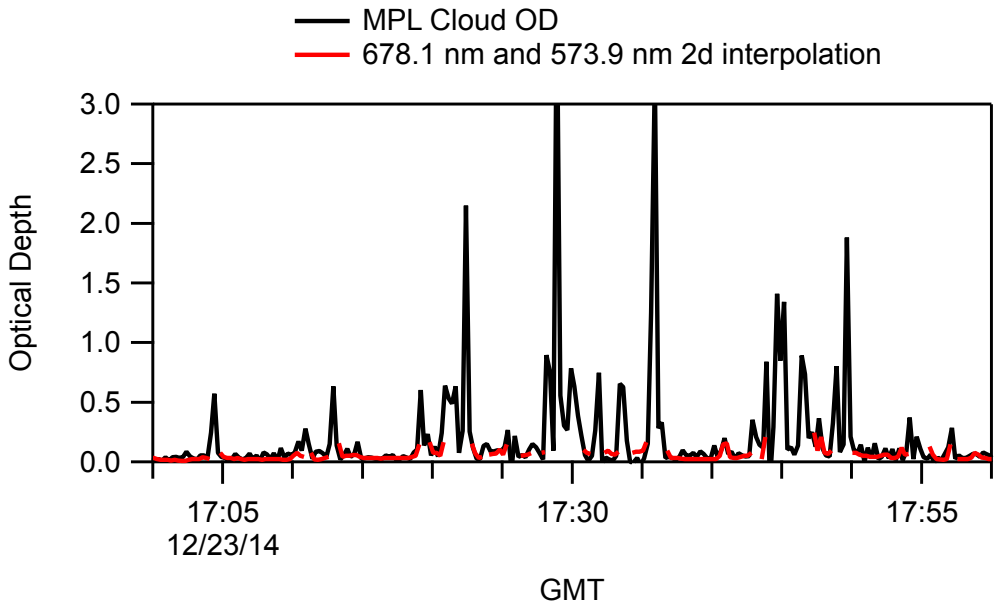

(a) 2D interpolation

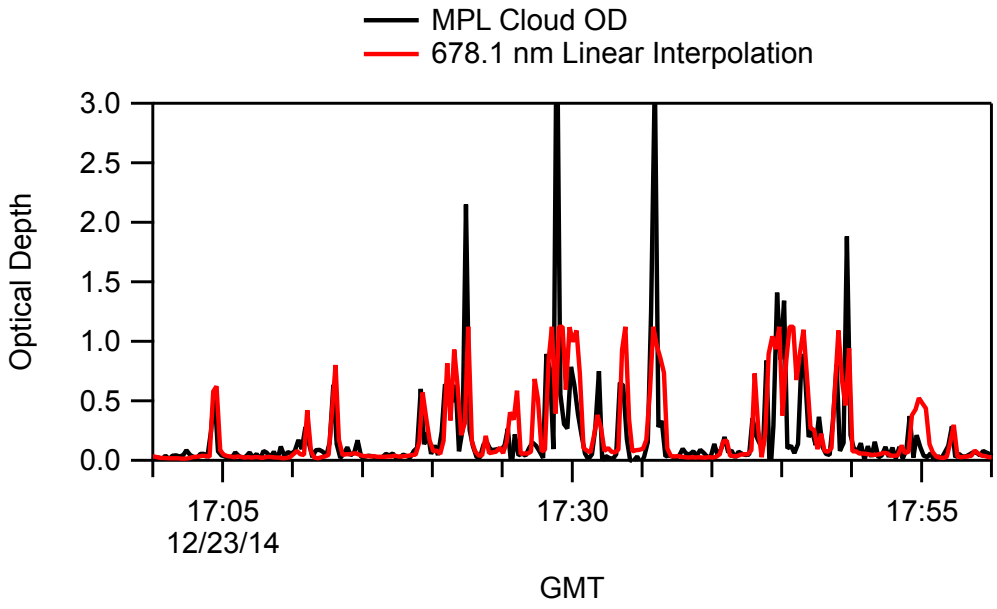

(b) 1D interpolation

Figure 5.10: Comparison between two and one wavelength interpolation methods. The one wavelength (linear interpolation) method is more responsive for cloud optical depths greater than 0.3 than the two wavelength method.

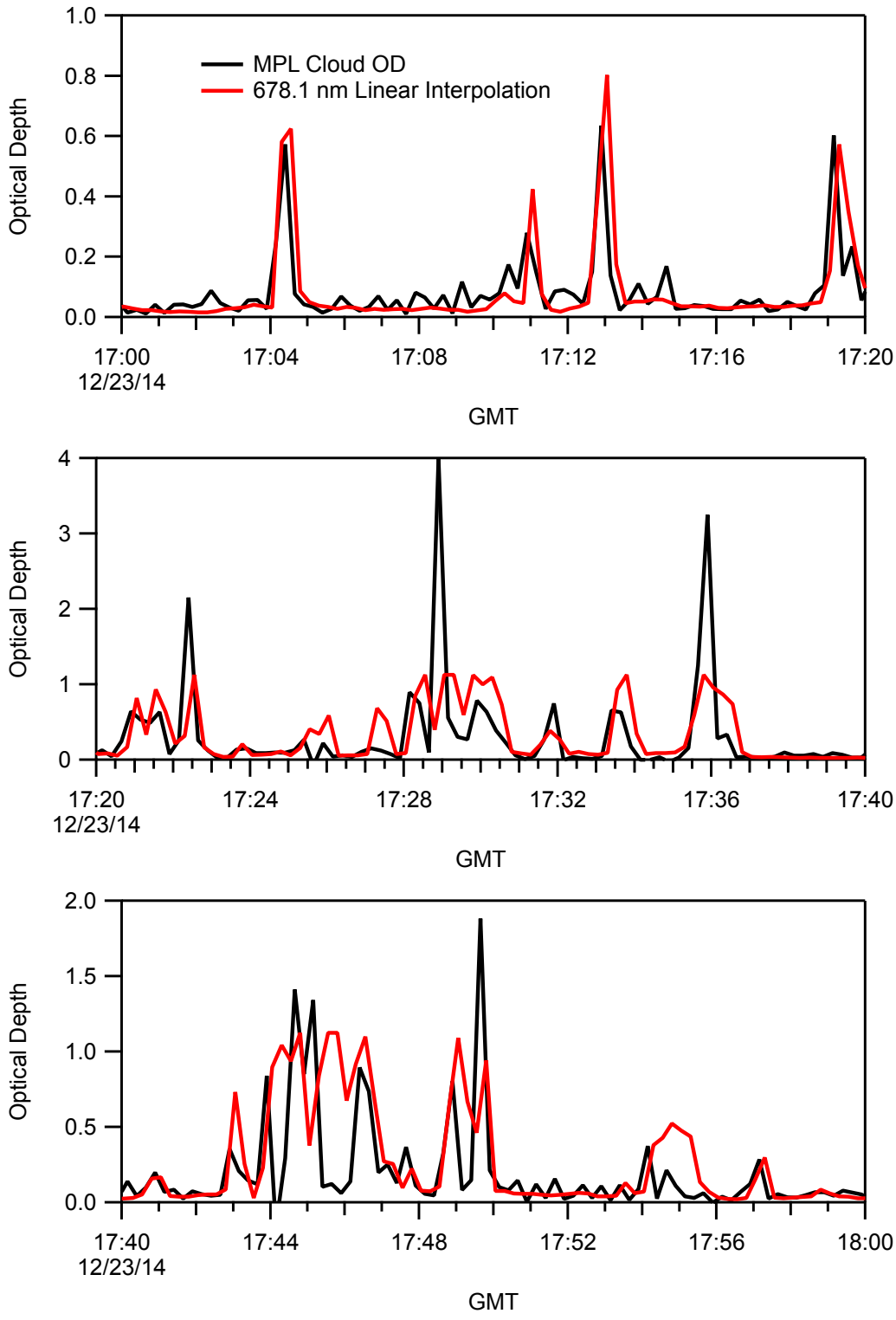

Figure 5.11: One wavelength method displayed in 20 minute intervals for cloud optical depth reveal good agreement between the two instruments.

to saturation of the radiance channels when there are thick clouds were overhead. Fig. 5.9 shows where the data is located in relation to the 2d radiance model for 678.1 and 573.9 nm. Ideally, all the data (black dots) would lie inside the confines of the color map generated for 678.1 vs 573.9 nm Zenith Radiance. However, you can see that for cloud optical depth above 0.30 the data deviates from the predicted possible values of the model. We realized that these deviations correspond to saturated radiance points, which appear as flat peaks in Fig. 5.6. The loss of data due to saturation can be overcome by decreasing the integration time for future measurements. The integration time was 250 ms and the radiance spectra were averaged for 15 second intervals. When there are very high or saturated values within the average, the result is erroneous, which explains the range of values of outside the model, or a smearing of saturated with non-saturated values. Another fix for this could be to take single measurements without averaging for 15 second intervals. This would minimize the smearing effect that we see from averaging. It may also be interesting to decrease the sample intervals to 5 seconds or lower to capture rapid transitions.

We find very good agreement between the MPL and zenith radiance derived AOD with the single wavelength method as shown in Fig. 5.11. Since the 678.1 nm radiance data is the least saturated wavelength, we use this wavelength for the linear interpolation. In this case, we see many of the same clouds peaks as seen in the MPL. We also found that the sky radiance method had an optical depth of 0.10 higher than the MPL method. This is most likely because the MPL cloud optical depth has the aerosol background portion removed, whereas the sky radiance method contains both cloud and aerosol background contributions. The AERONET aerosol optical depth for that day averaged around 0.1 for 675 nm, which would account for the offset in the sky radiance method to the MPL method.

Chapter 6

Error Analysis and Sensitivity

In this chapter we will analyze the sensitivity of the 1D zenith radiance cloud model to the parameters used in this work. The key model input variables are particle size, surface albedo, and solar zenith angle. For measurements in the previous chapter, we used a cloud particle size of 20 μm, an albedo of 0.0899 for $\lambda = 678.1\,nm$ and a solar zenith angle equal to 50°. For simplicity, we will focus on $\lambda = 678.1\,nm$, but given the similar optical properties for light in the visible spectrum we should expect similar relationships in the visible spectrum. By modifying these three key variables and producing new lookup tables we can get the variation of the derived cloud optical depth (COD) with these parameters. Then, by calculating the percentage that the COD has changed from the original value, we can find the induced percent error as a function of these key input variables.

6.1 Effective Cloud Particle Size

Through Mie scattering, the size parameter ($x = \frac{2\pi a}{\lambda}$), which depends on particle size and wavelength, directly affects the zenith radiance (Fig. 6.1a) through its effect on the particle scattering phase function. We consider typical effective cloud particle sizes from 5 to 25 μm [4]. The zenith radiance model at $\theta = 50°$ has a maximum around $COD = 7.8$. We find that particle size has a bigger effect on zenith radiance for high COD than for low COD. At low COD, below $COD = 7.8$, the radiance models for various particle sizes are tightly packed. At high COD above the maximum, we see more separation between the zenith radiance models

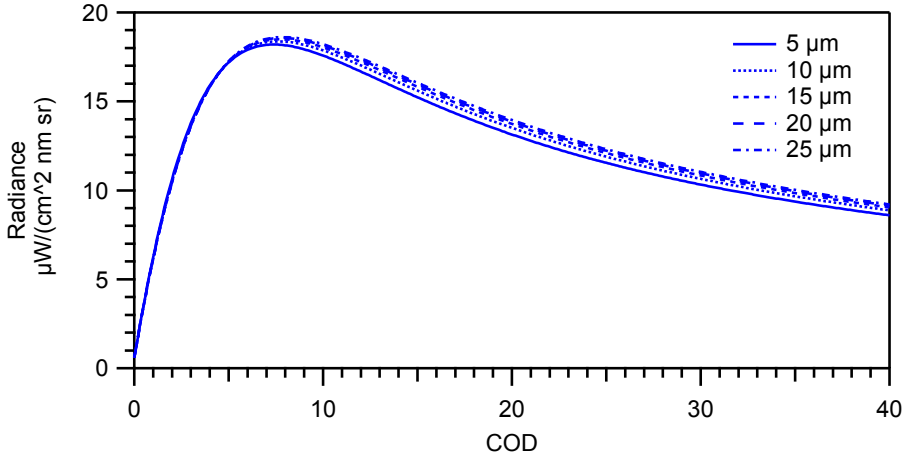

(a)

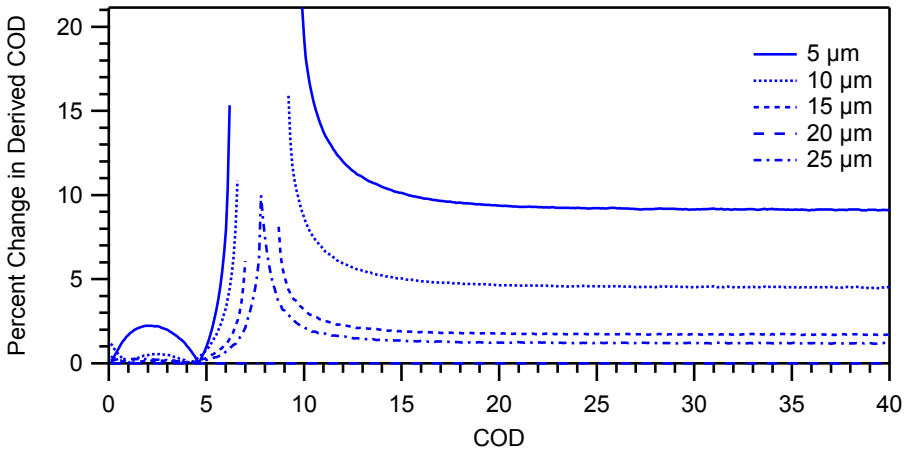

(b)

Figure 6.1: Cloud particle size's effect on the derived cloud optical depth (COD). (a) Zenith radiance models for different particle sizes. (b) Percent change in derived COD for 678.1 nm for different particle sizes. Percent change shown is with respect to the 20 μm model. Models shown here have an effective cloud fraction of 0.5 and a solar zenith angle of 50°.

for the different particle sizes. Consequently, for typical cloud effective particle sizes from 5 to 20 μm there is not a large dependence on particle size in the low COD region we are studying here. Figure 6.1b shows the percent change in COD when compared to the 20 μm model.

In terms of an error budget, we can determine how the COD will differ if the particle size was really 5, 10, 15, or 25 μm versus our assumed value of 20 μm? For COD less than 5, we see a percent error less than 2% and for COD larger than 15, we see a percent error less than 10% (Fig 6.1b). Thus, for optically thin clouds we have a maximum of 2% error due to particle size.

6.2 Surface Albedo

We measured spectral surface albedo, which is discussed in Ch. 4. However, there is an inherent uncertainty of 4% due to instrument error. Given the model's dependence on surface albedo to solve the radiative transfer equation, we must analyze the influence of a varying surface albedo on the derived COD. For this analysis, we varied the albedo by multiplying the measured albedo with a coefficient that varied from 0.1 to 3.0 (Fig 6.2). We find that, once again, the percent change in derived COD is larger for large COD. Optically thick clouds depend more on the local underlying surface albedo than thin clouds. A closer look at the optically thin cloud region is seen in Fig. 6.3. We find that if albedo is one tenth the original albedo that the percent change in COD varies from 2.5% ($COD = 1$) to 9% ($COD = 0.1$). If the albedo is 3 times the original albedo, the percent change in COD varies from 6% ($COD = 1$) to 20% ($COD = 0.1$).

Another way to summarize the percent change in the derived COD with changing albedo is by analysis of the contour maps in Fig. 6.4. The horizontal axis is COD and the vertical axis is albedo coefficient. The contour lines indicate the percent change in COD. These contours are used to determine the requirement on

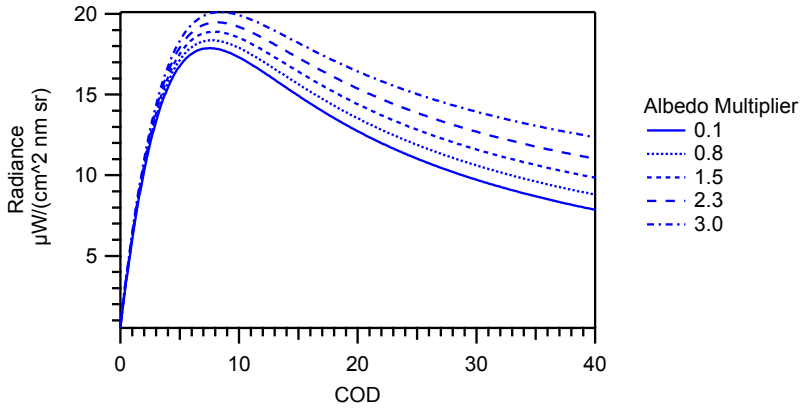

(a)

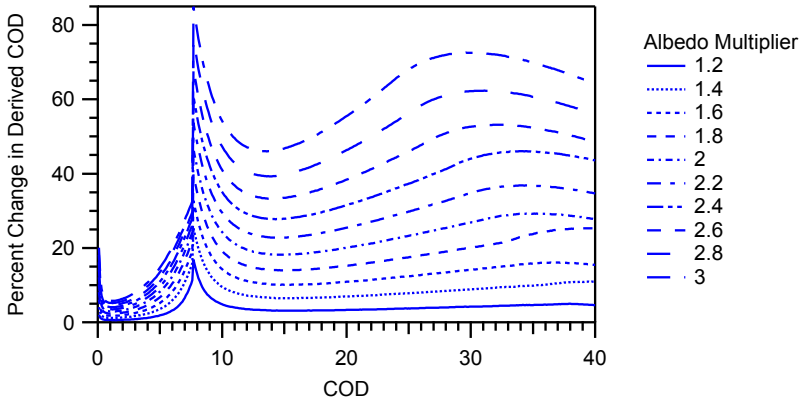

(b)

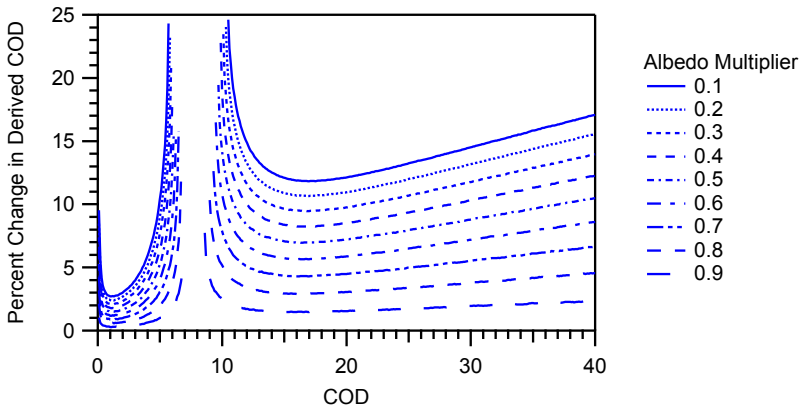

(c)

Figure 6.2: (a) Radiance resulting from changing the albedo by a factor of 0.1 to 3 times the measured albedo. (b) Resulting change in derived COD if the albedo is actually higher than we measured (by a factor of 1.2 to 3). (c) Resulting change in derived COD if the albedo is actually smaller than we measured (by a factor of 0.1 to 0.9).

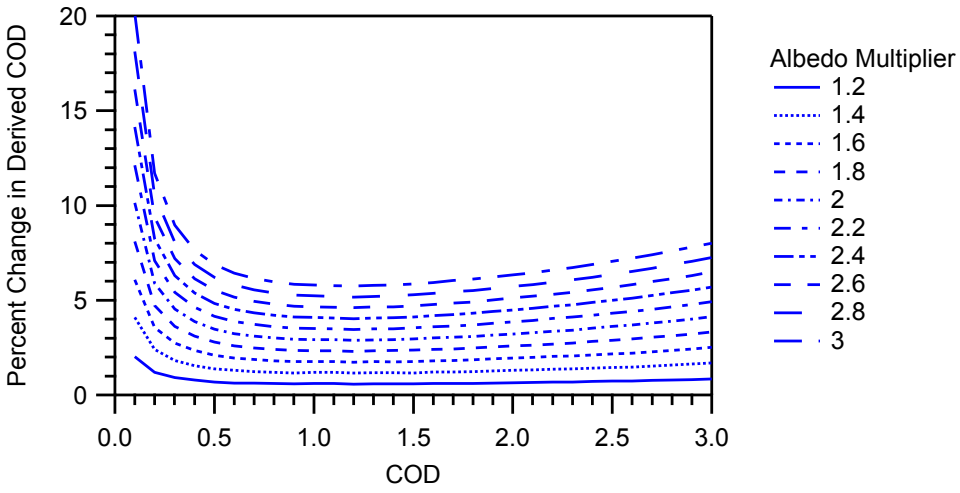

(a)

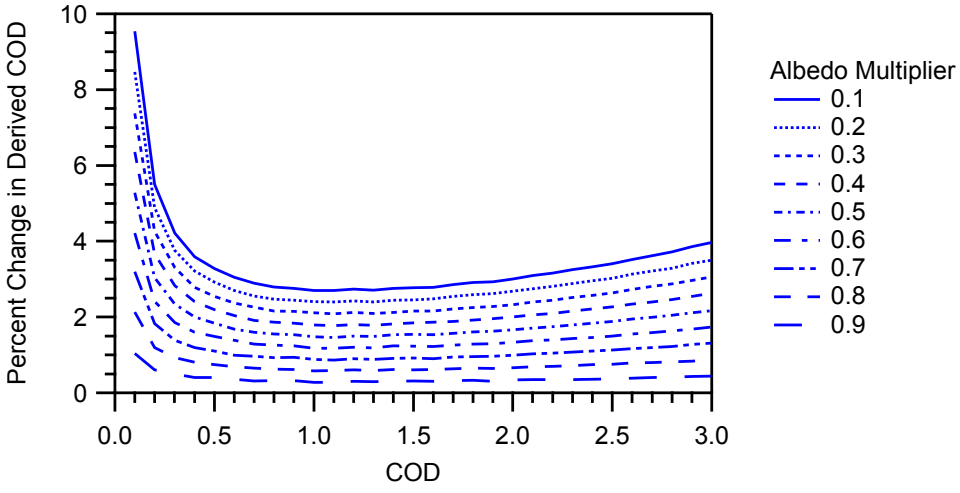

(b)

Figure 6.3: Closer look: Percent change in derived COD resulting from varying the surface albedo for COD less than 3 (a) Higher surface albedo. (c) Lower surface albedo.

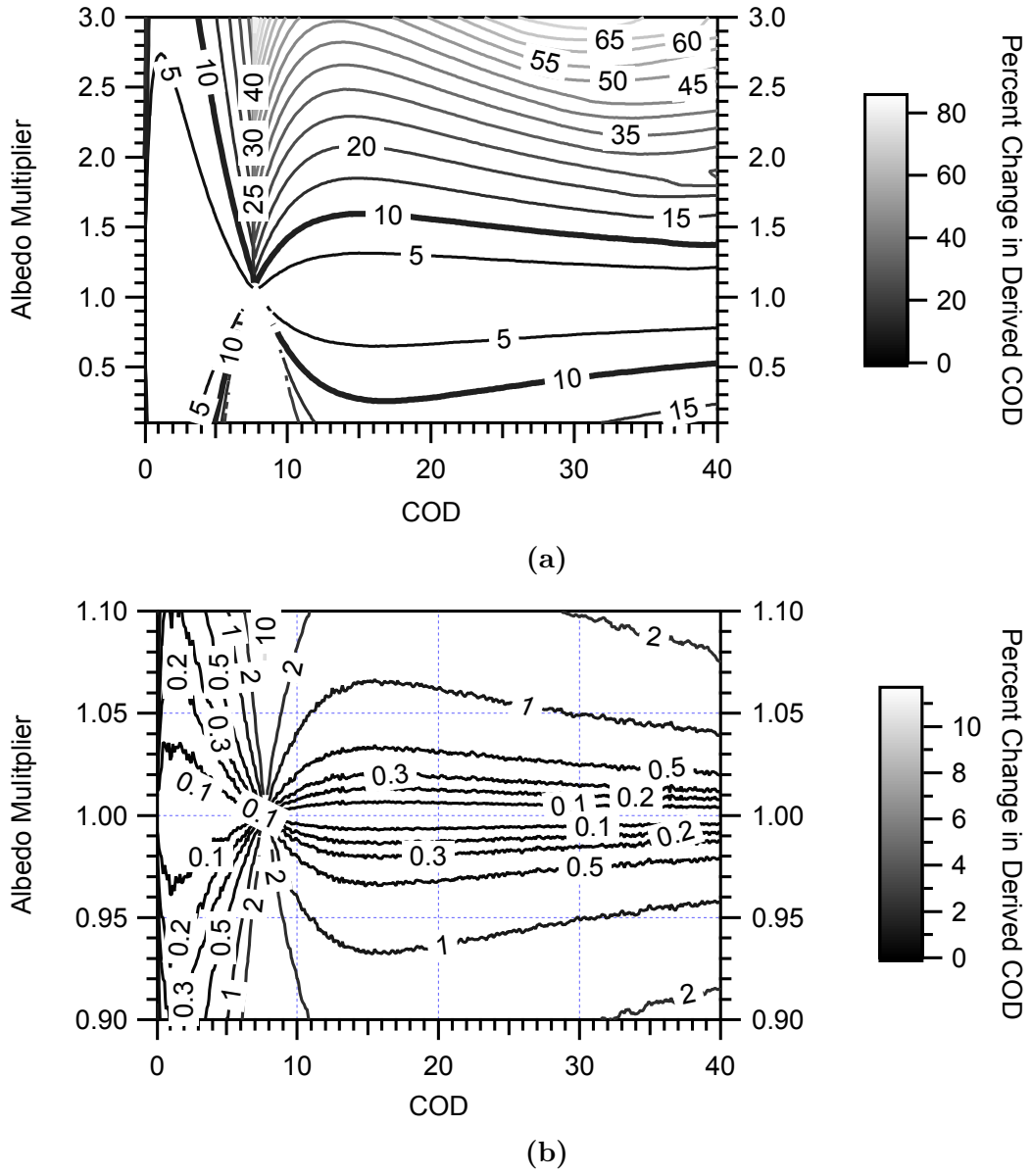

Figure 6.4: Contour map of percent change in derived COD as function of albedo and COD. (a) Albedo varied by a factor of 0.1 to 3, in intervals of 0.1. The thick black line represents when the cloud optical is changed by ten percent. (b) Expanded view, when albedo multiplier varies from 0.9-1.1 in intervals of 0.01, there is less dependence on albedo for COD less than 7 and consequently less error is attributed to COD. For COD larger than 10, an albedo error larger than 60% will result in a COD error larger than 10%.

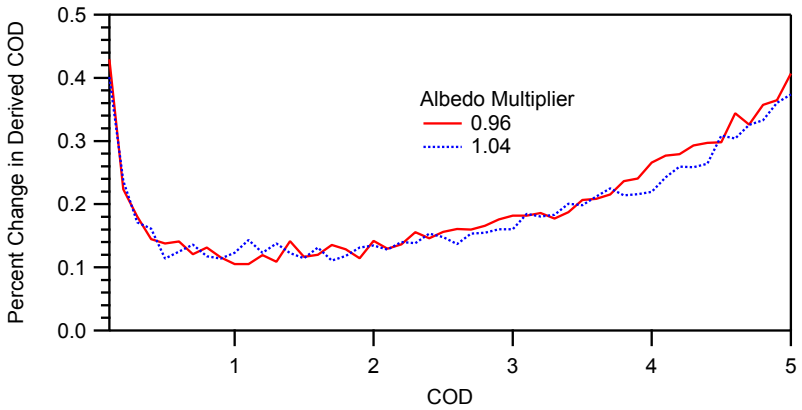

Figure 6.5: Percent change in COD from changing albedo ±4% as a function of COD. The uncertainty of our albedo measurement causes a COD error between 0.1 to 0.4%.

the albedo measurements. In order to keep the percent error in the derived COD under 10%, the surface albedo measurement must have a maximum of 60% error for COD larger than 10. From COD = 5 to 10, which is around the maximum radiance, the COD is highly sensitive to albedo, requiring less than 5% error in albedo to have a 10% error in derived COD. Given that the spectrometer used for the albedo measurements has an error of 4% and with Fig. 6.5, the COD error is between 0.1% ($COD = 1.2$) to 0.4% ($COD = 0.1$).

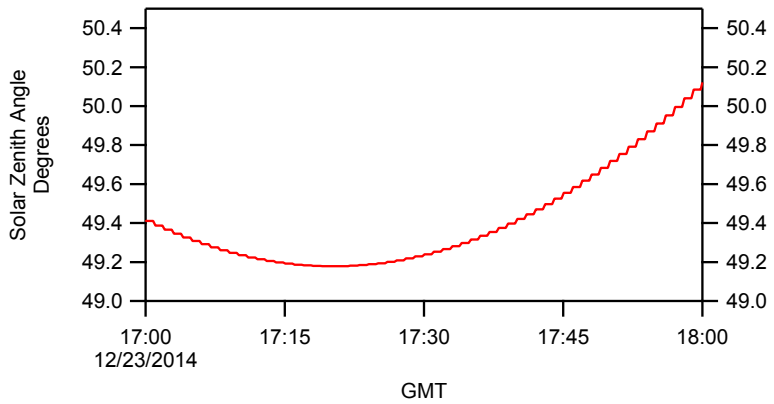

Figure 6.6: Solar zenith angle time series for data considered in previous chapter varies from 49.18° to 50.13°.

6.3 Solar Zenith Angle

This section seeks to set requirements on the applicable range of solar zenith angles per lookup table. We have the capability of creating lookup tables for any desired solar zenith angle below 80°. However, having pre-calculated tables for many solar zenith angles becomes problematic with respect to memory storage. With this in mind, we would like to minimize the number of solar zenith angle tables/files we need to at any given time.

For example, Marshak et al. [1] utilizes a lookup table for $\theta = 62 \pm 3°$. Similarly, we followed Marshak et al.'s [1] example and applied a table for $\theta = 50 \pm 2.5°$. However, by varying solar zenith angle around 50°, we find that a smaller angular restriction is required to reduce error to less than 10% in derived COD. In the data example from the previous chapter, the solar zenith angle varied from 49.18° to 50.13° (Fig. 6.6). For the error analysis, we varied the solar zenith angle from 40 to 60° (Fig. 6.7). We find that for COD from 0 to 5 and a solar zenith angle $\pm 2°$ from the original has a percent change in COD is equal to 20 to 40%.

Figure 6.8 shows contour maps of percent change in COD as a function of solar zenith angle and COD. We find that for COD greater than 20 that a $\pm 2°$ change

in solar zenith angle can cause COD error of 10%. For optically thin clouds, COD less than 5, the solar zenith angle should be less than $\pm 1^\circ$ from the lookup table's solar zenith angle to have an error less than 10%. In the time series from Fig. 6.6, the solar zenith angle varies from 49.18° to 50.13°. This causes a percent change in the derived COD from 2 to 11% (Fig. 6.9). Consequently, we can expect an error in our derived COD measurements to be between $2 - 11\%$.

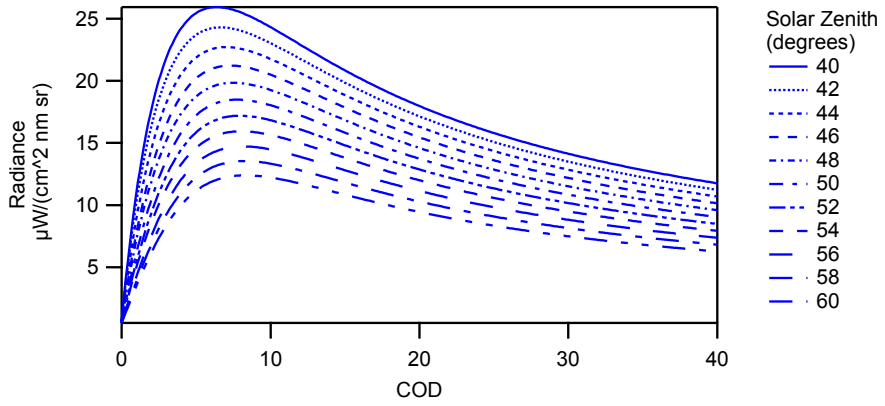

(a)

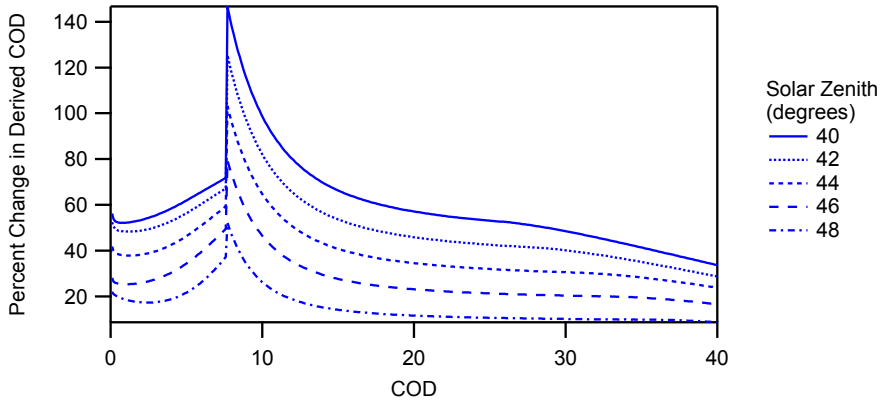

(b)

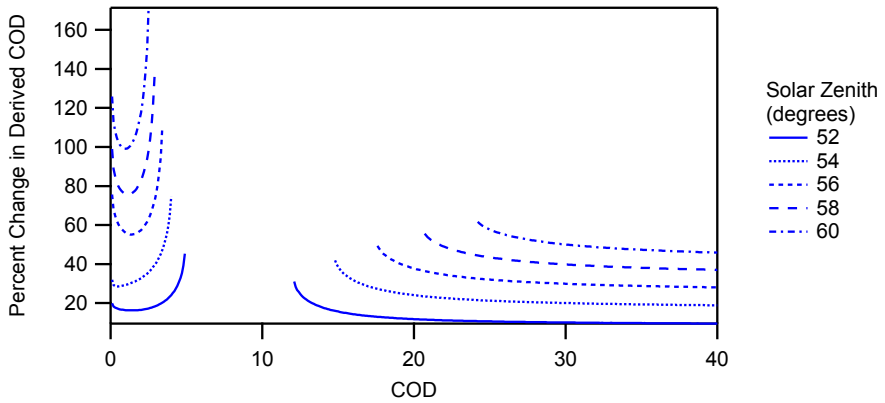

(c)

Figure 6.7: Solar zenith angle's effect on cloud models: (a) Zenith radiance for solar zenith angles from 40 to 60°. (b) Percent change in the derived COD as a result of solar zenith angles varying from 40 to 48° with respect to the 50° cloud model. (c) Percent change in the derived COD as a result of variations in solar zenith angles from 52 to 60° with respect to the 50° cloud model.

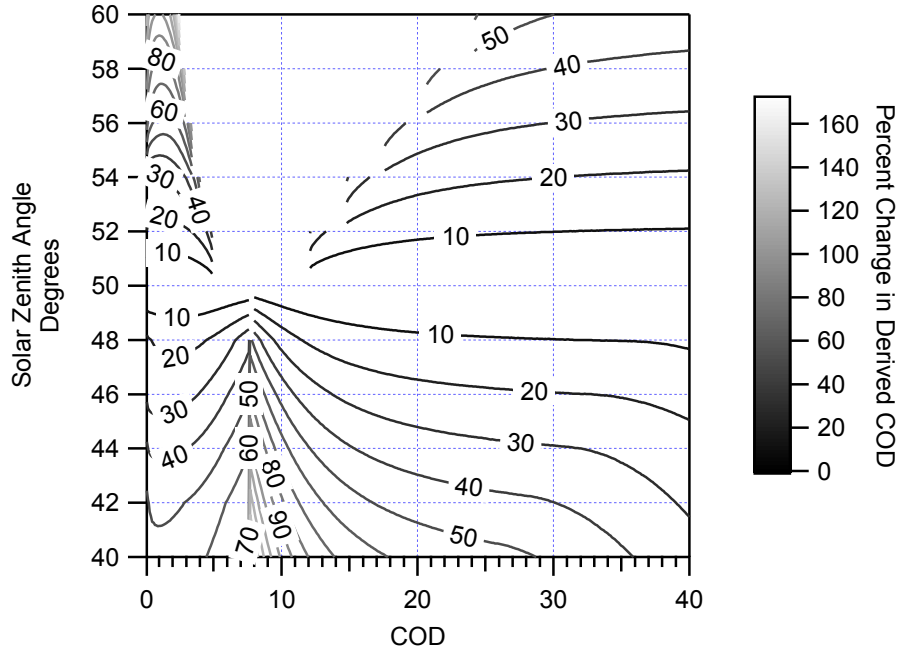

(a)

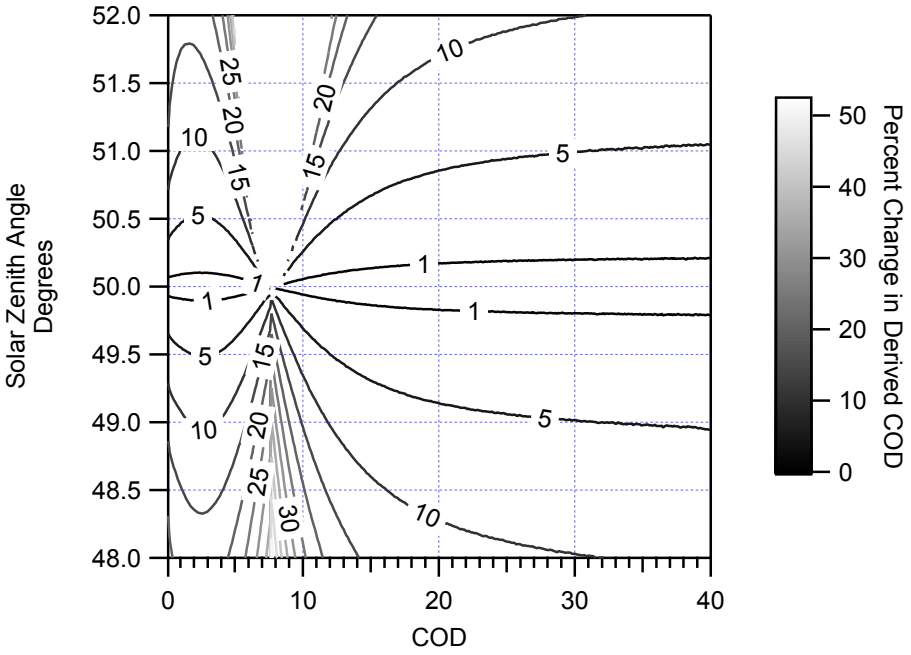

(b)

Figure 6.8: Contour maps of percent change in derived COD as a function of solar zenith angle and COD. (a) Solar zenith angles from 40 to 60°. (b) Expanded view: Solar zenith angles from 48 to 52°. For OD < 5, the lookup table must be less than $\pm 1°$ from the data to have a derived COD error less than 10%.

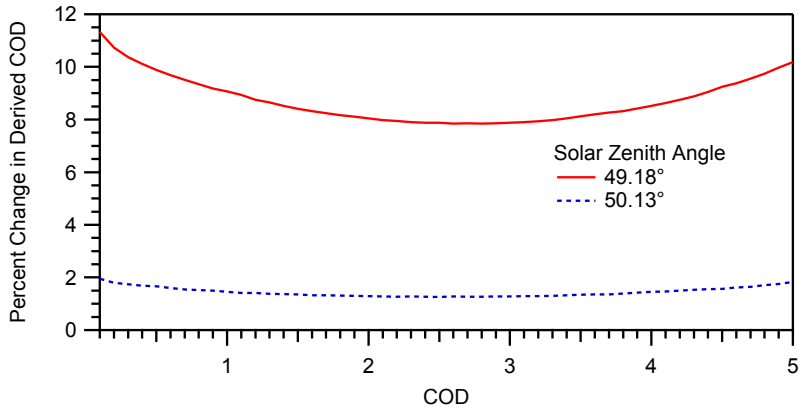

Figure 6.9: Percent error in derived COD due to using $\theta = 50°$ for data in previous chapter is from 2% ($\theta = 50.13°$) to 11% ($\theta = 49.18°$).

Chapter 7

Conclusion

Our goal was to compare inversions of cloud optical depth (COD) for optically thin clouds between two independent instruments, a micro pulse lidar (MPL) and zenith aligned radiometer. For the MPL data, we applied the Fernald inversion using a calibrated lidar coefficient C to find COD, which as discussed in Ch. 3 is calibrated using Aeronet Cimel AOD. For the Radiometer data, we used a 1D zenith radiance cloud model assuming homogeneous clouds for varying COD to generate a lookup table of COD vs zenith radiance. By interpolating this table, we can find the COD that corresponds to the measured zenith radiance. When comparing COD derived with the MPL to that derived with the radiometer, we found strong agreement. For instance, in Fig. 7.1, we find correlation coefficient of 0.94, which indicates a strong correlation. When COD is greater than 1, we find no correlation between the MPL and radiometer, which is caused by the optical power limitations of the MPL.

We studied the sensitivity of derived COD to surface albedo, particle size, and solar zenith angle. Given the measured albedo has an estimated error of 4%, we expect a maximum derived COD error equal to 0.4%. For optically thin clouds, we find that particle size contributes a maximum derived COD error equal to 2% for the range of particle sizes from 5 to 20 μm. Solar zenith angle has the biggest effect on the derived COD error: 2 to 11%. However, this is also the easiest to reduce, which can be achieved by using lookup tables with solar zenith angles closer to the data. We applied a solar zenith angle of 50° to data ranging from

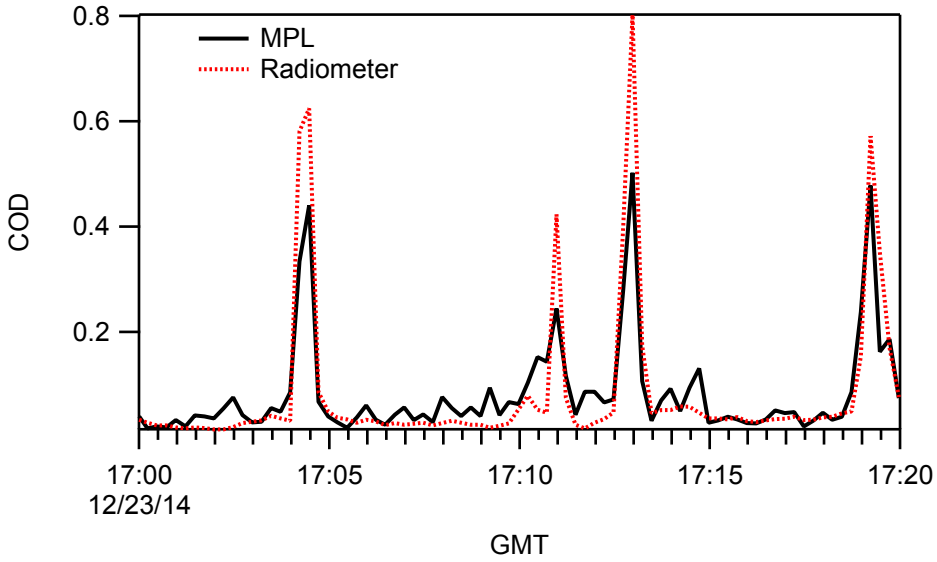

(a)

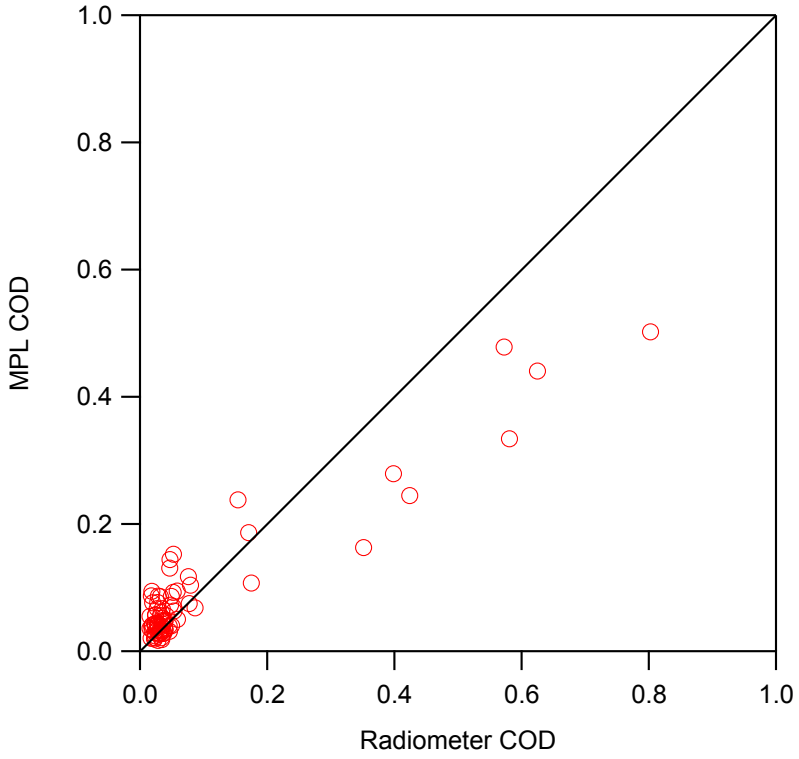

(b)

Figure 7.1: Correlation between derived COD from MPL and Radiometer. (a) COD time series comparison. (b) MPL COD vs Radiometer COD. Calculated correlation coefficient for this time period is 0.94.

49.18° to 50.13°. I have recently created new lookup tables for zenith radiance as a function of both COD and solar zenith angle (from 49.1° to 50.3° in increments of 0.1°), and have found equivalent correlation coefficients between the MPL and radiometer as discussed earlier. Consequently, when applying these new tables, the largest source of error is the effective cloud particle size (2%).

We adapted Marshak et al.'s [1] two-wavelength method to our measurement site. After performing albedo measurements at different surfaces around our site, we estimated the effective albedo. Analysis of the effective albedo spectrum shows that we do not have the spectral contrast to perform the same method as Marshak et al. [1]. However, we decided to focus on 573.9 nm and 670.1 nm, which provided the best contrast. We found that detector's integration time caused saturation problems for large COD. Since the 670.1 nm channel was not saturated, we could determine COD for optically thin clouds from one wavelength. The reason why the two-wavelength method is proposed is to avoid the multivalued problems for the zenith radiance models. For optically thin clouds this is not a problem.

Future work can lead to improved results. Smaller integration times will have less saturation. This may lead to the possibility of inverting larger COD. However, the MPL data cannot be inverted for COD greater than 1, which means that we would rely solely on the zenith radiance technique. We may also be able to use a two dimensional method to accommodate non-homogeneous cloud fields.

Investigating independent measurements of surface albedo would provide comparison with our effective albedo. For example, we could measure albedo from high altitude, such as an aircraft for instance. Another idea is to take advantage of the portability of the method we developed by moving the radiance detector to different measurement sites. For instance, we could go to the Everglades, a more

vegetated site, and retrieve COD. By refining our method and considering different sites, there are many possible directions in which to build upon this work.

15% of the global cloud cover is made of small clouds [25]. In marine environments, such as our site, nearly 50% of low clouds are optically thin [27] and cannot be measured well from space [28]. The MPL and zenith radiance COD methods developed in this work measured this cloud type. Consequently, these COD methods provide more knowledge, which was historically lacking, on a cloud type that represents a large portion of the clouds seen in marine environments and globally.

References

[1] A. Marshak, Y. Knyazikhin, K. D. Evans, and W. J. Wiscombe. The RED versus NIR plane to retrieve broken-cloud optical depth from ground-based measurements. *Journal of the Atmospheric Sciences*, 61(15):1911–1925, 2004.

[2] G. Thuillier, M. Hers, D. Labs, T. Foujols, W. Peetermans, D. Gillotay, P. Simon, and H. Mandel. The solar spectral irradiance from 200 to 2400 nm as measured by the SOLSPEC spectrometer from the Atlas and Eureca missions. *Solar Physics*, 214(1):1–22, 2003.

[3] G. W. Petty. *A first course in atmospheric radiation*. Sundog Pub, second edition, 2006.

[4] A. A. Kokhanovsky. *Cloud optics*, volume 1. Springer, 2006.

[5] D. Deirmendjian. Electromagnetic scattering on spherical polydispersions. *Electromagnetic scattering on spherical polydispersions., by Deirmendjian, D.. New York, NY (USA): Elsevier Scientific Publishing, 290 p.*, 1, 1969.

[6] G. Ayvazian. Propagation of millimeter and submillimeter waves in clouds. *Leningrad: Gidometeoizdat*, 1991.

[7] J. E. Hansen and L. D. Travis. Light scattering in planetary atmospheres. *Space Science Reviews*, 16(4):527–610, 1974.

[8] G. M. Hale and M. R. Querry. Optical constants of water in the 200-nm to 200-μm wavelength region. *Applied Optics*, 12(3):555–563, 1973.

[9] S. G. Warren. Optical constants of ice from the ultraviolet to the microwave. *Applied Optics*, 23(8):1206–1225, 1984.

[10] C. Magono, W. Chung, et al. Meteorological classification of natural snow crystals. *Journal of the Faculty of Science, Hokkaido University. Series 7, Geophysics*, 2(4):321–335, 1966.

[11] K. Sassen. The polarization lidar technique for cloud research: A review and current assessment. *Bulletin of the American Meteorological Society*, 72(12):1848–1866, 1991.

[12] E. J. Welton. *Measurements of aerosol optical properties over the ocean using sunphotometry and lidar*. PhD thesis, University of Miami, 1998.

[13] F. Kasten and A. Young. Revised optical air mass tables and approximation formula. *Applied optics*, 28(22):4735, 1989.

[14] R. Schiffer and W. B. Rossow. The international satellite cloud climatology project(ISCCP)- the first project of the world climate research programme. *American Meteorological Society, Bulletin*, 64:779–784, 1983.

[15] Q. Han, W. B. Rossow, and A. A. Lacis. Near-global survey of effective droplet radii in liquid water clouds using ISCCP data. *Journal of Climate*, 7(4):465–497, 1994.

[16] Q. Han, W. B. Rossow, J. Chou, and R. M. Welch. Global survey of the relationships of cloud albedo and liquid water path with droplet size using ISCCP. *Journal of Climate*, 11(7):1516–1528, 1998.

[17] W. B. Rossow and R. A. Schiffer. ISCCP cloud data products. *Bulletin of the American Meteorological Society*, 72(1):2–20, 1991.

[18] P. Zuidema and D. L. Hartmann. Satellite determination of stratus cloud microphysical properties. *Journal of Climate*, 8(6):1638–1657, 1995.

[19] H. Barker, T. Curtis, E. Leontieva, and K. Stamnes. Optical depth of overcast cloud across Canada: Estimates based on surface pyranometer and satellite measurements. *Journal of Climate*, 11(11):2980–2994, 1998.

[20] J. C. Barnard and C. N. Long. A simple empirical equation to calculate cloud optical thickness using shortwave broadband measurements. *Journal of Applied Meteorology*, 43(7):1057–1066, 2004.

[21] X. Dong, T. P. Ackerman, E. E. Clothiaux, P. Pilewskie, and Y. Han. Microphysical and radiative properties of boundary layer stratiform clouds deduced from ground-based measurements. *Journal of Geophysical Research: Atmospheres*, 102(D20):23829–23843, 1997.

[22] E. Leontieva, K. Stamnes, and J. Olseth. Cloud optical properties at bergen (norway) based on the analysis of long-term solar irradiance records. *Theoretical and applied climatology*, 50(1-2):73–82, 1994.

[23] Q. Min and L. C. Harrison. Cloud properties derived from surface mfrsr measurements and comparison with GOES results at the ARM SGP site. *Geophysical Research Letters*, 23(13):1641–1644, 1996.

[24] E. Leontyeva and K. Stamnes. Estimations of cloud optical thickness from ground-based measurements of incoming solar radiation in the arctic. *Journal of climate*, 7(4):566–578, 1994.

[25] R. Wood and P. R. Field. The distribution of cloud horizontal sizes. *Journal of Climate*, 24(18):4800–4816, 2011.

[26] C. Justice, J. Townshend, E. Vermote, E. Masuoka, R. Wolfe, N. Saleous, D. Roy, and J. Morisette. An overview of modis land data processing and product status. *Remote sensing of Environment*, 83(1):3–15, 2002.

[27] L. Leahy, R. Wood, R. Charlson, C. Hostetler, R. Rogers, M. Vaughan, and D. Winker. On the nature and extent of optically thin marine low clouds. *Journal of Geophysical Research: Atmospheres*, 117(D22), 2012.

[28] I. Koren, L. Oreopoulos, G. Feingold, L. Remer, and O. Altaratz. How small is a small cloud? *Atmospheric Chemistry and Physics*, 8(14):3855–3864, 2008.

[29] K. D. Moore, K. J. Voss, and H. R. Gordon. Spectral reflectance of whitecaps: instrumentation, calibration, and performance in coastal waters. *Journal of Atmospheric and Oceanic Technology*, 15(2):496–509, 1998.

[30] K. D. Moore, K. J. Voss, and H. R. Gordon. Spectral reflectance of whitecaps: Their contribution to water-leaving radiance. *Journal of Geophysical Research: Oceans*, 105(C3):6493–6499, 2000.

[31] B. Holben, T. Eck, I. Slutsker, D. Tanre, J. Buis, A. Setzer, E. Vermote, J. Reagan, Y. Kaufman, T. Nakajima, et al. AERONETA federated instrument network and data archive for aerosol characterization. *Remote sensing of environment*, 66(1):1–16, 1998.

[32] A. Ångström. On the atmospheric transmission of sun radiation and on dust in the air. *Geografiska Annaler*, pages 156–166, 1929.

[33] C. J. Flynn, A. Mendoza, Y. Zheng, and S. Mathur. Novel polarization-sensitive micropulse lidar measurement technique. *Optics express*, 15(6):2785–2790, 2007.

[34] M. Bass, C. DeCusatis, J. Enoch, V. Lakshminarayanan, G. Li, C. Macdonald, V. Mahajan, and E. Van Stryland. *Handbook of optics, Volume II: Design, fabrication and testing, sources and detectors, radiometry and photometry.* McGraw-Hill, Inc., 2009.

[35] C. Y. Young, L. C. Andrews, and A. Ishimaru. Time-of-arrival fluctuations of a space–time gaussian pulse in weak optical turbulence: an analytic solution. *Applied Optics*, 37(33):7655–7660, 1998.

[36] E. J. Welton and J. R. Campbell. Micropulse lidar signals: Uncertainty analysis. *Journal of Atmospheric and Oceanic Technology*, 19(12):2089–2094, 2002.

[37] J. R. Campbell, D. L. Hlavka, E. J. Welton, C. J. Flynn, D. D. Turner, J. D. Spinhirne, V. S. Scott III, and I. Hwang. Full-time, eye-safe cloud and aerosol lidar observation at atmospheric radiation measurement program sites: Instruments and data processing. *Journal of Atmospheric and Oceanic Technology*, 19(4):431–442, 2002.

[38] U. NOAA and U. A. Force. U.S. Standard Atmosphere, 1976. Technical report, NOAA-S/T, 1976.

[39] S. A. Glantz and B. K. Slinker. *Primer of applied regression and analysis of variance*, volume 309. McGraw-Hill New York, 1990.

[40] E. J. Welton, K. J. Voss, H. R. Gordon, H. Maring, A. Smirnov, B. Holben, B. Schmid, J. M. Livingston, P. B. Russell, P. A. Durkee, et al. Ground-based lidar measurements of aerosols during ACE-2: instrument description, results, and comparisons with other ground-based and airborne measurements. *Tellus B*, 52(2):636–651, 2000.

[41] F. G. Fernald. Analysis of atmospheric lidar observations: some comments. *Applied optics*, 23(5):652–653, 1984.

[42] Google Earth. "ARM: Lamont, OK" 36.602892 N and -97.481484 E, 4/18/2013, 10/23/2014.

[43] Google Earth. "RSMAS: Key Biscayne, FL" 25.730827 N and -80.161070 E, 1/18/2014, 5/19/2014.

[44] E. G. Dutton, A. Farhadi, R. S. Stone, C. N. Long, and D. W. Nelson. Long-term variations in the occurrence and effective solar transmission of clouds as determined from surface-based total irradiance observations. *Journal of Geophysical Research: Atmospheres*, 109(D3), 2004.

[45] E. G. Moody, M. D. King, S. Platnick, C. B. Schaaf, and F. Gao. Spatially complete global spectral surface albedos: Value-added datasets derived from terra MODIS land products. *Geoscience and Remote Sensing, IEEE Transactions on*, 43(1):144–158, 2005.

[46] W. J. Wiscombe. Improved mie scattering algorithms. *Applied Optics*, 19(9):1505–1509, 1980.

[47] W. J. Wiscombe. MIEV documentation, 1996.

[48] O. Geoffroy, J.-L. Brenguier, and F. Burnet. Parametric representation of the cloud droplet spectra for LES warm bulk microphysical schemes. *Atmospheric Chemistry and Physics*, 10(10):4835–4848, 2010.

[49] K. Stamnes, S.-C. Tsay, W. Wiscombe, and I. Laszlo. DISORT, a general-purpose fortran program for discrete-ordinate-method radiative transfer in scattering and emitting layered media: documentation of methodology. *Goddard Space Flight Center, NASA*, 2000.

[50] M. Box, S. Gerstl, and C. Simmer. Application of the adjoint formulation to the calculation of atmospheric radiative effects. *Beitr. Phys. Atmos*, 61(4):303–311, 1988.

[51] J. C. Chiu, A. Marshak, Y. Knyazikhin, W. J. Wiscombe, H. W. Barker, J. C. Barnard, and Y. Luo. Remote sensing of cloud properties using ground-based measurements of zenith radiance. *Journal of Geophysical Research: Atmospheres*, 111(D16), 2006.

[52] H. R. Gordon and T. Zhang. How well can radiance reflected from the oceanatmosphere system be predicted from measurements at the sea surface? *Applied Optics*, 35(33):6527–6543, 1996.